ARPA ORDER NO.: 189-1

R-1005-ARPA
November 1972

The January Global Climate Simulated by the Two-Level Mintz-Arakawa Model: A Comparison with Observation

W. L. Gates

A Report prepared for

ADVANCED RESEARCH PROJECTS AGENCY

Rand
SANTA MONICA, CA. 90406

Bibliographies of Selected Rand Publications

Rand maintains a number of special subject bibliographies containing abstracts of Rand publications in fields of wide current interest. The following bibliographies are available upon request:

Aerodynamics • Arms Control • China • Civil Defense
Communication Satellites • Communication Systems
Computer Simulation • Computing Technology
Decisionmaking • Game Theory • Maintenance • Middle East
Policy Sciences • Probability • Program Budgeting
SIMSCRIPT and Its Applications • Southeast Asia
Space Technology and Planning • Statistics • Systems Analysis
USSR/East Europe • Weapon Systems Acquisition
Weather Forecasting and Control

To obtain copies of these bibliographies, and to receive information on how to obtain copies of individual publications, write to: Publications Department, Rand, 1700 Main Street, Santa Monica, California 90406.

Published by The Rand Corporation

ARPA ORDER NO.: 189-1

R-1005-ARPA
November 1972

The January Global Climate Simulated by the Two-Level Mintz-Arakawa Model: A Comparison with Observation

W. L. Gates

A Report prepared for

ADVANCED RESEARCH PROJECTS AGENCY

Rand
SANTA MONICA, CA. 90406

This research is supported by the Advanced Research Projects Agency under Contract No. DAHC15 67 C 0141. Views or conclusions contained in this study should not be interpreted as representing the official opinion or policy of Rand or of ARPA.

PREFACE

This report is one of a series describing the results of numerical experiments with the two-level Mintz-Arakawa model, which are being carried out as part of the Rand/ARPA Climate Dynamics Program. The present work presents a systematic comparison of the observed January climate with a reference or control integration. The identification of the errors in this simulation is a necessary preliminary to the analysis of subsequent experiments designed to explore the effect of altered boundary conditions. Other Rand publications related to the present report are R-877-ARPA, which presents a detailed documentation of the atmospheric model, and R-958-ARPA, which compares the model's simulated mean forcing fields with observation.

SUMMARY

The mean global distributions of pressure, temperature, wind, moisture, cloudiness, precipitation, evaporation, and surface heat balance simulated for January by the two-level Mintz-Arakawa model are compared with the corresponding observed fields. In general the simulated climate may be considered reasonably satisfactory, particularly in view of the relative simplicity of the model. The prominent errors are a simulated cloudiness of about half that observed (in the northern hemisphere), and a precipitation rate about twice that observed and extending over too broad a zone in the tropics. The cloudiness error is evidently due to the model's production of clouds only during precipitation, and its failure to simulate nonprecipitating cloudiness at all. The precipitation error is due to an apparent simulation of excessive convective rainfall and has noticeably affected the heat and moisture balances.

The simulated January surface air temperature is higher than the specified sea-surface temperature over the tropical oceans, and has resulted in a net downward sensible heat flux at the surface between about 20°N and 20°S in contrast with observation. The evaporation, which occurs almost exclusively over the oceans, is simulated to be about 50 percent too great in the tropics. These errors evidently compensate each other in the surface heat balance everywhere except at high southern latitudes, where the low amounts of simulated cloudiness permit excessive surface insolation.

At 800 mb the simulated relative humidity is approximately half that observed between about 30°N and 20°S, while at higher latitudes it exceeds observation by an average of about 15 percent. At 400 mb the simulated zonally averaged January temperature is approximately 5 deg C above that observed in the equatorial and tropical regions; at 800 mb the simulated temperature more closely resembles observation. The meridional gradients of geopotential height in midlatitudes at both 400 mb and 800 mb are somewhat steeper than those observed, as is the meridional gradient of the 400-mb zonal mean temperature. The

associated maximum zonal winds at 400 mb and 800 mb are about 60 percent stronger than the observed winds, at least in the northern hemisphere.

These errors may in turn be related to the model's tendency to simulate too great a strength for the quasi-stationary oceanic cyclones of middle and higher latitudes, while the intensity of the individual transient waves is underestimated. The associated midlatitude Ferrel cell in the mean meridional circulation is therefore both too weak and too narrow. The subtropical oceanic anticyclones are more realistically simulated, and at least in the northern (winter) hemisphere, the strength of the associated Hadley circulation resembles that derived from observations.

A more extended summary and a discussion of the research under way on the major sources of error in the model are given in Sec. VII.

ACKNOWLEDGMENTS

I would like to thank Professors Yale Mintz and Akio Arakawa of the Department of Meteorology, University of California at Los Angeles, for permission to use their two-level general-circulation model for the present simulation. I would also like to thank Professor Mintz for his constructive review of the present paper, and for performing the integrations with corrected albedo. Thanks are also due Robert Mobley and Al Nelson of Rand for their supervision of the computations and machine graphical output.

CONTENTS

I. INTRODUCTION

Numerical models of the atmospheric circulation have been used to study the dynamics of climate since the pioneering calculation of Phillips (1956). The groups with the most extensive experience in this work are at the Geophysical Fluid Dynamics Laboratory of NOAA, at the National Center for Atmospheric Research (NCAR), and in the Department of Meteorology at UCLA. Starting from the relatively simple hemispheric model integrations reported by Smagorinsky (1963), the Princeton group has developed a hierarchy of models of the general circulation with increasing physical and numerical resolution. In the most recent (nine-level) formulation published, Holloway and Manabe (1971) have discussed the comparison of the global simulation of selected climatic elements with observation. The results of the application of the most recent (six-level) version of the NCAR model to the simulation of the global climate have been reported by Kasahara and Washington (1971). These comparisons reveal a fair degree of correspondence between the simulated and observed climate, and are an important measure of the models' fidelity.

The two-level general-circulation model developed at UCLA by Mintz and Arakawa beginning in 1961 has also received extensive use. Although this model has fewer levels than the NOAA and NCAR models, it contains a comparable degree of physical sophistication, particularly in the treatment of radiation, cloudiness, and convection (Arakawa, Katayama, and Mintz, 1969). A preliminary view of the simulations performed with an early version of this model has been given by Mintz (1965, 1968).

It is the purpose of the present report to present a comprehensive comparison with observation of the global climatic simulations made with a recent formulation of the two-level Mintz-Arakawa model (Gates et al., 1971). The performance of this model may then be evaluated alongside those of the other models cited. Because of its economy and availability, this model has been selected for use in a program of experimental integrations whose aim is the study of the response of global

climate to selected perturbations and to changes in the model's physical boundary conditions. To evaluate the significance of such simulations of climate modification properly, the model's errors in specifying a reference or control climate must first be known.

II. SUMMARY OF THE MODEL

The Mintz-Arakawa two-level, atmospheric general-circulation model employs the primitive (hydrostatic) equations at two tropospheric levels surrounding the globe. This model was summarized in its essentials by Arakawa, Katayama, and Mintz (1969), and a comprehensive description and documentation of both the model and its numerical solution were recently prepared by Gates et al. (1971). In broad outline, it predicts the horizontal wind velocity, temperature, and pressure (or geopotential) at each of two levels, which approximate the 400-mb and 800-mb surfaces, with the water-vapor mixing ratio predicted only at the lower level. The vertical motion as given by $\dot{\sigma}$ (see next page) is determined at a central level (approximately 600 mb), and is defined to be zero at the top of the model atmosphere (200 mb) as well as at the earth's surface (where the geopotential is assumed known). Identification of the model's levels is given in Fig. 1.

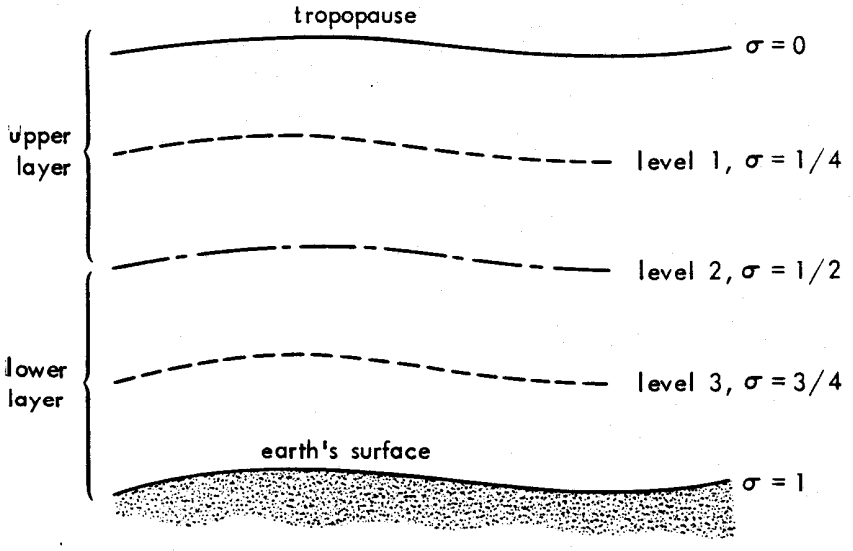

Fig. 1 -- Schematic representation of the model's vertical structure.

The diabatic heating in the model is composed of the net absorbed short- and long-wave radiation, the release of latent heat during condensation, and the sensible heating from the surface. The radiative heating is itself affected by the predicted distribution of water vapor and clouds, with the latter determined as a result of both large-scale and convective processes.

The moisture source is surface evaporation and the sink is the precipitation released in both large-scale and convective condensation. There is a momentum transfer by skin friction at the earth's surface, and an internal frictional momentum transfer between the two levels, which depends on the vertical wind shear; there is no lateral eddy viscosity or diffusion. In addition to the requirement $\dot{\sigma} = 0$ at the earth's surface, a surface thermal boundary condition of zero net heat flux is employed over land (and ice-covered) surfaces, and is used as the basis for the determination of the ground temperature itself. Over the oceans the sea-surface temperature is prescribed throughout the simulation. In the present January simulation, the topography (land elevation, ocean surface temperature, and the locations of land and sea ice) is as given by Gates et al. (1971) in the documentation of the model.

It is here sufficient to state the model's governing equations for the primary dependent variables, and to summarize the determination of those elements of the momentum, hydrologic, and heat balances whose simulated distributions are shown later. We first define the σ-coordinate system by

$$\sigma = (p - p_T)/\pi \tag{1}$$

where p is pressure, p_T an assumed tropopause pressure (200 mb), and $\pi = p_s - p_T$ is a measure of the variable surface pressure, p_s. In this system, the earth's surface ($p = p_s$) is everywhere given by $\sigma = 1$, and the top of the model atmosphere ($p = p_T$) is given by $\sigma = 0$. The model's equations of motion and thermodynamic energy may be written

$$\frac{\partial}{\partial t}(\pi\vec{V}) + \nabla(\pi\vec{V},\vec{V}) \pm \pi\dot{\sigma}_2\vec{V}_2 + \pi f\vec{k}\times\vec{V} + \pi\nabla\phi + \sigma\pi\alpha\nabla\pi = \pi\vec{F} \tag{2}$$

$$\frac{\partial}{\partial t}(\pi T) + \nabla \cdot (\pi T\vec{V}) \pm (p/p_0)^{\kappa}\pi\dot{\sigma}_2\theta_2 - (\pi\alpha\sigma/c_p)\left(\frac{\partial \pi}{\partial t} + \vec{V} \cdot \nabla\pi\right) = \pi\dot{H}/c_p \qquad (3)$$

The notation $\nabla(\pi\vec{V},\vec{V})$ is to be interpreted as $\vec{V}(\nabla\cdot\pi\vec{V}) + (\pi\vec{V}\cdot\nabla)\vec{V}$. Here $\vec{V}$ is the horizontal velocity, ϕ the geopotential, α the specific volume, f the Coriolis parameter, T the temperature, and θ the potential temperature, and $\vec{F}$ and $\dot{H}$ are the frictional force and diabatic heating rate per unit mass. When the equations are applied at the model's upper level (i.e., level 1, or $\sigma = \sigma_1 = 1/4$), the upper signs (plus) of the third terms of Eqs. (2) and (3) are used; when they are applied to the lower level (level 3, or $\sigma = \sigma_3 = 3/4$), the lower signs (minus) are used. At these levels the variables $\vec{V}$, ϕ, α, $\vec{F}$, T, p, and $\dot{H}$ assume the subscripts 1 and 3, respectively. In (2) and (3) the velocity $\vec{V}_2$ and the potential temperature θ_2 at the midlevel (i.e., level 2, or $\sigma = \sigma_2 = 1/2$) are taken to be the average of the values at levels 1 and 3. The geopotential, ϕ, is found by integration of the hydrostatic equation, $\partial\phi/\partial\sigma = -\pi\alpha$, with the assumption that the potential temperature, $\theta = T(p_0/p)^{\kappa}$, is linear in p^{κ}-space, where $\kappa = 0.286$ and $p_0 = 1000$ mb.

At the lower level, the water-vapor continuity equation is applied in the form

$$\frac{\partial}{\partial t}(\pi q_3) + \nabla \cdot \pi q_3\vec{V}_{3.5} = 2g(E - C) \qquad (4)$$

where q_3 is the mixing ratio at level 3, $\vec{V}_{3.5}$ is the wind velocity extrapolated to the (fictitious) surface $\dot{\sigma} = 7/8$ (level 3.5), and E - C is the difference between the surface evaporation rate, E, and the condensation rate, C. The precipitation rate is assumed to be equal to C, with no allowance made for either the liquid water content of clouds or for evaporation from falling rain or snow.

At the earth's surface the rate of change of the surface pressure as obtained from the continuity equation may be written in the form

$$\frac{\partial \pi}{\partial t} = -\nabla \cdot \pi\vec{V}_2 \qquad (5)$$

while at level 2 the pressure tendency may be written in terms of $\dot{\sigma}$ in the form

$$\dot{\sigma}_2 = -(4\pi)^{-1} \nabla \cdot \pi(\vec{V}_1 - \vec{V}_3) \tag{6}$$

The finite-difference approximations used to solve the system (2) to (6) are due to Arakawa, and are described in detail elsewhere (Gates et al., 1971; see also Arakawa, 1972). After the introduction of appropriate scale factors for mapping the sphere, the general computational philosophy is to write the difference equations in such a way that the model's total mass and vorticity are exactly conserved, the total energy and momentum are conserved in the absence of sources and sinks, and the mean potential temperature (and its square) are very nearly conserved. The computational grids consist of two interlocking sets of points with a resolution of 4 deg latitude and 5 deg longitude. One grid, on which π, T, and q are carried, includes the points at ±2, ±6, ±10, ... deg latitude and 0, ±5, ±10, ... deg longitude; the other grid, on which the wind velocity components, u and v, are carried, includes the points at 0, ±4, ±8, ... deg latitude and ±2.5, ±7.5, ±12.5, ... deg longitude. The finite-difference analogs are formed by appropriate averages and interpolations in the various centered and uncentered space-difference schemes. The time integration proceeds in steps of 6 minutes by means of a version of the backward differencing scheme due to Matsuno, which introduces a damping of the solutions of high frequency in time.

The source terms, $\vec{F}$, $\dot{H}$, and (E - C) in (2) to (4) are calculated every fifth time step, at which time an areal smoothing of the local lapse rate is performed. The frictional force, $\vec{F}$, consists of an internal stress at levels 1 and 3 (proportional to the vertical wind shear), and a surface stress or drag (dependent upon the surface wind, taken as 0.7 of the wind extrapolated to level 4). The surface drag acts on the wind at level 3. The heating rate, $\dot{H}$, at level 1 contains the absorption of solar radiation in the upper layer (dependent upon humidity and clouds), the net long-wave radiation lost from the layer (dependent upon temperature, humidity, and clouds), and the warming of

the layer by the latent heat released in the parameterized midlevel and penetrating convection. The heating rate at level 3 contains the corresponding quantities for the lower layer, and in addition includes both the surface sensible-heat flux (dependent upon the ground-to-air temperature difference and the surface wind) and the heating due to the latent heat released in large-scale condensation.

In the model the convective precipitation depends upon a parameterized convective adjustment process governed by the vertical stability, while the large-scale precipitation depends upon the apparent supersaturation (primarily a result of large-scale vertical motion). Midlevel clouds in the model always accompany large-scale precipitation, but the convective clouds are separately parameterized in terms of the relative humidity at level 3. An analysis of the mean January forcing fields given by the net surface frictional force (surface stress), net diabatic heating ($\dot{H}_1 + \dot{H}_3$), and net moisture addition rate (E - C) is given elsewhere (Gates, 1972).

III. THE CONTROL INTEGRATION

In order to provide a reference case against which to judge the significance of later integrations in which deliberate experimental changes are made in the model, in its associated boundary conditions, or in both, a 30-day period has here been adopted as a control simulation for comparison with January observations. In terms of the calendar position of the sun, this period extends from 29 December to 27 January; in model time this period is from day 370 to day 400 of a longer simulation started from an initial state of rest and isothermality by Mintz and Arakawa.

Of the many constants and parameters specified in the model, attention is here called only to the prescribed boundary conditions. As was previously noted, the top of the model atmosphere is taken as the 200-mb isobaric surface. Here $\dot{\sigma} = 0$ is required, and the incoming solar radiation corresponding to a solar constant of 2 ly min^{-1} is partitioned into 65 percent subject to atmospheric scattering and 35 percent subject to absorption. At the earth's surface the distributions of land elevation and sea-surface temperature are assumed to be given as shown in Figs. 2 and 3, which also serve to document the continental outlines resolved by the grid. The surface elevations shown in Fig. 2 are based on the data given by Berkofsky and Bertoni (1955), and the ocean surface temperatures shown in Fig. 3 were found from the average annual data given by Dietrich (1963). In these figures the grid points (of the π- or primary grid) are shown over the oceans, and the overprinted symbol I denotes those points at which either ice-covered land (Fig. 2) or sea ice (Fig. 3) was assumed to be present throughout the simulation. The albedo of the surface is prescribed as 0.14 for bare land and 0.07 for the oceans; the albedo of snow- or ice-covered surfaces is designed to vary between 0.4 and 0.9, depending upon the latitude and season.*

*An inadvertent program error (first pointed out by E. S. Batten) has caused the systematic underestimate of the albedo of snow and ice by about 0.4. This error is probably unimportant in the northern hemisphere (there being little solar radiation north of about 70°N in January), but has introduced some error over Antarctica as noted in some of the figures, starting with Fig. 6.

For further details of the model's configuration in the control integration, as well as a complete and annotated listing of the program, reference should be made to the model documentation (Gates et al., 1971).

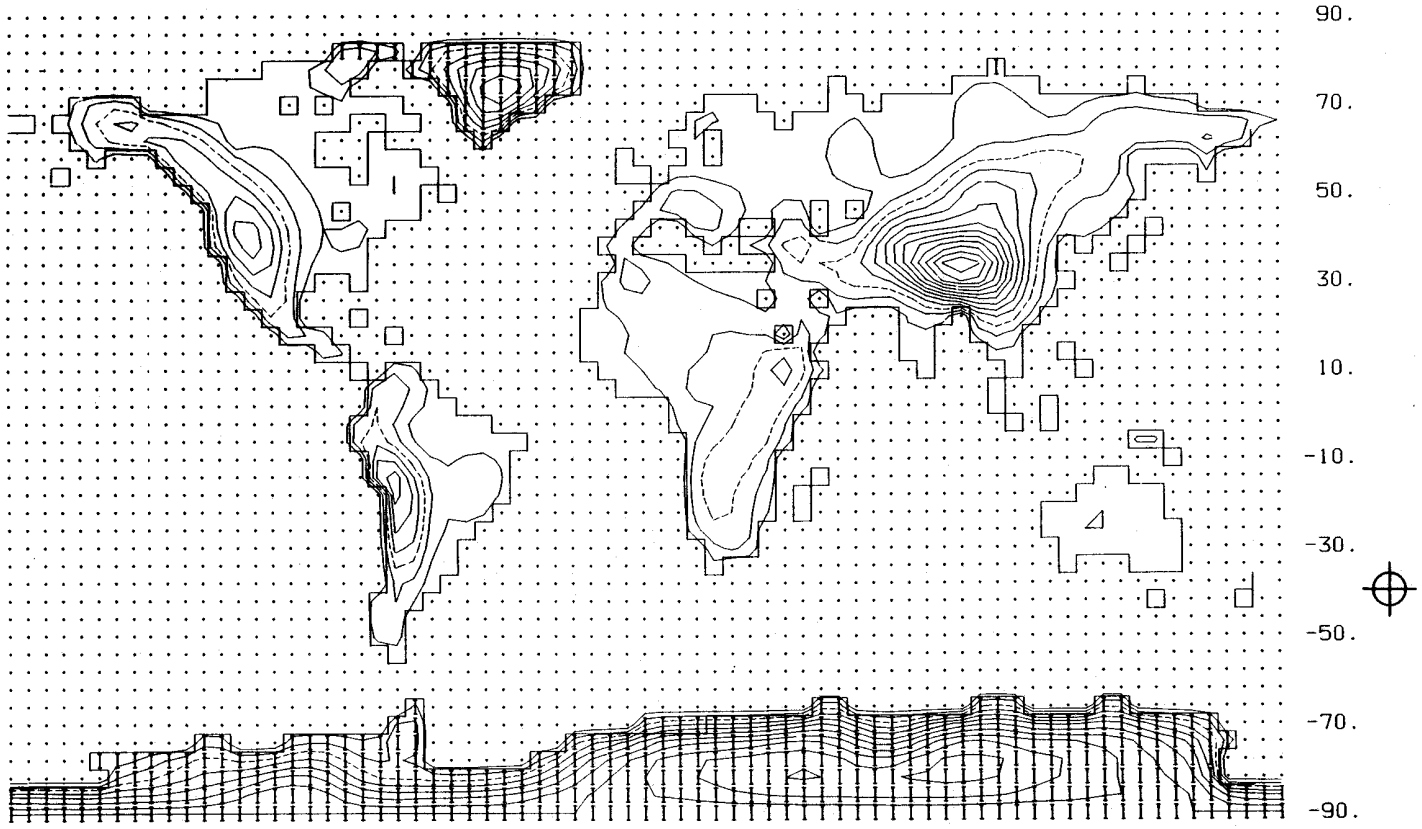

Fig. 2 -- The surface elevation used in the control experiment, with isolines every 1000 ft and the 3000-ft contour dashed. The overprinted symbol I denotes the locations of ice-covered land. The points of the basic 4-deg latitude, 5-deg longitude grid are shown over the oceans, with the latitude given on the right. From Gates et al. (1971).

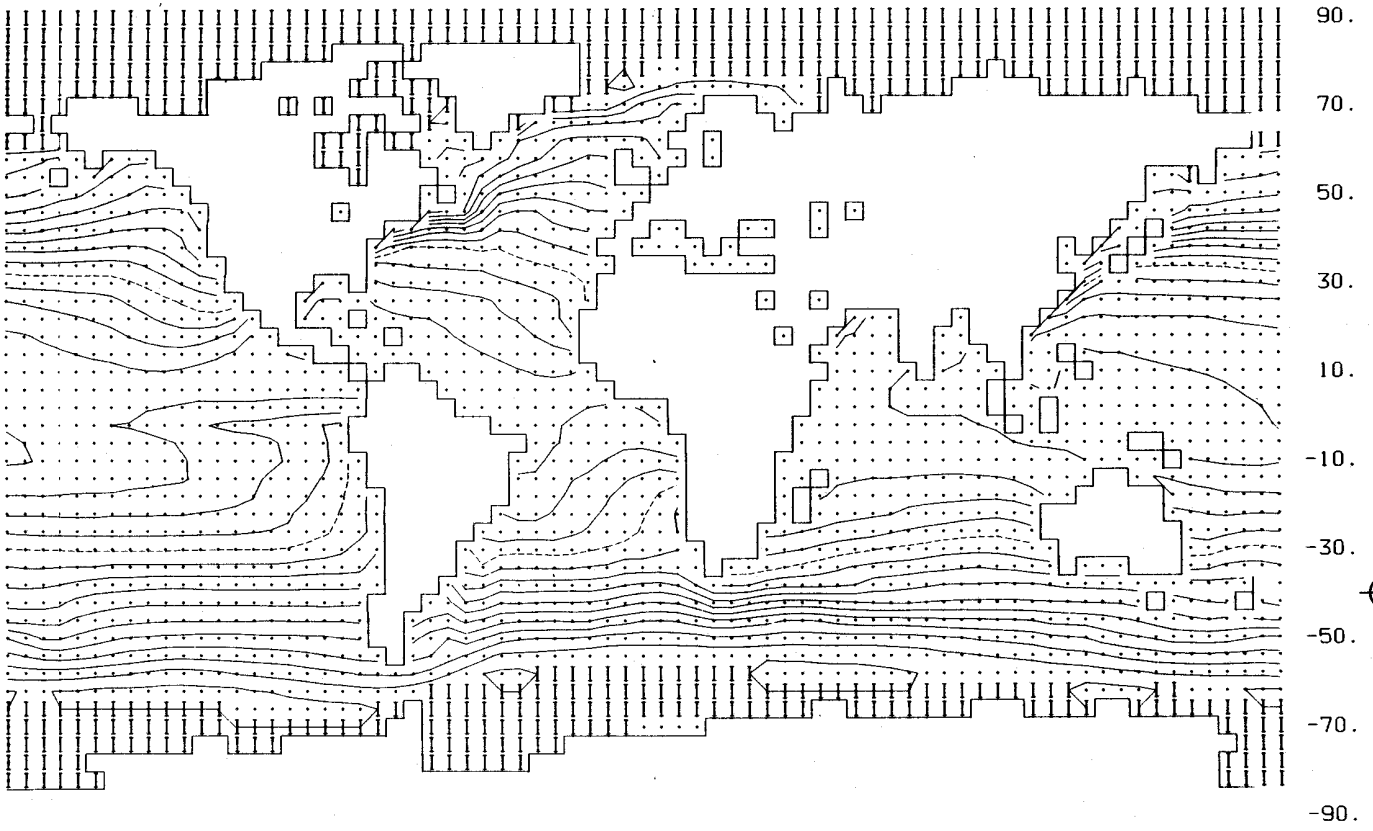

Fig. 3 -- The sea-surface temperature used in the January control experiment, with isolines every 2 deg C and the 20-deg C isotherm dashed. The overprinted symbol I denotes the locations of sea ice. From Gates et al. (1971); see also Fig. 2.

IV. THE SIMULATED AVERAGE PRESSURE, TEMPERATURE, AND WIND

Of the many quantities computed in the model, pressure, temperature, and wind exhibit behavior of particular interest; not only are these the model's primary dependent variables, but they are the meteorological variables most easily compared with observation. The distributions of humidity, cloudiness, precipitation, evaporation, and elements of the surface heat balance are considered in subsequent sections. Except as noted, all of the average distributions shown here were determined from data every 6 hours during the 30-day control simulation. The observed distributions are from various sources as compiled by Schutz and Gates (1971).

SEA-LEVEL PRESSURE

The global distribution of the average January sea-level pressure simulated in the control experiment is shown in Fig. 4, together with the observed average January pattern. In general the model has correctly depicted the principal centers of low and high pressure over the globe. The mean anticyclones in the subtropics of the southern (summer) hemisphere in particular are correctly simulated just to the west of the continents and with approximately the correct maximum pressure. The Aleutian low in the northern hemisphere is simulated about 15 mb too low, although its position is reasonably accurate. The Icelandic low, on the other hand, is simulated some 1000 km southwest of its observed average position, as well as being about 15 mb too deep.

The global distribution of the difference between the simulated and observed sea-level pressure is shown in Fig. 5. In addition to the intensity errors in the Aleutian and Icelandic lows noted above, large differences in sea-level pressure occur over the continents of the northern hemisphere, where errors of 10 to 20 mb are common. It is significant to note that these errors resemble, in general scale and magnitude, that found between successive Januaries in a three-year simulation (Mintz et al., 1972), although the simulated Januaries all show similar intensity errors in comparison with observation. This

serves to emphasize that difference maps such as Fig. 5 strongly reflect the errors of position as well as of magnitude of the quasi-stationary (monthly average) circulations.

The most serious error is a systematic overprediction of the intensity of the semi-permanent surface low-pressure systems, which steepens the pressure gradients in Fig. 4a as compared with those of Fig. 4b in the northern middle latitudes. This error is particularly noticeable in the zonally averaged sea-level pressure given in Fig. 6, where the average simulated pressure at 55°N is about 10 mb too low. The only other significant discrepancies occur south of 60°S. Here simulation exceeds observation by several millibars between about 55°S and 70°S, and the sea-level meridional pressure gradient has the wrong sign between 70°S and 86°S. This latter feature is attributed to the erroneous surface heating over the Antarctic sea ice and Antarctic continent due to an inadvertent underestimate of the albedo of snow and ice.* Over the bulk of the atmosphere, however, the simulated latitudinal pressure profile is in good agreement with the observed. Since the model is constrained to have a global average *surface* pressure equal to that observed (984 mb; see Gates et al., 1971), the difference between the simulated global average sea-level pressure (1013.3 mb) and the observed value (1011.1 mb) reflects only errors in reduction to sea level.

This comparison of predicted and observed sea-level pressure may be considered to update that given by Mintz (1965, 1968) for an earlier version of this model (which used a 7-deg latitude by 9-deg longitude grid, did not predict the water vapor or cloudiness, and had simpler treatments of convection and radiative heating, among other differences). The present model version may be considered to produce a more satisfactory overall simulation. Its use of a smaller grid size without lateral diffusion has reduced the truncation error of the middle-latitude transient cyclones in particular. Significant errors remain, however,

*This conjecture was confirmed in a subsequent January simulation in which the surface albedo for snow and ice was corrected (Mintz, personal communication); see Fig. 6.

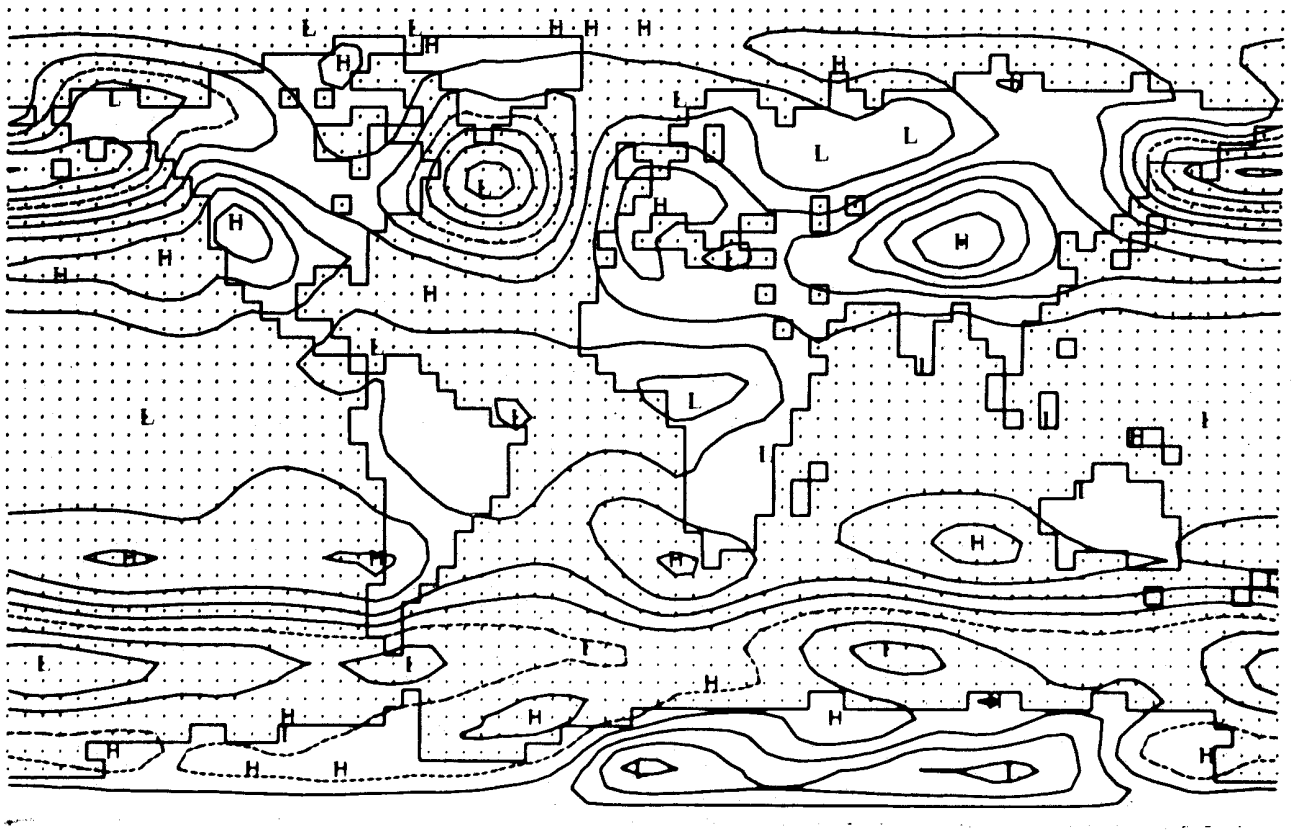

Fig. 4a -- The simulated sea-level pressure for January, with isolines every 5 mb and the 1000-mb isobar dashed. The symbols H and L denote local maxima and minima.

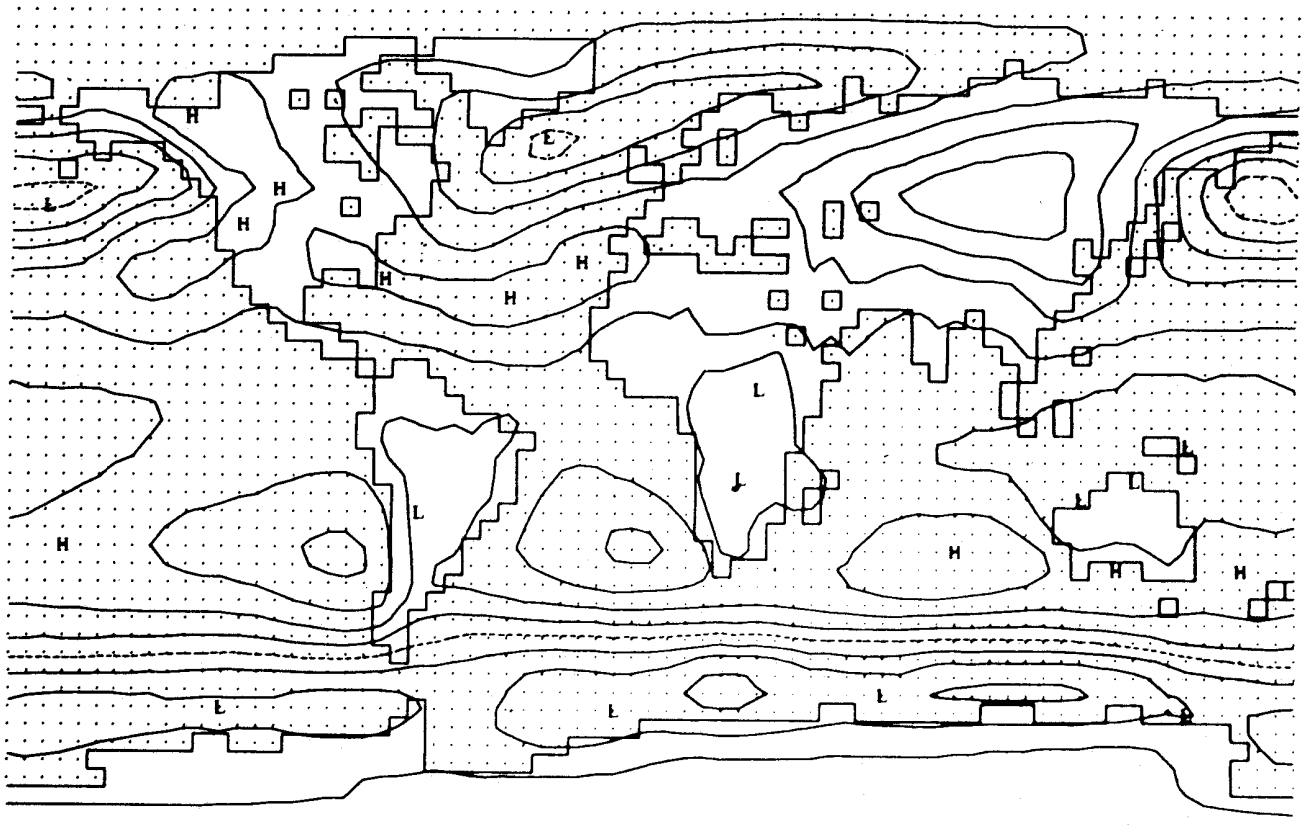

Fig. 4b -- The observed sea-level pressure with isolines every 5 mb and the 1000-mb isobar dashed. From Schutz and Gates (1971), based upon data of Crutcher and Meserve (1970) and Taljaard et al. (1969).

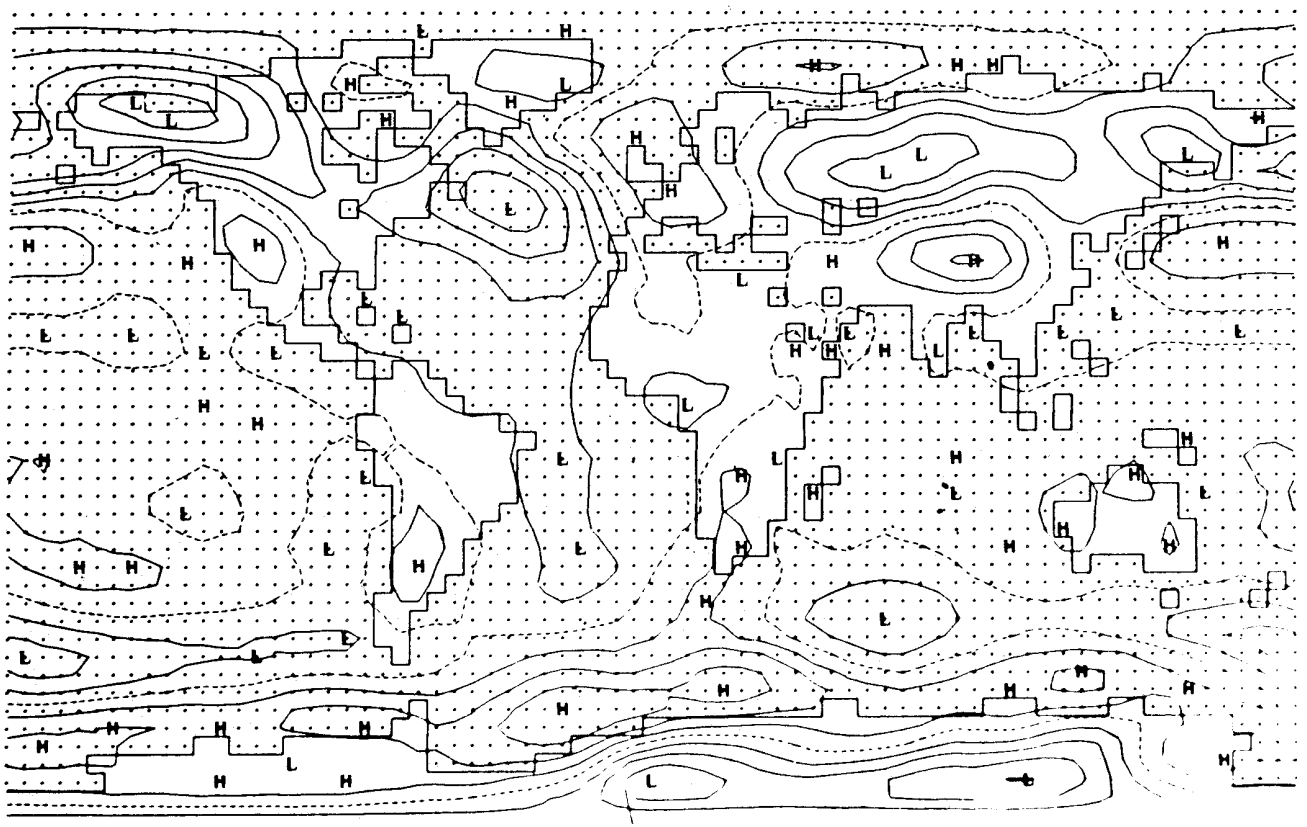

Fig. 5 -- The difference between the simulated and observed sea-level pressure (Fig. 4a minus Fig. 4b). The isobar interval is 5 mb with the zero line dashed.

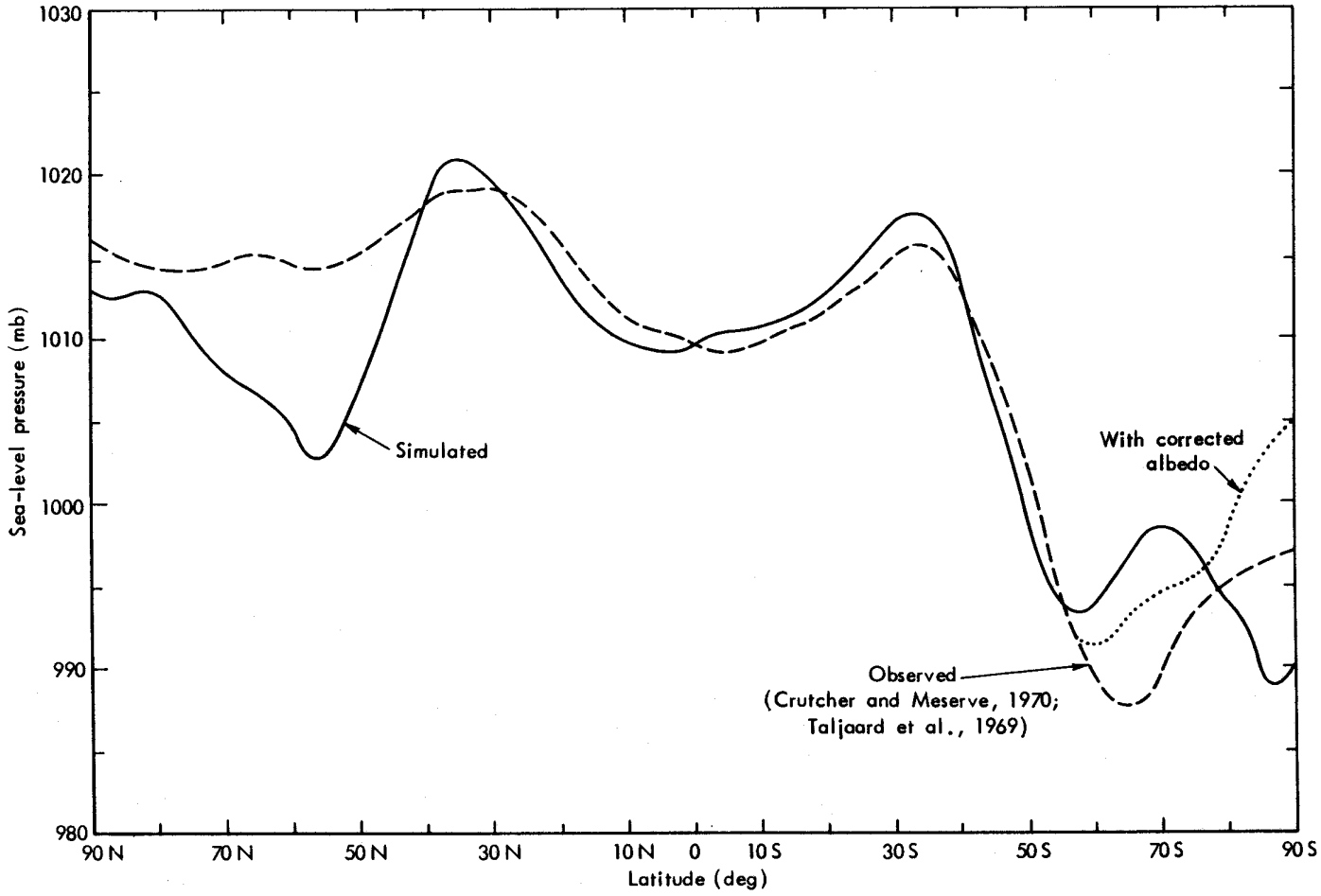

Fig. 6 -- The zonal average sea-level pressure as simulated (full line) and as observed (dashed line), based on the data of Fig. 4. The dotted curve at high southern latitudes in this and later figures is the simulation with a corrected albedo for snow and ice, as obtained from a subsequent January integration (Mintz, private communication); see footnote, p. 8.

in the amplitude (and location) of the time-averaged or quasi-stationary systems (see below, and also Gates, 1972).

GEOPOTENTIAL HEIGHTS AT 800 MB AND 400 MB

The average January geopotential height simulated at 800 mb and 400 mb are shown in Figs. 7 and 10, along with the observed global pattern.* As was the case with the sea-level pressure, the model has reproduced the general pattern of geopotential height in the troposphere with reasonable accuracy, although the simulated mean troughs and ridges are too large in amplitude. In the southern hemisphere the simulated geopotential height gradient approximately agrees with observation at both 800 mb and 400 mb, as do the pole-to-equator height differences in the northern hemisphere. The 800-mb and the 400-mb simulated height gradients in the northern middle latitudes, however, are approximately twice as great as those observed. Together with the sea-level pressure (Fig. 4), these data show the model's ability to develop the correct vertical tilt and thermal wind in the middle-latitude systems.

The error fields of the simulated geopotential heights at 800 mb and 400 mb are shown in Figs. 8 and 11. We note that the simulation errors or discrepancies are positive nearly everywhere and are several hundred meters in magnitude at both levels. This error is even more clearly shown in the latitudinal variations of the zonal averages in Figs. 9 and 12; here the simulated 800-mb and 400-mb heights are systematically higher than the observed values at all latitudes. On a global average, the mean simulated heights at 800 mb and 400 mb are 2268 m and 7600 m, which exceed the observed mean heights of these surfaces by 330 m and 322 m, respectively. The source of this discrepancy is not the interpolation errors involved in determining the simulated 800-mb and 400-mb geopotential heights, nor is it that involved in finding the observed heights (see Schutz and Gates, 1971). Rather, it lies in the determination of ϕ_1 and ϕ_3 themselves as deviations from the height of the center of mass of the model atmosphere

*Figures in some sections have been sequenced to facilitate comparison rather than in the order cited.

(see Gates et al., 1971). This height has been selected in such a way that when T_1 and T_3 are equal to the observed temperatures, the vertical integral of the model's potential and internal energy approximates the vertical integral of the potential and internal energy of the actual atmosphere. The model's center of mass thus turns out to be about 326 m higher than that of the real atmosphere, and accounts for the systematic error seen in Figs. 7 to 12.*

SURFACE AIR TEMPERATURE

The average January surface air temperature simulated in the control experiment is shown in Fig. 13, along with the observed January pattern. In broad terms the model has correctly simulated many observed features of the surface air temperature, of which the most prominent are the cold air over the interior of the continents of the northern (winter) hemisphere, the relatively warm air over the southerm hemisphere continents, and the location of the freezing isotherm (dashed line in Fig. 13). Except in the Antarctic region, where there was an underestimate of the surface albedo, the observed gradient of surface air temperature is also reasonably well portrayed in the simulation.

Over the oceans the prescription of a fixed sea-surface temperature has constrained the model's simulation of the surface air temperature to be within about 3 deg C of the prescribed water temperature, as may be seen in the global error of Fig. 14. Over most of the tropical oceans, however, the simulated surface air temperature is higher than the sea-surface temperature itself (see Fig. 3). This feature has affected the surface heating as is discussed in Sec. VI below. Over the continents, where a surface heat balance was assumed in the model, even larger errors occur. In general, the land regions of middle and high latitudes are simulated to be too warm by about 10 deg, while in the tropics the land areas are characteristically simulated to be several degrees too cold. This is probably the result of the model's inability to accurately portray either a strong surface inversion or a steep low-level lapse rate. The model's failure to develop a strong surface

*I am indebted to Yale Mintz and Akio Arakawa for pointing out this property in their model.

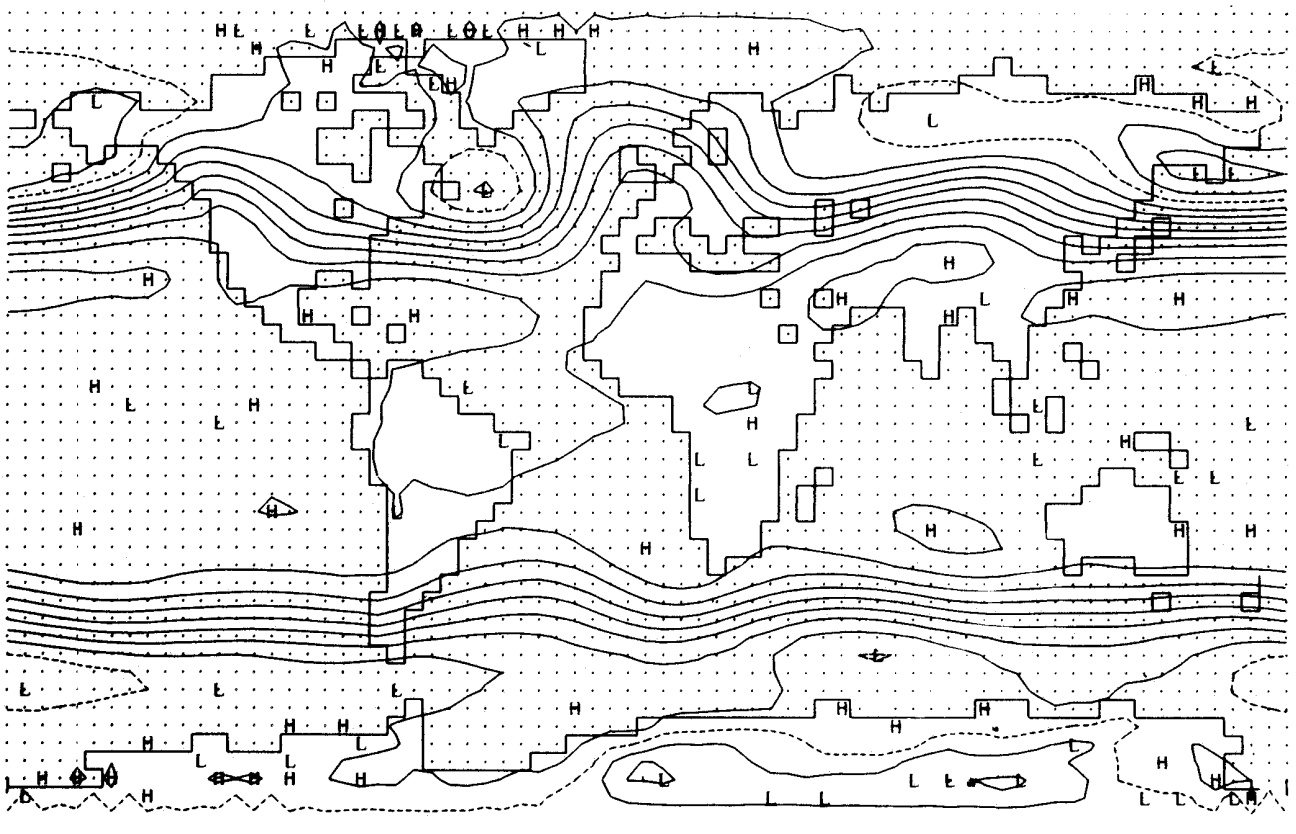

Fig. 7a -- The simulated geopotential height at 800 mb for January, with isolines every 50 m and the 2000-m contour dashed.

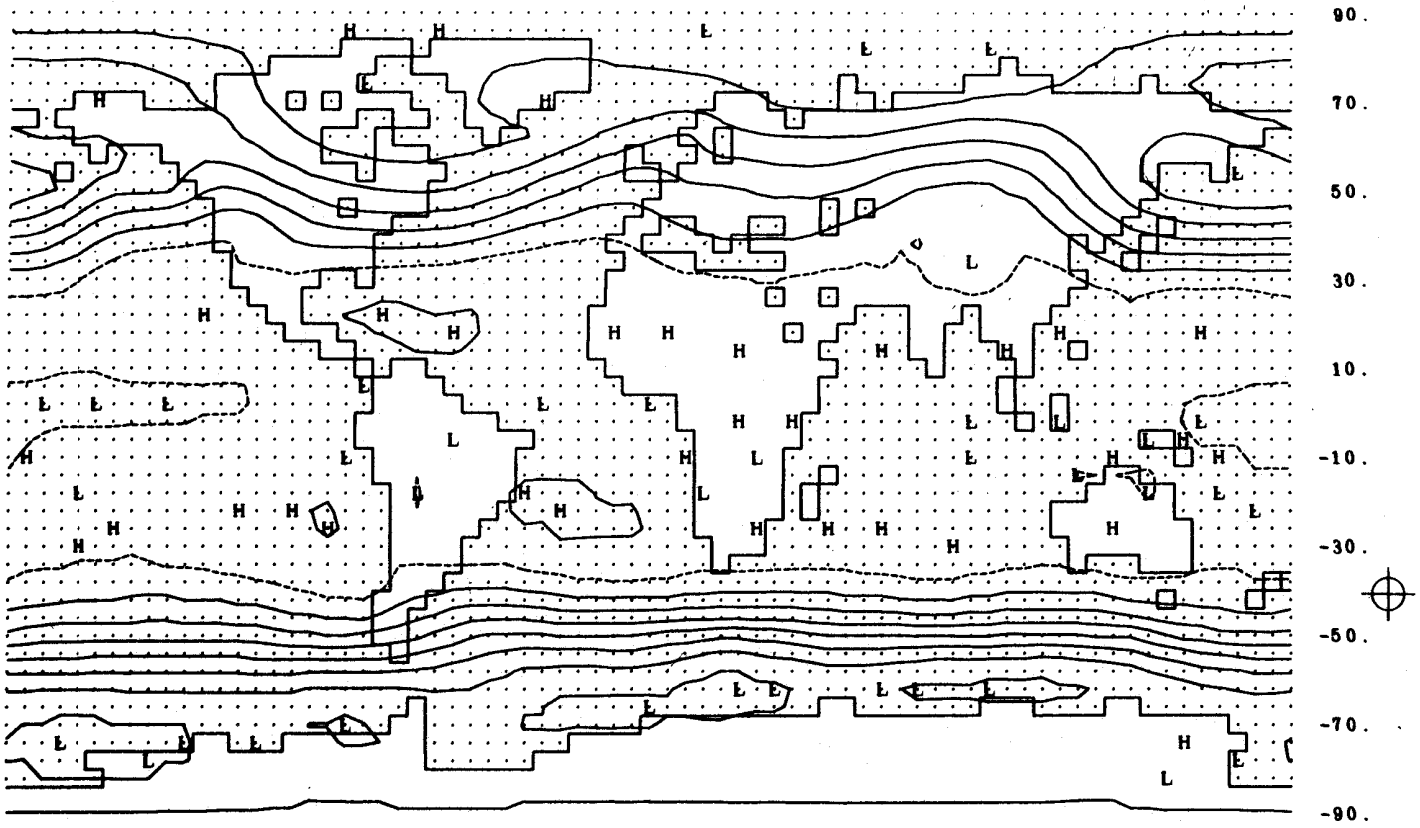

Fig. 7b -- The observed geopotential height at 800 mb for January with isolines every 50 m and the 2000-m contour dashed. From Schutz and Gates (1971), based on data of Crutcher and Meserve (1970) and Taljaard et al. (1969).

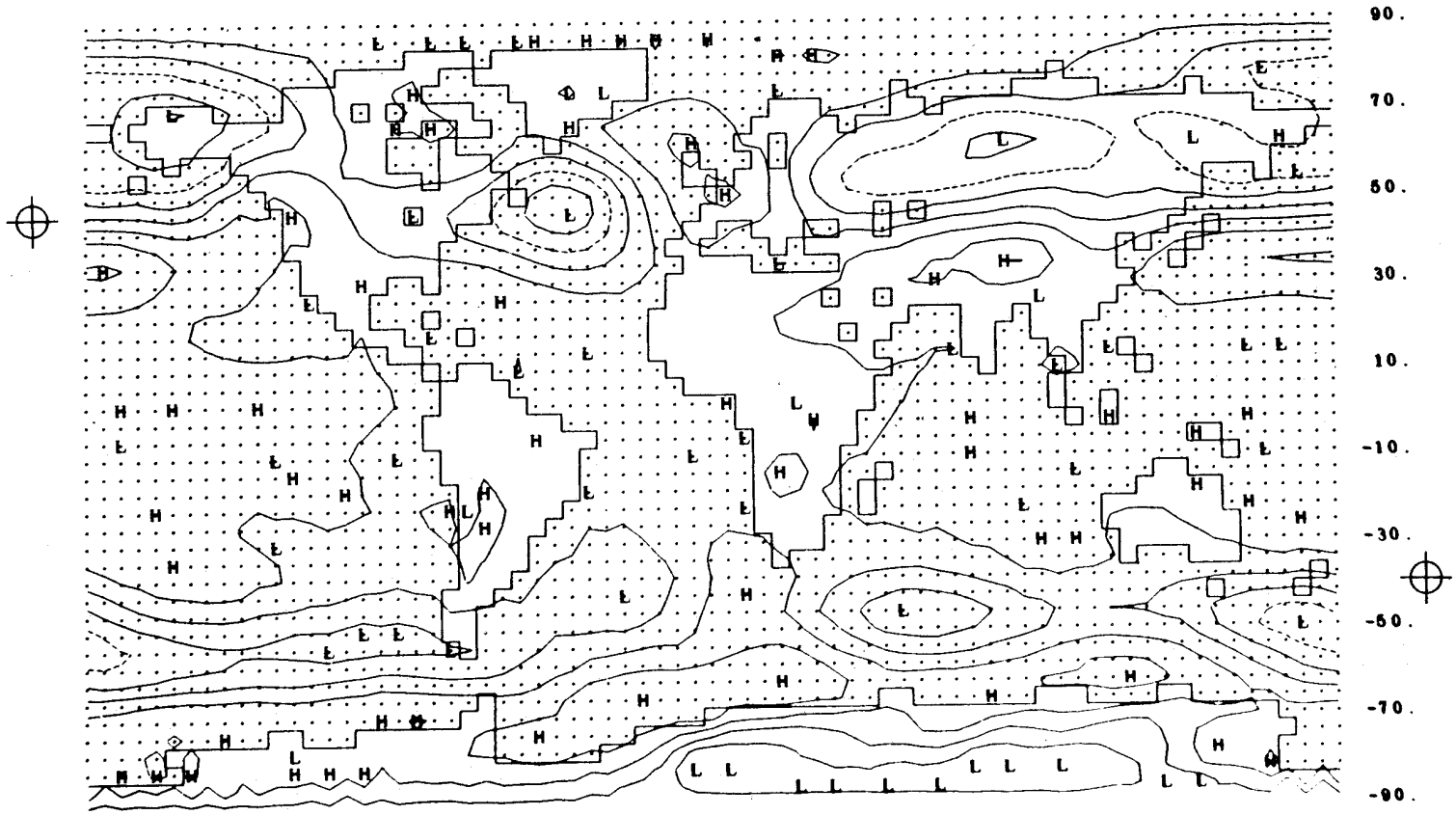

Fig. 8 -- The difference between the simulated and observed 800-mb geopotential height (Fig. 7a minus Fig. 7b). The isoline interval is 50 m with the 200-m line dashed.

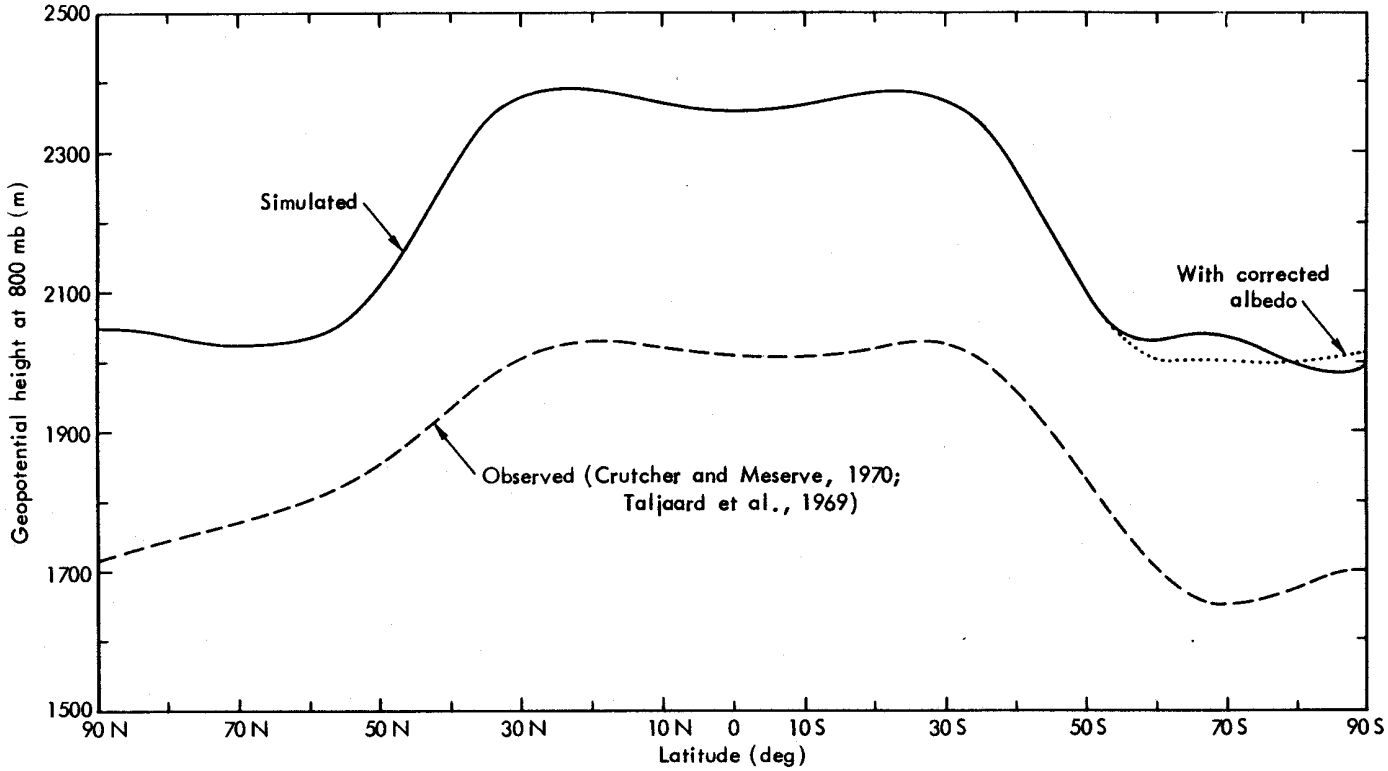

Fig. 9 -- The zonal average 800-mb geopotential height as simulated (full line) and as observed (dashed line), based on the data of Fig. 7. See Fig. 6 for dotted-line identification.

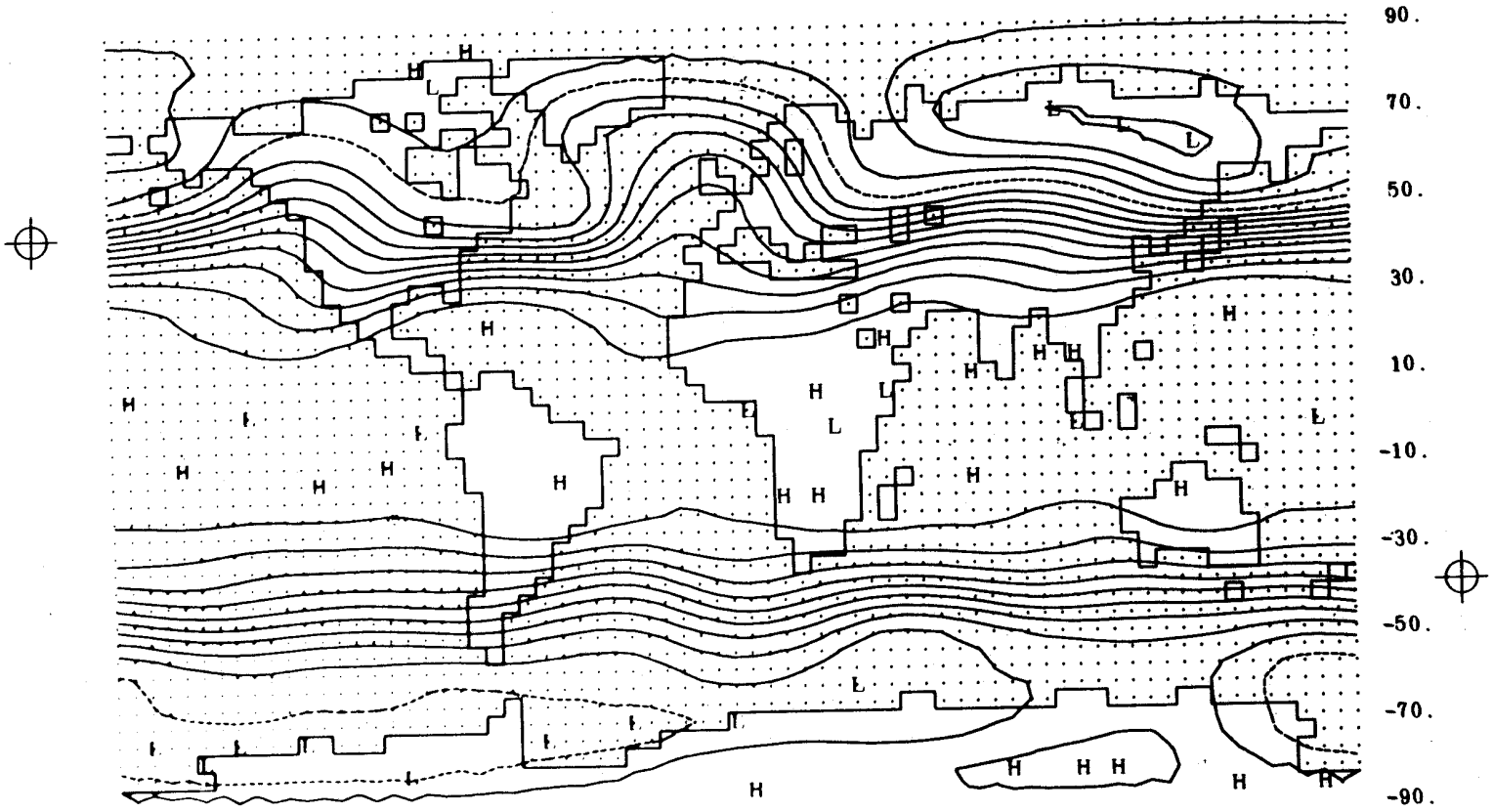

Fig. 10a -- The simulated geopotential height at 400 mb for January, with isolines every 100 m and the 7000-m contour dashed.

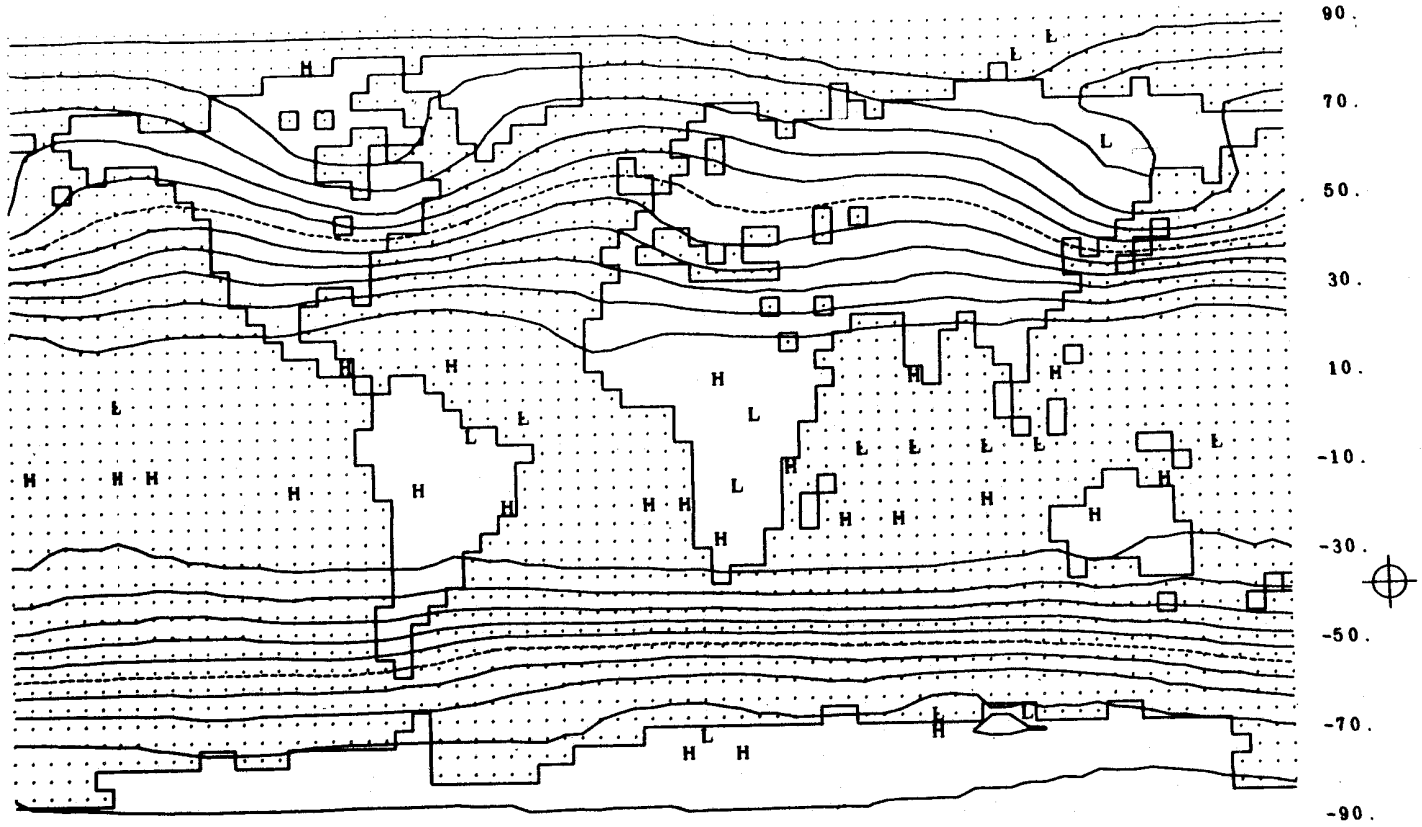

Fig. 10b -- The observed geopotential height at 400 mb for January, with isolines every 100 m and the 7000-m contour dashed. From Schutz and Gates (1971), based on data of Crutcher and Meserve (1970) and Taljaard et al. (1969).

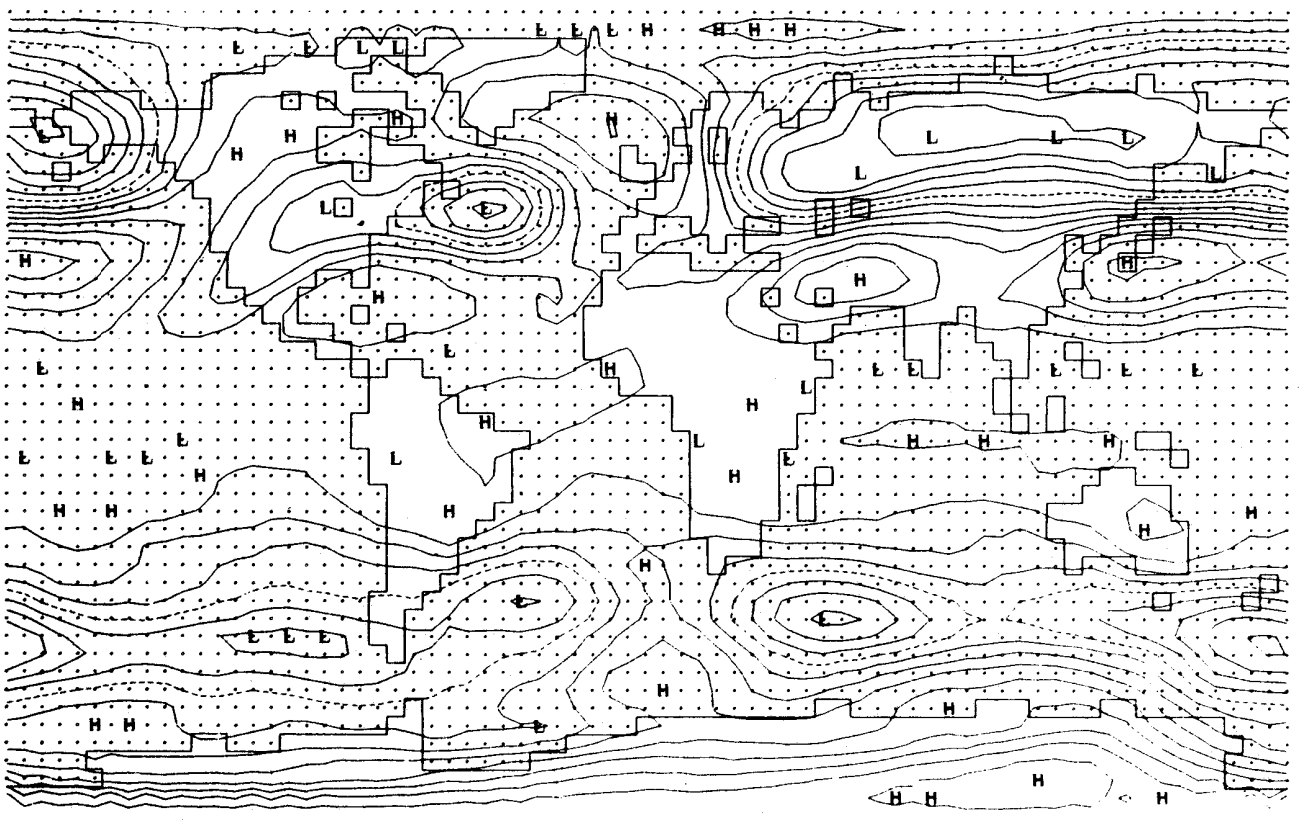

Fig. 11 -- The difference between the simulated and observed 400-mb geopotential height (Fig. 10a minus Fig. 10b). The isoline interval is 50 m with the 200-m line dashed.

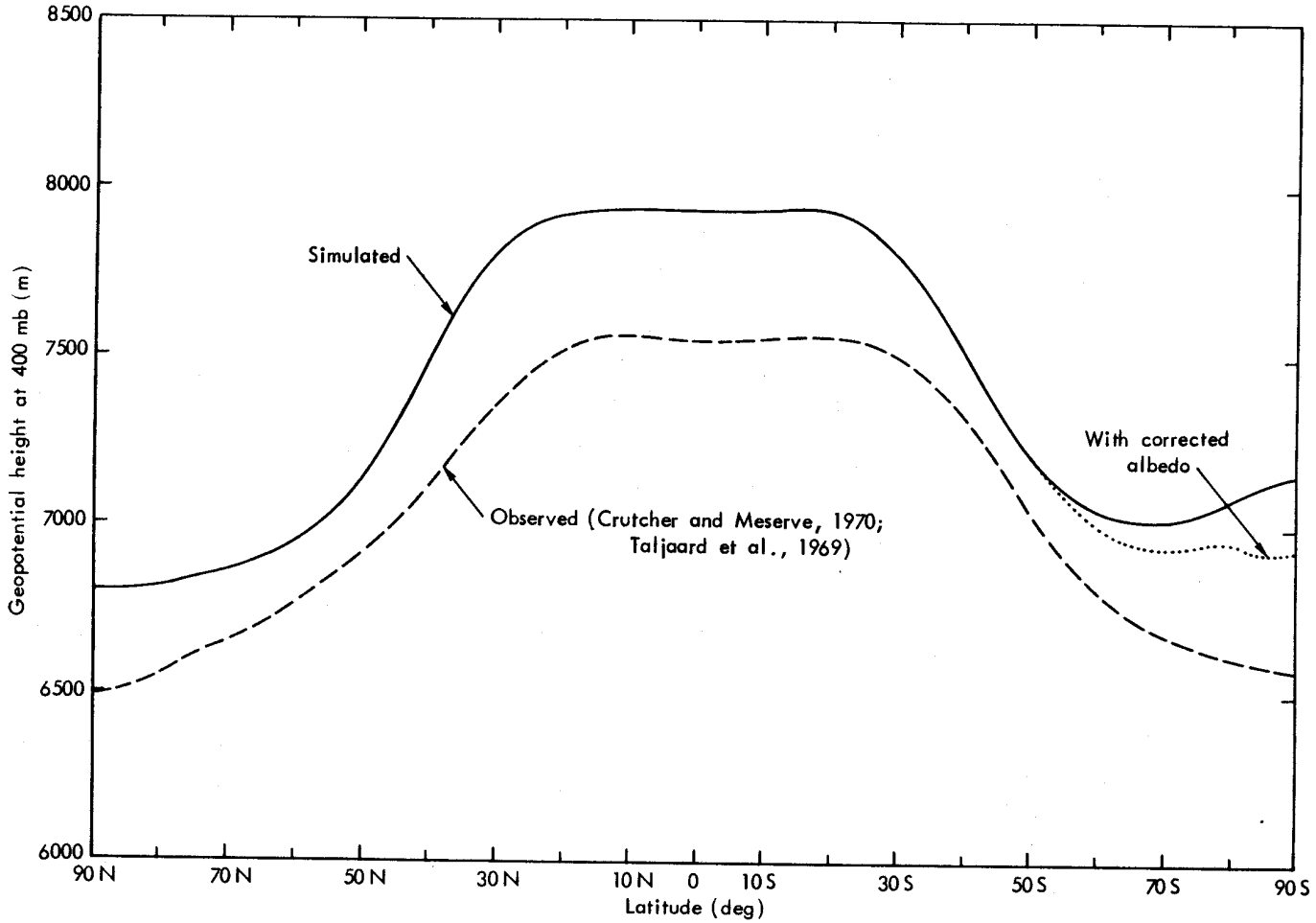

Fig. 12 -- The zonal average 400-mb geopotential height as simulated (full line) and as observed (dashed line), based on the data of Fig. 10.

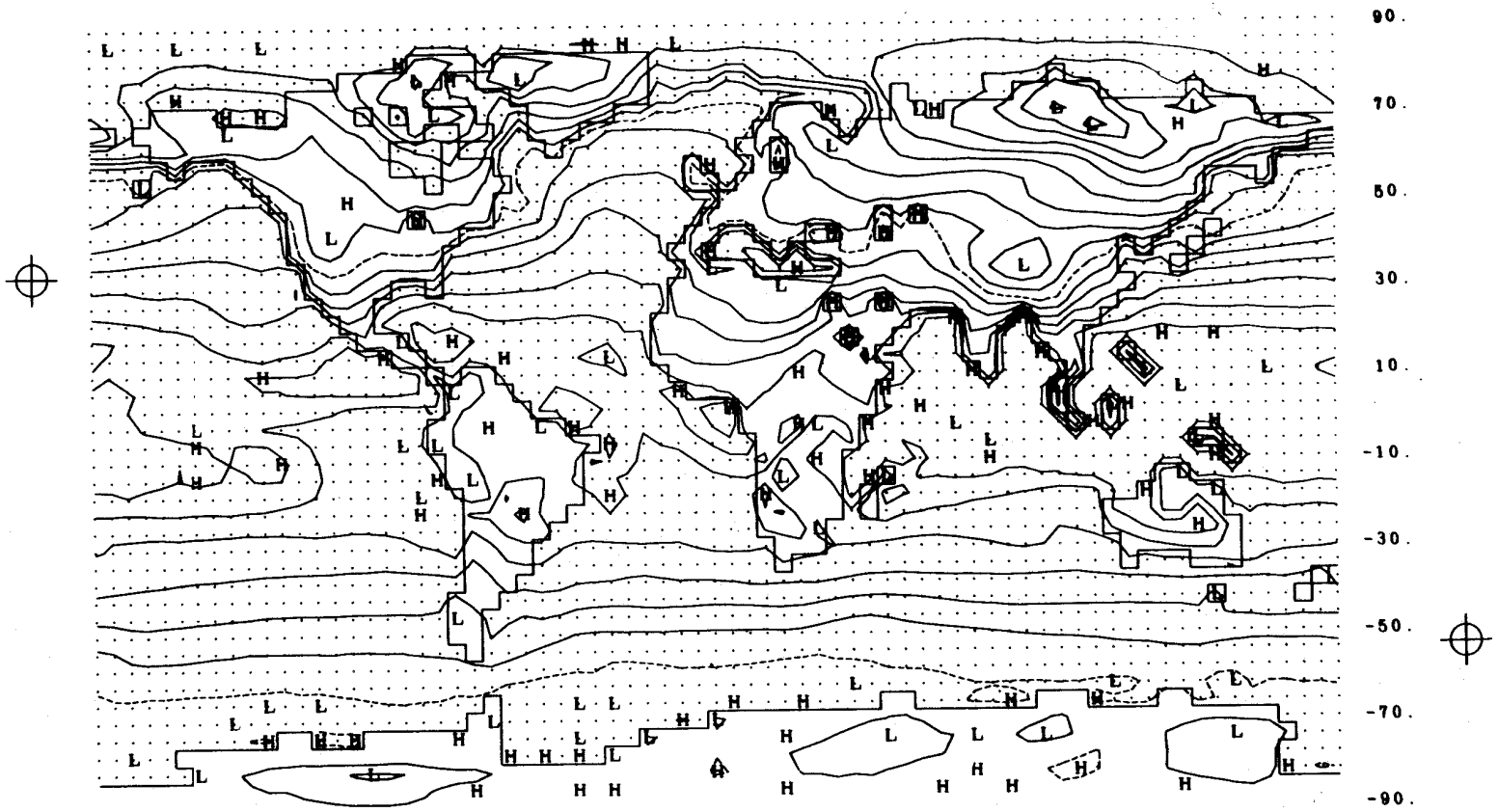

Fig. 13a -- The simulated surface air temperature for January, with isolines at 5 deg C intervals and the 0-deg C isotherm dashed

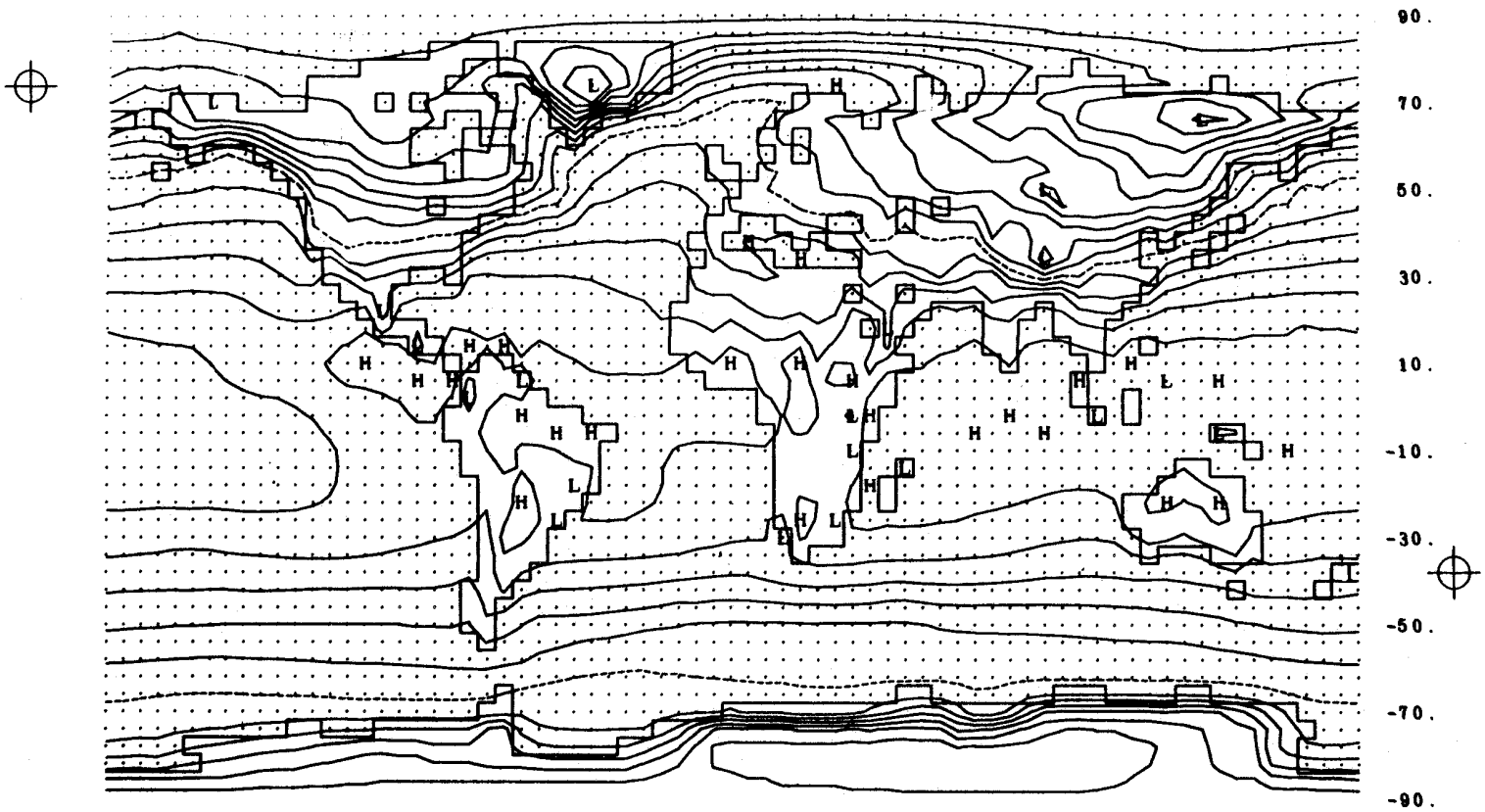

Fig. 13b -- The observed surface air temperature for January, with isolines at 5-deg C intervals and the 0 deg C isotherm dashed. From Schutz and Gates (1971), based on data of Crutcher and Meserve (1970) and Taljaard et al. (1969).

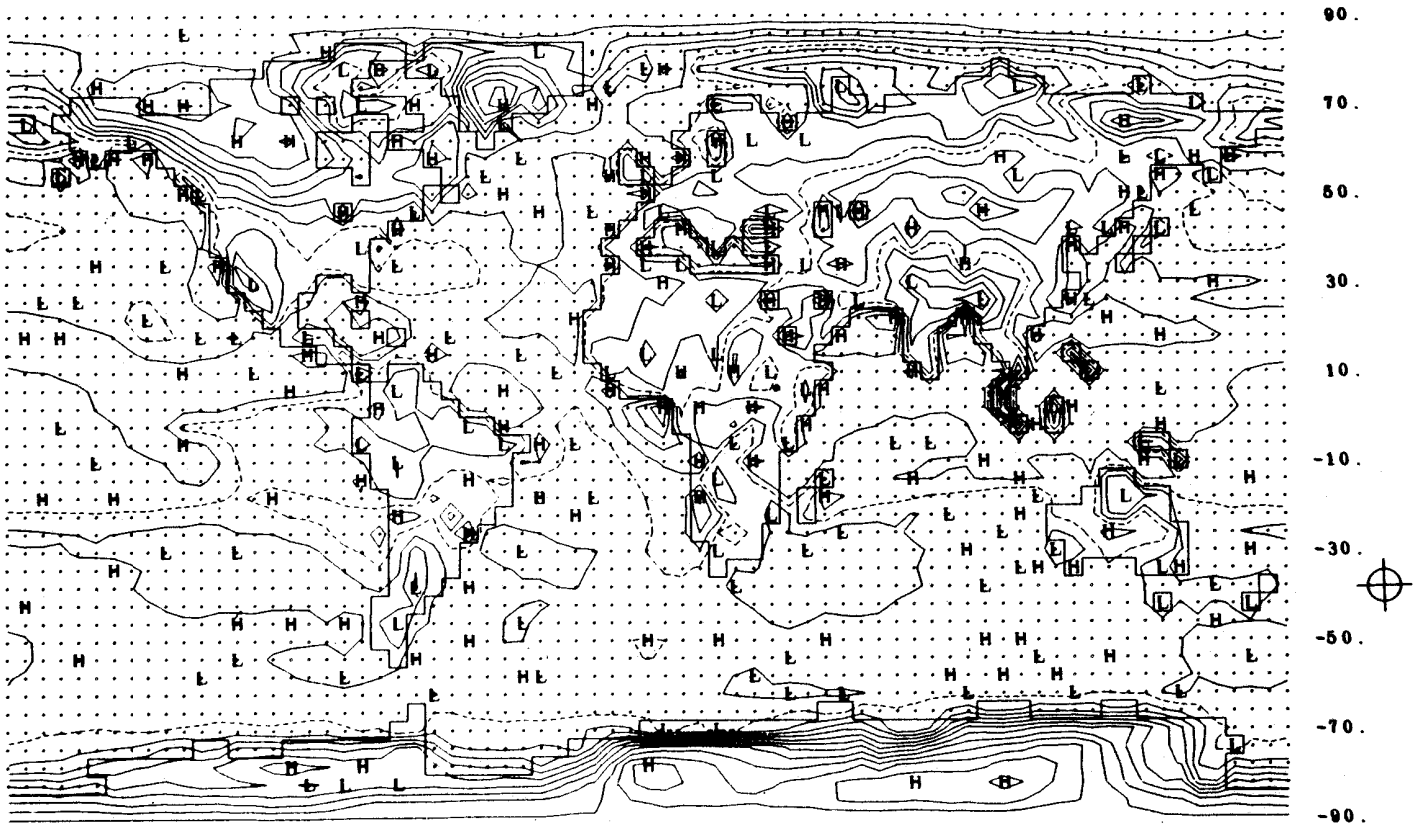

Fig. 14 -- The difference between the simulated and observed surface air temperature (Fig. 13a minus Fig. 13b). The isoline interval is 3 deg C with the zero line dashed.

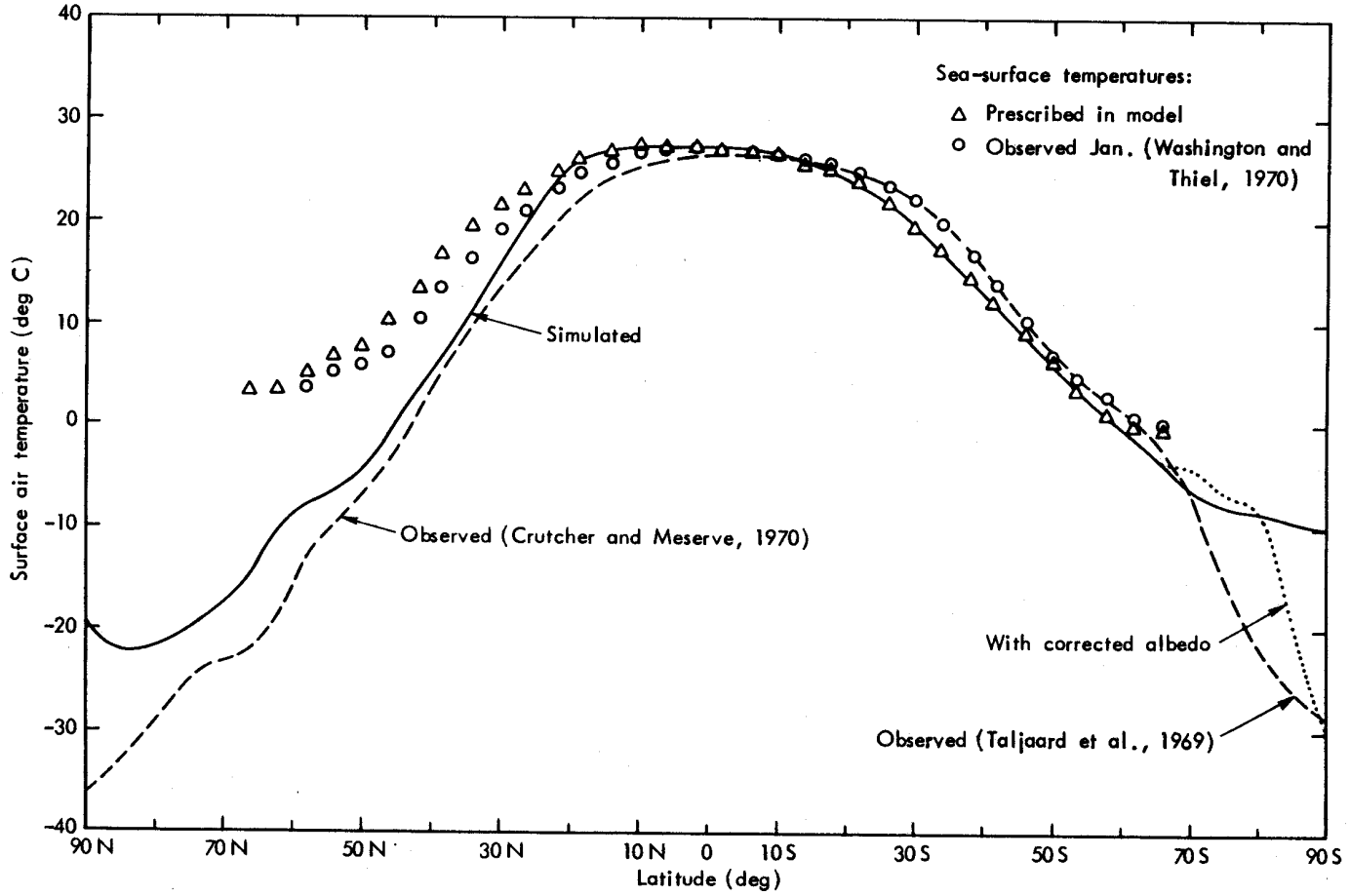

Fig. 15 -- The zonal average surface air temperature as simulated (full line) and as observed (dashed line), based on the data of Fig. 13. Also shown are the zonal averages of the prescribed sea-surface temperature (as used in the simulation) and of the observed sea-surface temperature for January from Schutz and Gates (1971), based on data of Washington and Thiel (1970).

inversion during the polar night is also the cause of the high simulated surface air temperatures over the Arctic. The large positive errors, in the range of 10 to 20 deg C, in the surface air temperature in the south polar region are mainly due to the model's use of an erroneously low albedo for snow and ice.*

On the basis of the zonal averages shown in Fig. 15, the model is seen to simulate a surface air temperature slightly too high at most latitudes, leading to a global average which is 1.2 deg C above the observed global mean value of 12.2 deg C. Only between 20°S and 65°S does the model simulate too low a zonal average surface air temperature, which may be attributed to the prescription of too low an ocean-surface temperature. This may be seen in Fig. 15, where the (fixed) sea-surface temperature used in the simulation is shown, along with the zonal average of the observed values for January; where the prescribed ocean temperature is too high, the simulated surface air temperature is also too high. Use of the observed sea-surface temperature data for January (rather than the annual average used here) would remove this error and might improve the simulation in the northern hemisphere as well.

TEMPERATURE AT 800 MB AND 400 MB

The simulated and observed average January temperatures for 800 mb and 400 mb are shown in Figs. 16 and 19, respectively. The major large-scale features of the temperature field are seen to be reasonably well simulated by the model at both levels. The principal axes of the mean January cold and warm air tongues are in approximately the observed positions, with the longitude of the maximum temperature gradient correctly simulated off the east coasts of North America and Asia. In general, however, the model has given too large an amplitude to the isotherm perturbations, and produced maximum temperature gradients which are approximately twice as great as those observed.

As was the case with the surface air temperature, the largest simulation errors at 800 mb (Fig. 17) occur over the continents, where

*See footnote, p. 8 and also Fig. 18.

errors of 5 to 10 deg C are common in higher latitudes. Over the globe, the simulated average 800-mb temperature is 1 deg C below the observed January value of 4.1 deg C. The large simulation errors over Antarctica (exceeding 26 deg C) are similar to those for surface air temperature (Fig. 14), inasmuch as the surface pressure itself is below 800 mb. This excessively warm air is due to the model's use of an erroneously low albedo, as noted above. This error is particularly evident in the zonal averages of Fig. 18, where the anomalous increase of temperature south of about 65°S coincides with the extent of the ice over the Antarctic ocean and continent (see Figs. 2 and 3).

Figure 20 records the departure of the simulated 400-mb temperature from that observed and reveals (with the exception of Antarctica) that the largest errors occur in the equatorial and subtropical latitudes, in contrast to the error patterns at both the surface (Fig. 14) and at 800 mb (Fig. 17). Over the Caribbean and over the Amazon, for example, the simulated 400-mb temperature is some 12 deg C above that observed for January. The zonally averaged 400-mb temperature in Fig. 21 is about 6 deg C above that observed between 40°N and 20°S, and contributes to a global average temperature 3.7 deg above the observed value of 24.2 deg C. Perhaps of more significance is the model's simulation of a midlatitude meridional temperature *gradient*, which is about 60 percent too great in both hemispheres (see Fig. 21). This error is reflected in the mean zonal winds discussed below, and is most likely related to the model's simulation of excessive convective precipitation in the lower latitudes, with its upper level receiving too much (convective) latent heating.

As was the case at the surface and at 800 mb, the air temperature at 400 mb over Antarctica is systematically higher than that observed. South of about 70°S the simulated meridional temperature gradient is of the wrong sign, with a 10-deg C error at 90°S (Fig. 21). This discrepancy is due to the albedo error noted earlier.

ZONAL WIND AT 800 MB AND 400 MB

The simulated January zonal (u) wind component at 800 mb and 400 mb is shown in Figs. 22 and 23. Because of the lack of corresponding observed wind data, global maps of the observed values and the simulation

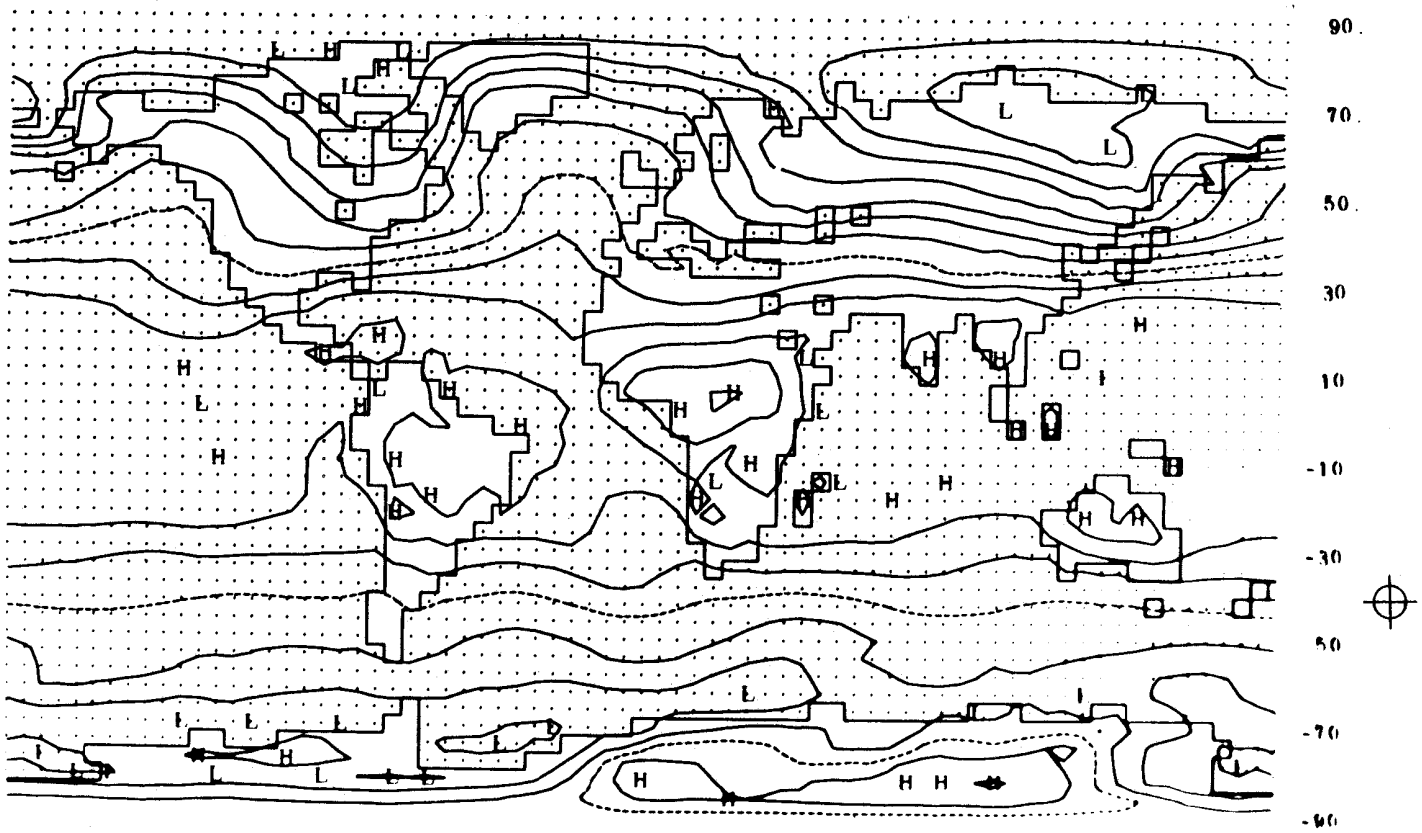

Fig. 16a -- The simulated temperature for January at 800 mb, with isolines at 5-deg C intervals and the 0-deg C isotherm dashed.

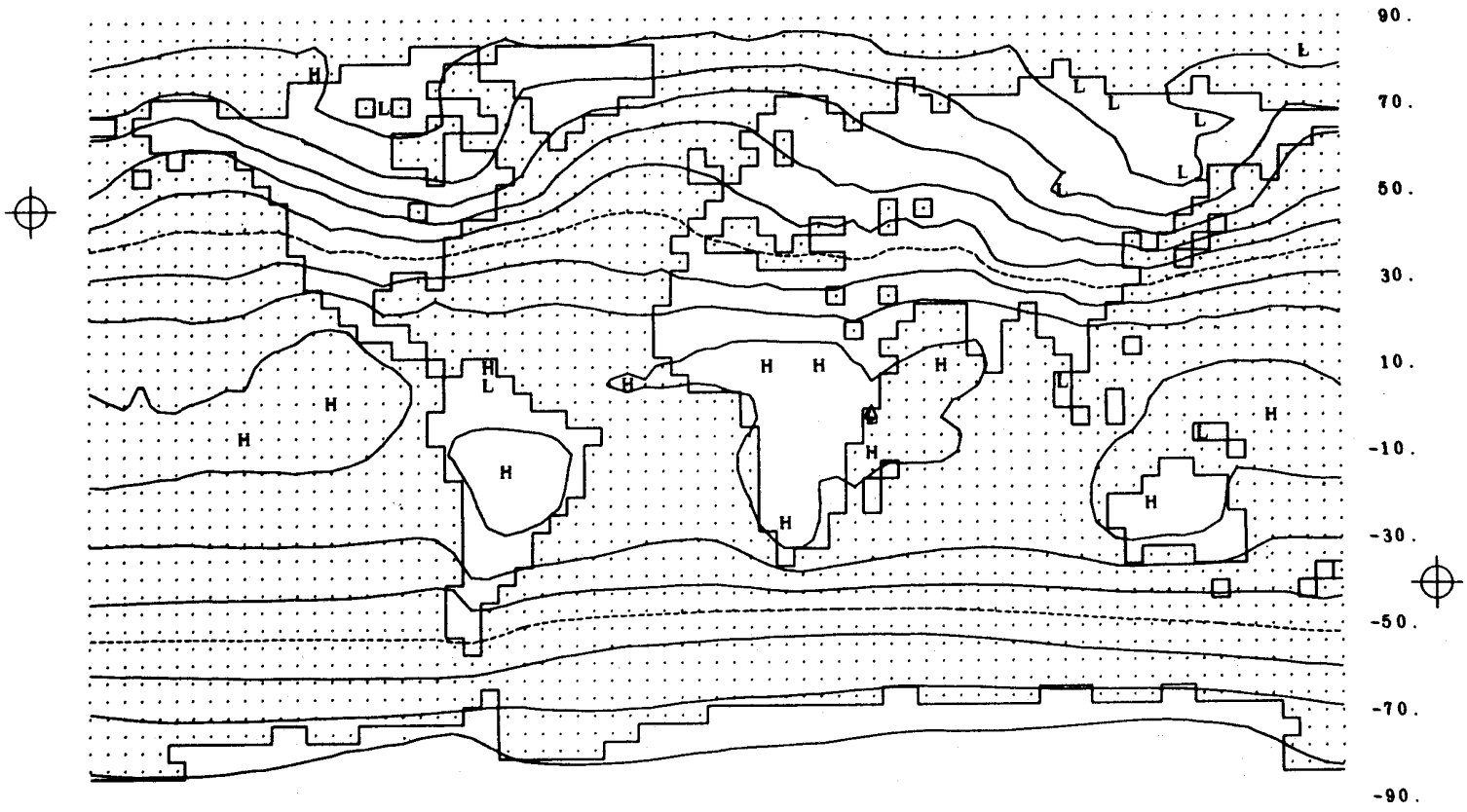

Fig. 16b -- The observed temperature for January at 800 mb, with isolines at 5-deg C intervals and the 0-deg C isotherm dashed. Based on data of Crutcher and Meserve (1970) and Taljaard et al. (1969) as summarized by Schutz and Gates (1971).

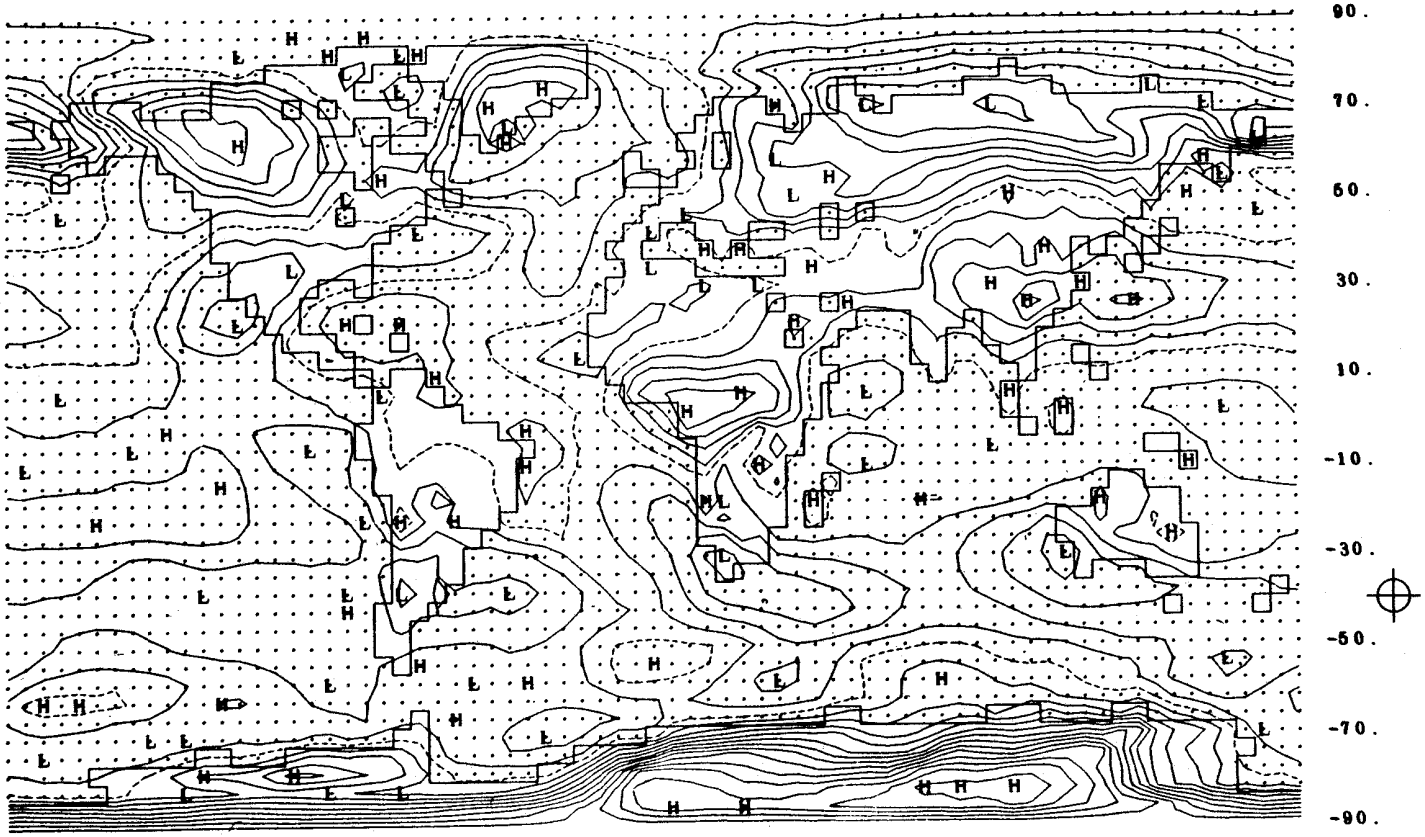

Fig. 17 -- The difference between the simulated and observed 800-mb temperature (Fig. 16a minus Fig. 16b). The isoline interval is 2 deg C with the 0-deg C line dashed.

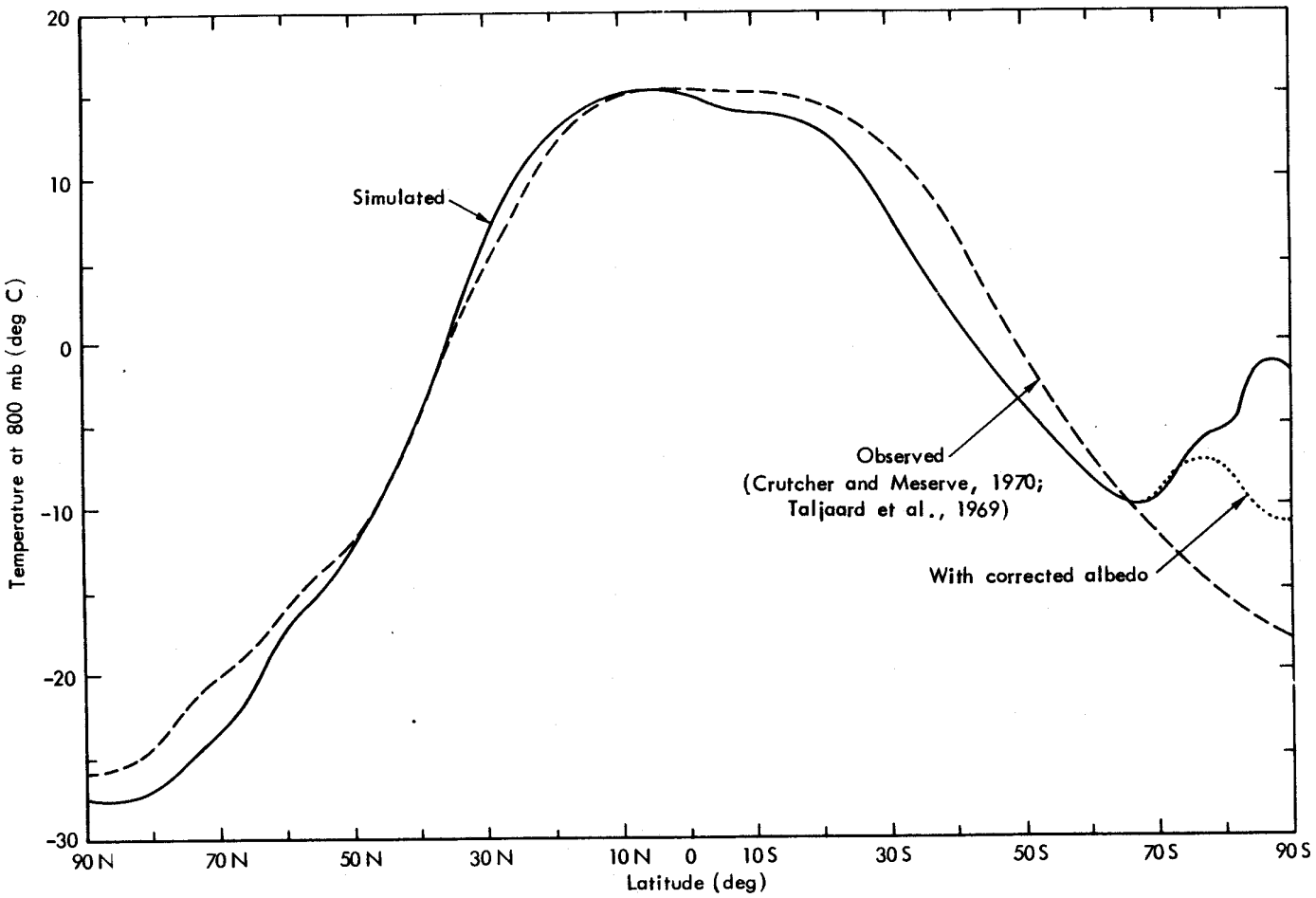

Fig. 18 -- The zonal average January 800-mb temperature as simulated (full line) and as observed (dashed line), based on the data of Fig. 16.

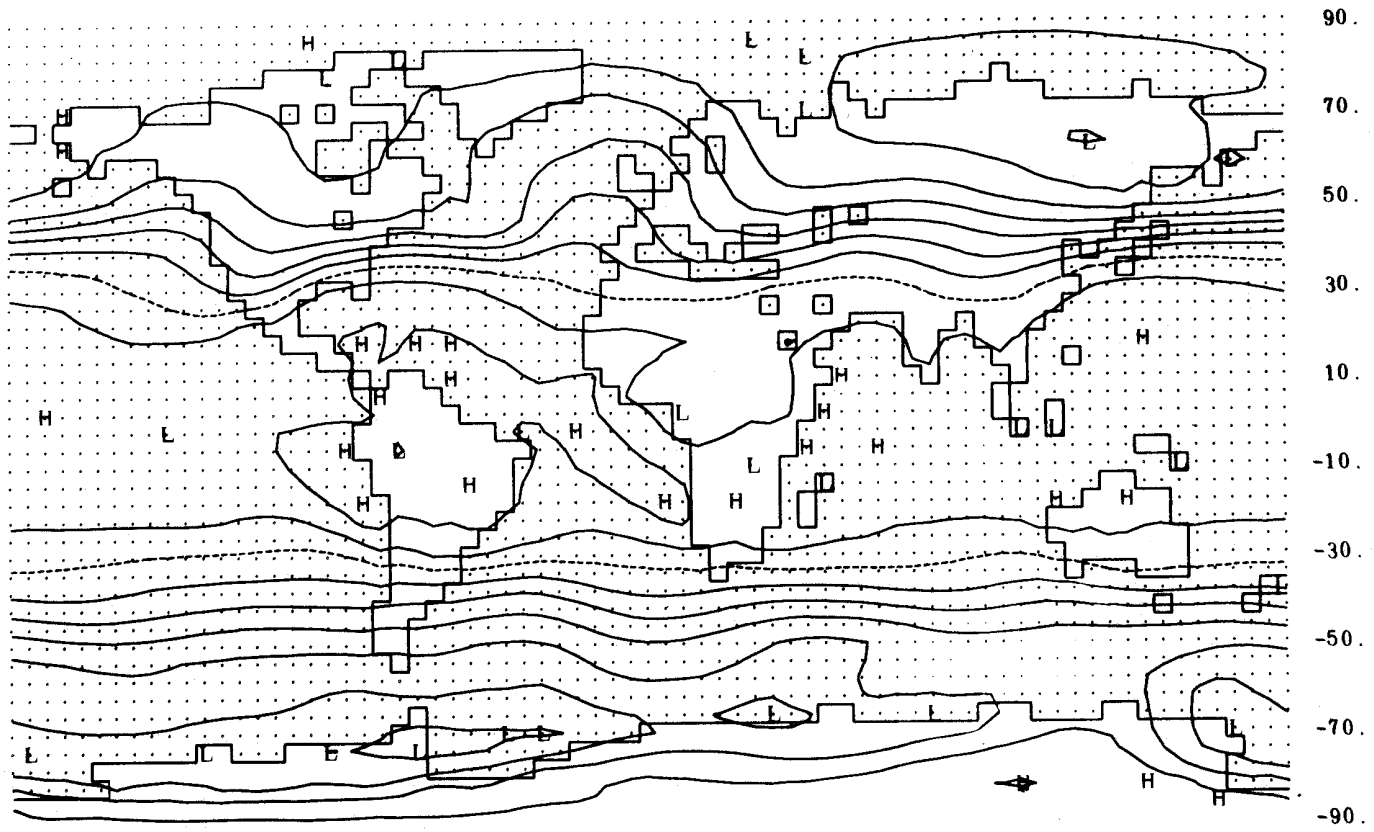

Fig. 19a -- The simulated temperature for January at 400 mb, with isolines every 5 deg C and the -20-deg C isotherm dashed.

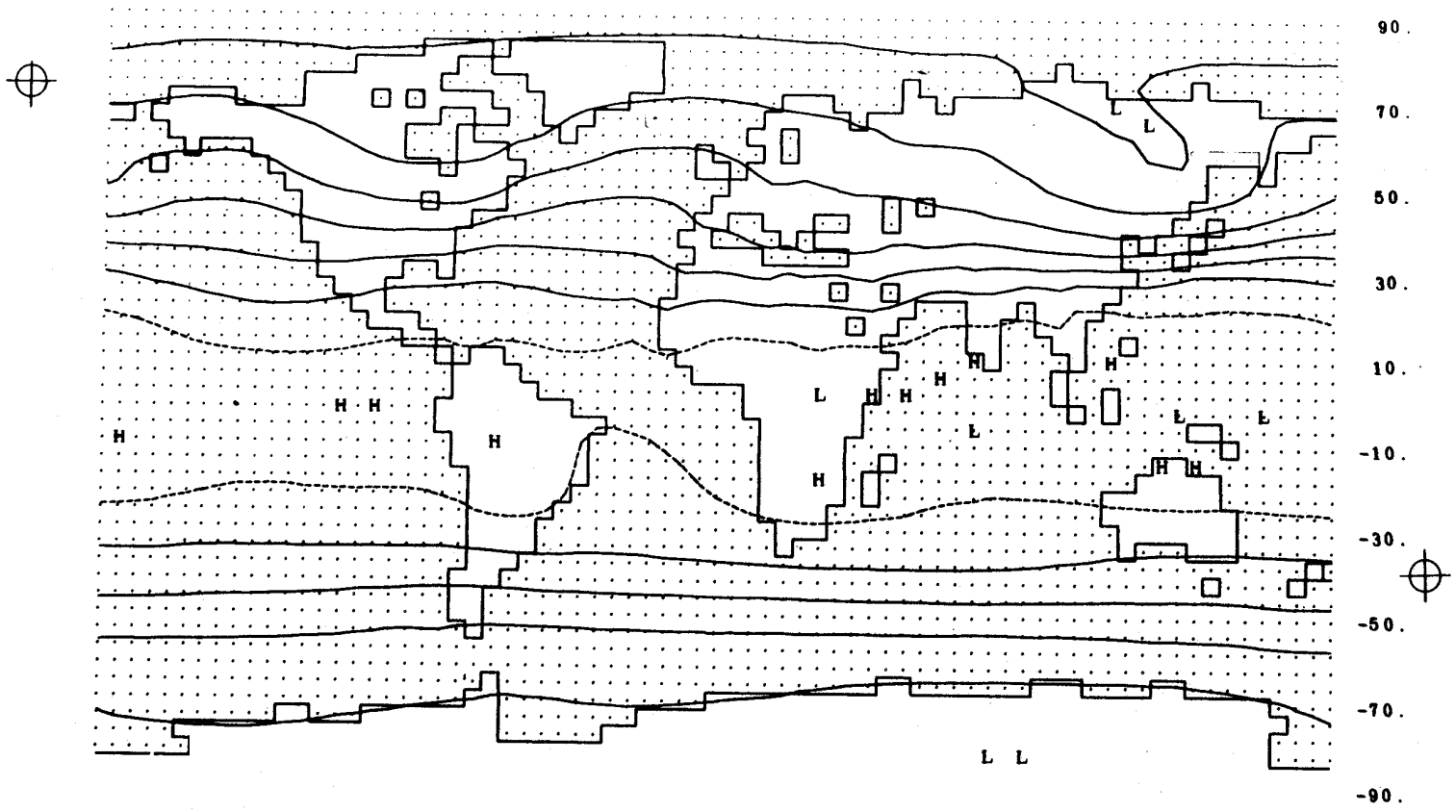

Fig. 19b -- The observed temperature for January at 400 mb, with isolines every 5 deg C and the -20-deg C isotherm dashed. Based on data of Crutcher and Meserve (1970) and Taljaard et al. (1969) as summarized by Schutz and Gates (1971).

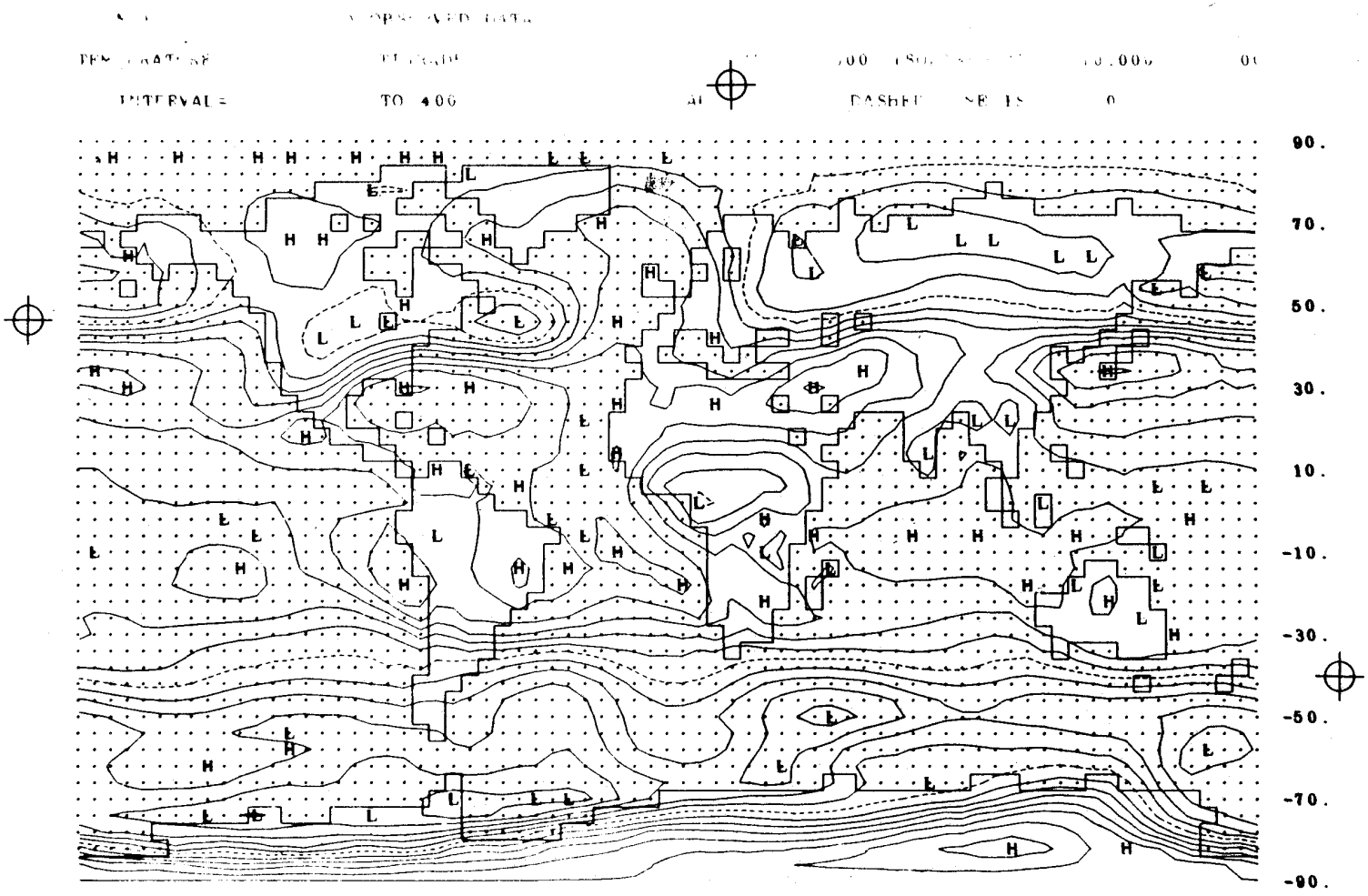

Fig. 20 -- The difference between the simulated and observed 400-mb temperature (Fig. 19a minus Fig. 19b). The isoline interval is 2 deg C with the 0-deg C line dashed.

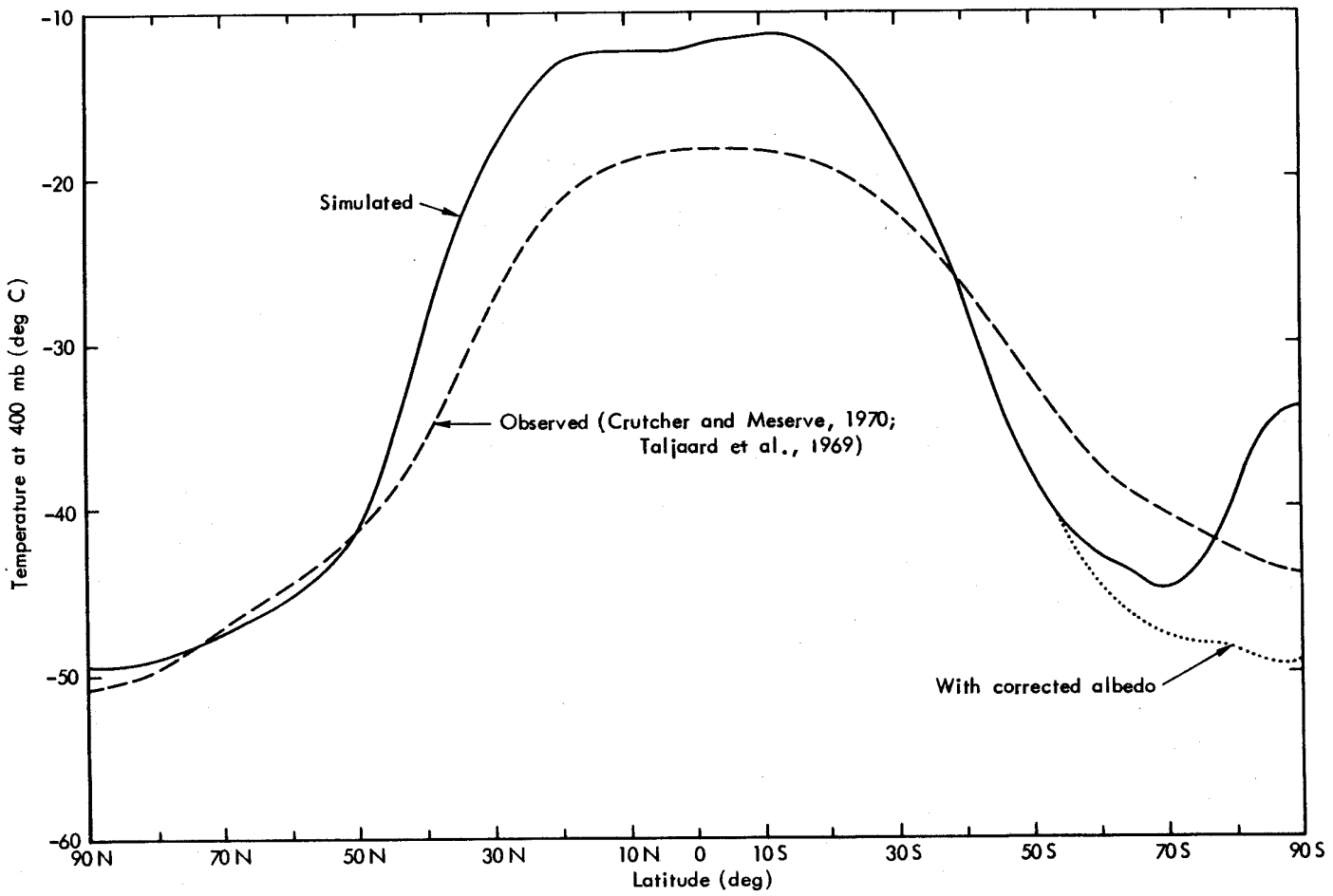

Fig. 21 -- The zonal average January temperature at 400 mb as simulated (full line) and as observed (dashed line), based on the data of Fig. 19.

errors cannot be given. In general, the simulated mean zonal winds clearly show the midlatitude jet streams, with maximum westerlies off the east coasts of North America and Asia, and with the westerly winds generally increasing with height. These simulations correspond reasonably well with the observed mean geostrophic zonal wind, which may be calculated from the observed geopotential fields (Figs. 7b and 10b), and with the available observed winds in the northern hemisphere shown by Schutz and Gates (1971). The strongest simulated zonal winds near 40°N in Figs. 22 and 23, however, are approximately twice the strength of either of these observed measures. In the lower latitudes, the model developed weak easterlies between about 25°N and 20°S at 800 mb, and between about 10°N and 10°S at 400 mb.

In spite of the sparsity of the observed data, a useful quantitative comparison can be made with zonal averages as in Figs. 24 and 25. At 800 mb the agreement with observation may be considered generally good, although the southern hemisphere westerlies and the northern hemisphere easterlies are about 5 deg too far north. A more important simulation error, however, is the systematic overprediction of the speed of the northern hemisphere westerlies; the simulated 800-mb maximum zonal wind speed of 14 m sec^{-1} at 40°N is nearly twice the 8 m sec^{-1} speed of the strongest observed mean zonal winds (either actual or geostrophic). At 400 mb the speed of the simulated maximum zonal westerlies at 40°N is 35 m sec^{-1}, a 67 percent overprediction of Crutcher's (1961) maximum observed zonal wind of 21 m sec^{-1} (at 35°N) and a 25 percent overprediction of the maximum mean zonal geostrophic wind of 28 m sec^{-1} (Crutcher and Meserve, 1970). The maximum westerlies are also simulated between 5 and 10 deg too far north. These errors are related to the excessively strong gradient of geopotential noted earlier, which in turn is related to the excess warmth of the tropical atmosphere. The accompanying increased meridional temperature gradient thereby contributes to the intensification of the midlatitude disturbances.

It is also of interest to compare the simulated and observed vertical wind shears. From Figs. 24 and 25, the maximum difference between the simulated zonal winds at 400 mb and 800 mb is about 22 m sec^{-1} at 36°N, and about 19 m sec^{-1} at 35°S. The maximum shear of the observed

zonal winds in the northern hemisphere between 400 mb and 800 mb occurs near 35°N and is about 16 m sec^{-1} (Crutcher, 1961). The maximum simulated shear is thus about 37 percent higher than that observed (in the northern hemisphere). In terms of the vertical shear of the observed *geostrophic* zonal winds, the maximum differences between 400 mb and 800 mb are about 20 m sec^{-1} (at 36°N) and about 13 m sec^{-1} (at 48°S), according to the data of Crutcher and Meserve (1970) as summarized by Schutz and Gates (1971). These agree quite well with the model's calculations, which may therefore be said to correctly simulate the observed thermal wind balance in the troposphere.

The most direct way to reduce the excessive strength of the simulated zonal winds (while possibly preserving the model's nearly correct vertical wind shear) would seem to be either to increase the surface friction (see Gates, 1972) or to introduce lateral eddy viscosity that is not now used in the model (see Gates et al., 1971).

MERIDIONAL WIND AT 800 MB AND 400 MB

The simulated January meridional (v) wind component at 800 mb and at 400 mb is shown in Figs. 26 and 27. As with the zonal wind, available data are not sufficient to permit a detailed global comparison with observation. In general, the mean meridional winds have maximum strength in connection with the standing long waves in the middle latitudes of the northern hemisphere. Here the simulated winds agree reasonably well, in both position and magnitude, with the available observations in the northern hemisphere and with the global geostrophic winds as given by Schutz and Gates (1971). Generally, the pattern of the mean meridional wind shows coherence between the levels 400 mb and 800 mb, with approximately twice as great speed at the upper level. The prominent feature is the one associated with the Icelandic low, where the mean January meridional wind exceeds 20 m sec^{-1} at 400 mb. The mean meridional winds in the tropics and in most of the southern hemisphere are relatively weak, although there is still a noticeable resemblance between the winds at both levels.

The zonal averages of the meridional winds present a somewhat different picture (Figs. 28 and 29). Here the simulated mean meridional

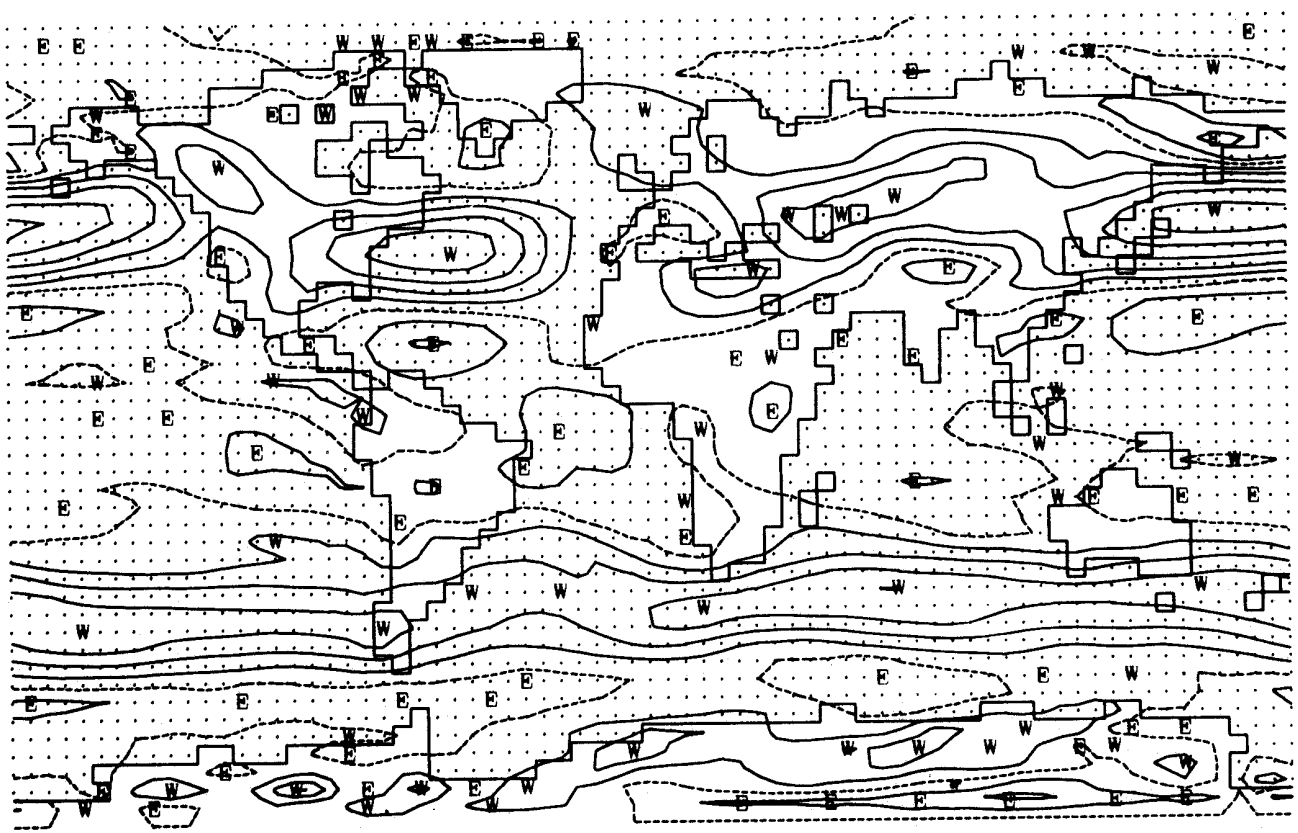

Fig. 22 -- The zonal wind at 800 mb simulated for January. The isolines are at intervals of 5 m sec^{-1}, with the zero line dashed. The symbols W and E denote local maxima of winds from the west and east.

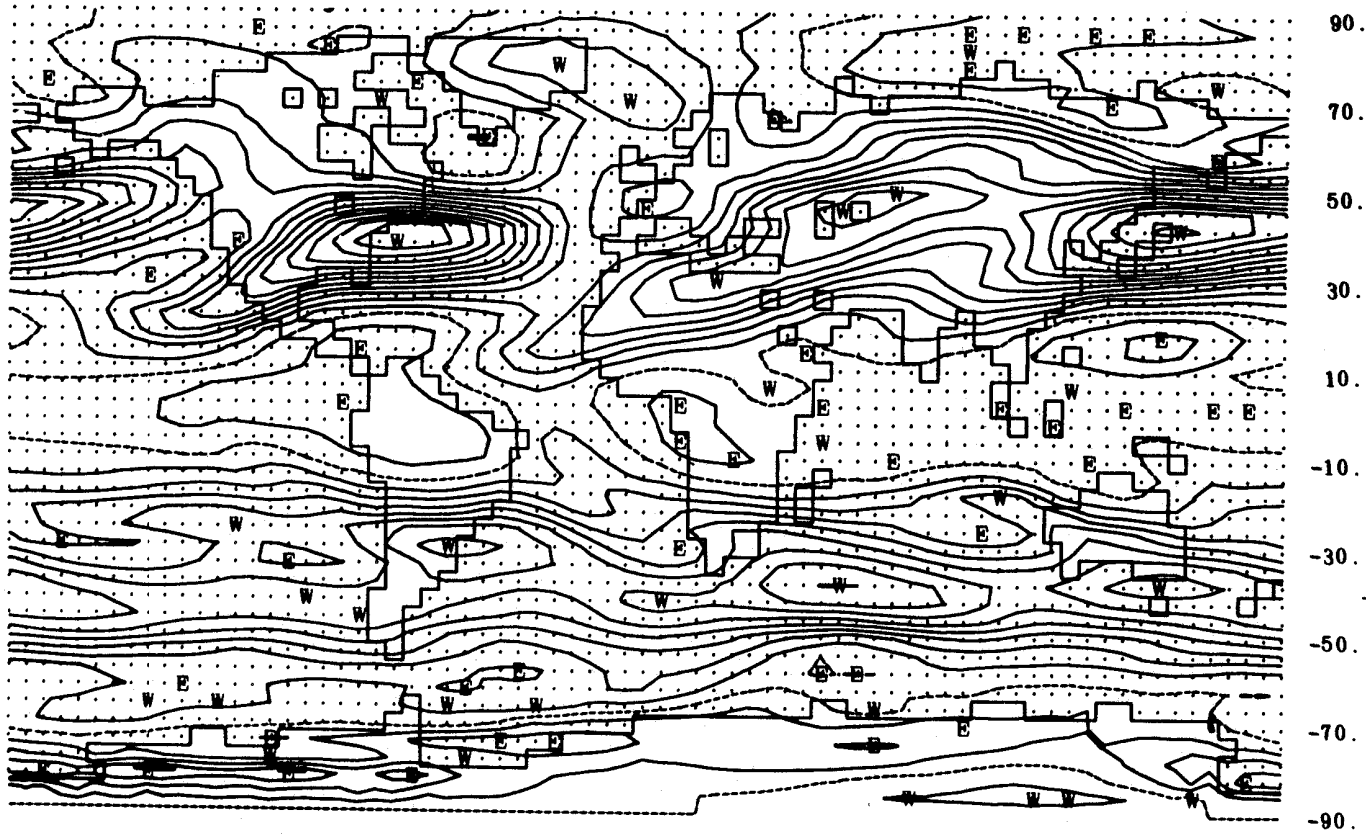

Fig. 23 -- The zonal wind at 400 mb simulated for January. See also Fig. 22.

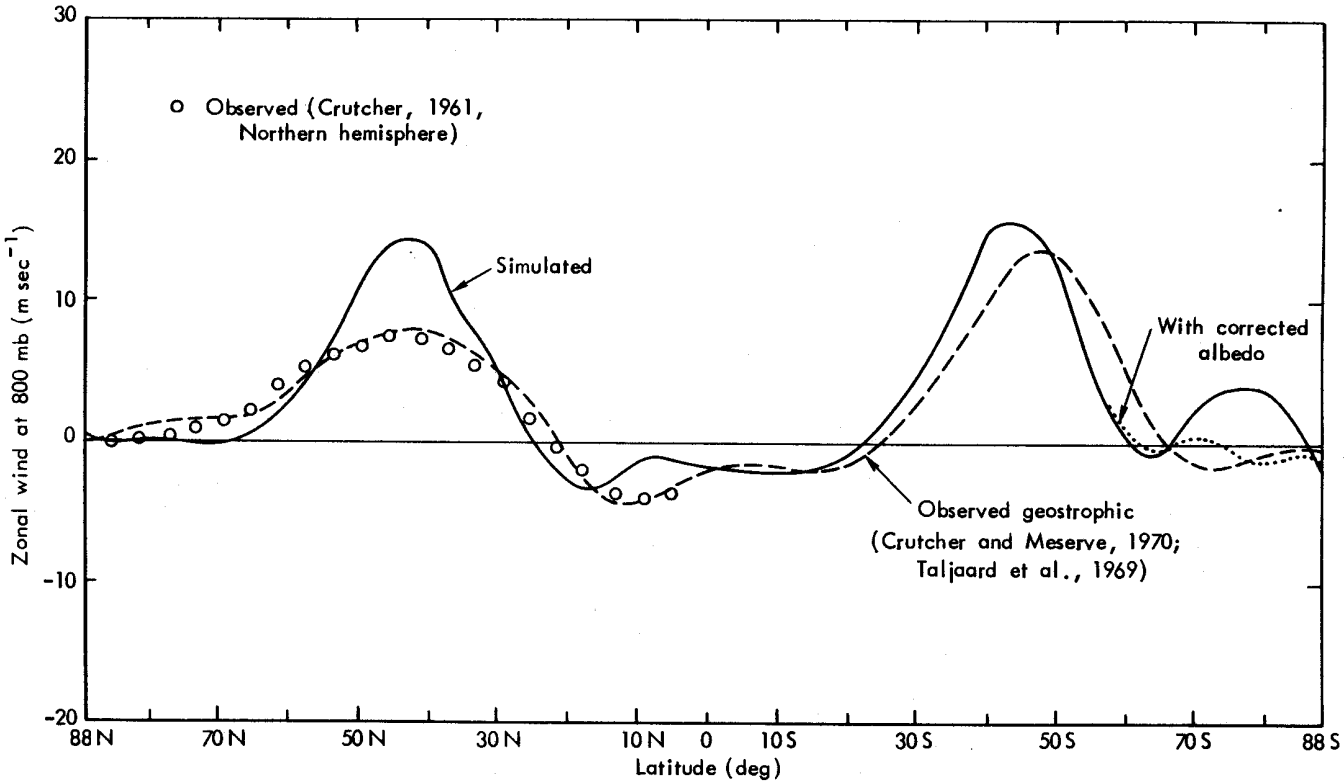

Fig. 24 -- The zonal average of the mean zonal winds at 800 mb simulated for January (full line), together with the distribution of the corresponding observed geostrophic winds (dashed line) as given by Schutz and Gates (1971) based on data of Crutcher and Meserve (1970) and Taljaard et al. (1969). Also shown by the open circles in the northern hemisphere are the zonal averages of the observed zonal wind (for December, January, February) from Schutz and Gates (1971) based on data of Crutcher (1961).

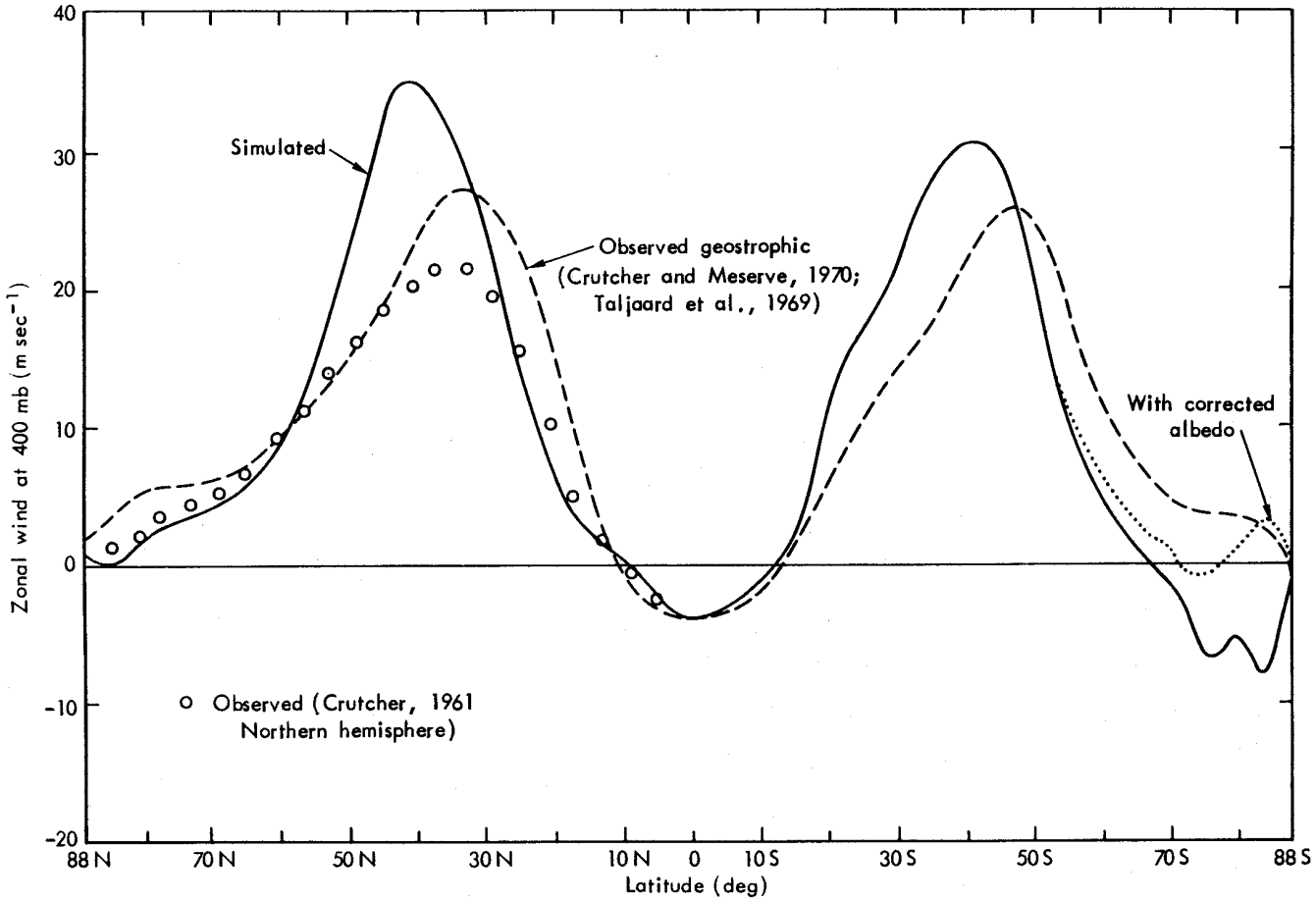

Fig. 25 -- The zonal average of the mean zonal winds at 400 mb simulated for January (full line), together with the distribution of the corresponding observed geostrophic winds (dashed line) as given by Schutz and Gates (1971) based on data of Crutcher and Meserve (1970) and Taljaard et al. (1969). Also shown by the open circles in the northern hemisphere are the zonal averages of the observed zonal wind (for December, January, February) from Schutz and Gates (1971) based on data of Crutcher (1961).

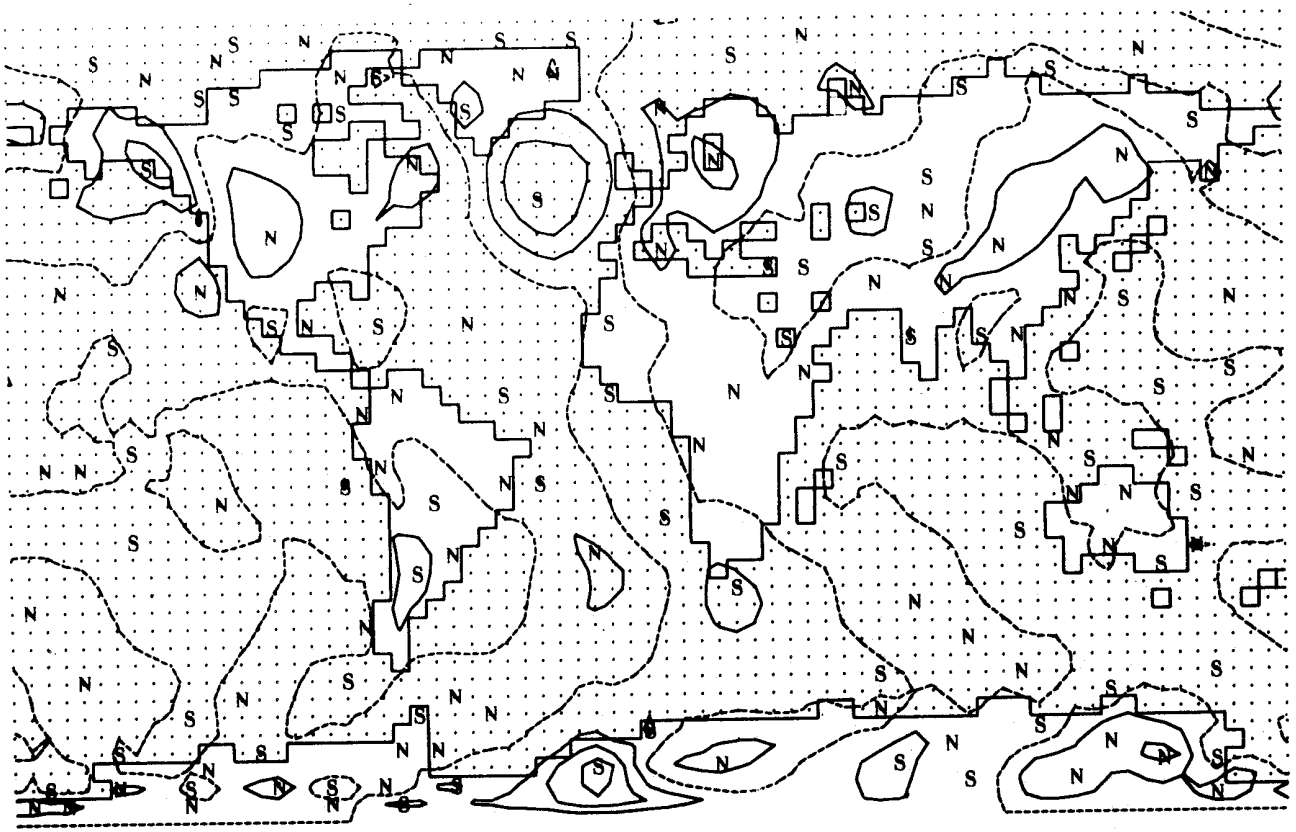

Fig. 26 -- The meridional wind at 800 mb simulated for January. The isolines are at intervals of 5 m sec^{-1}, with the zero line dashed. The symbols N and S denote local maxima of winds from the north and south.

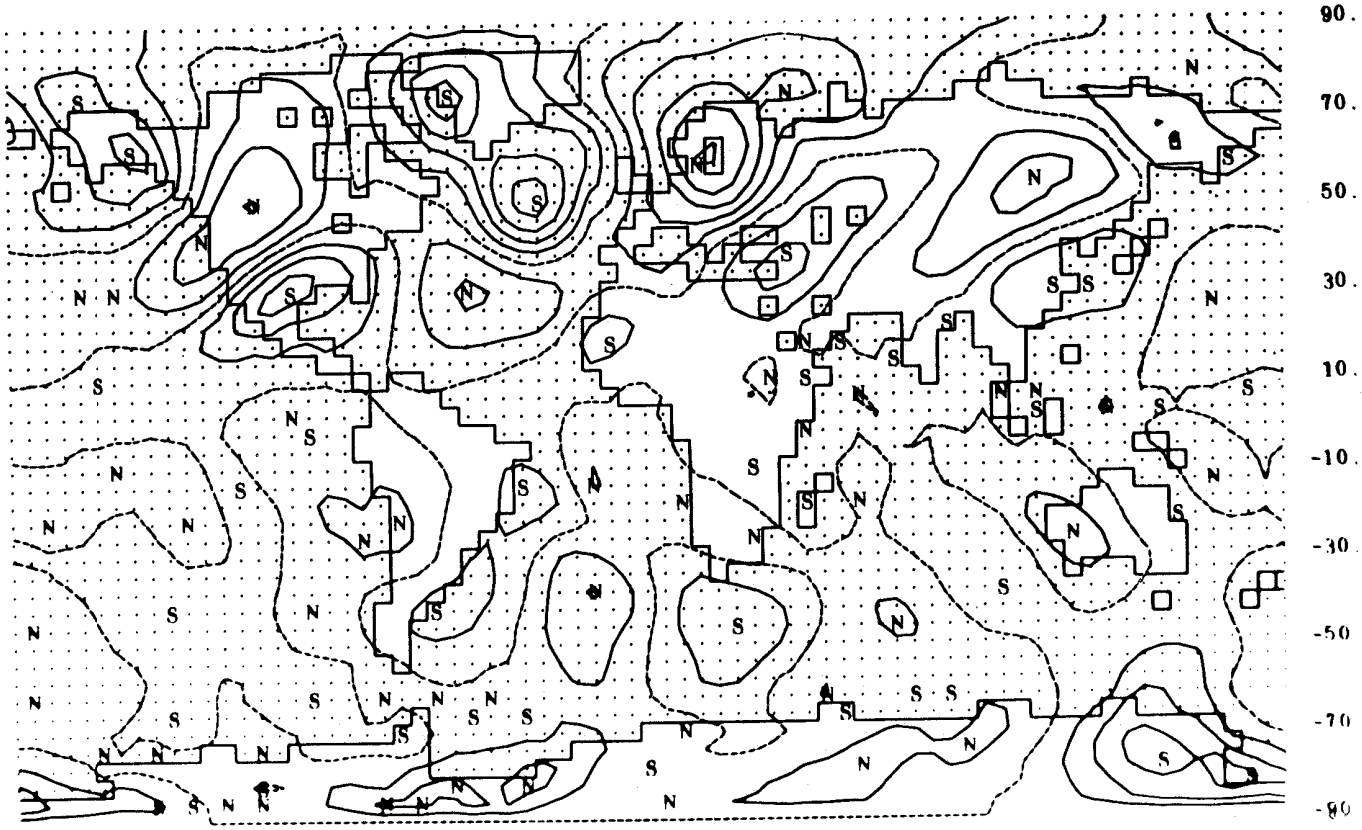

Fig. 27 -- The meridional wind at 400 mb simulated for January. See also Fig. 26.

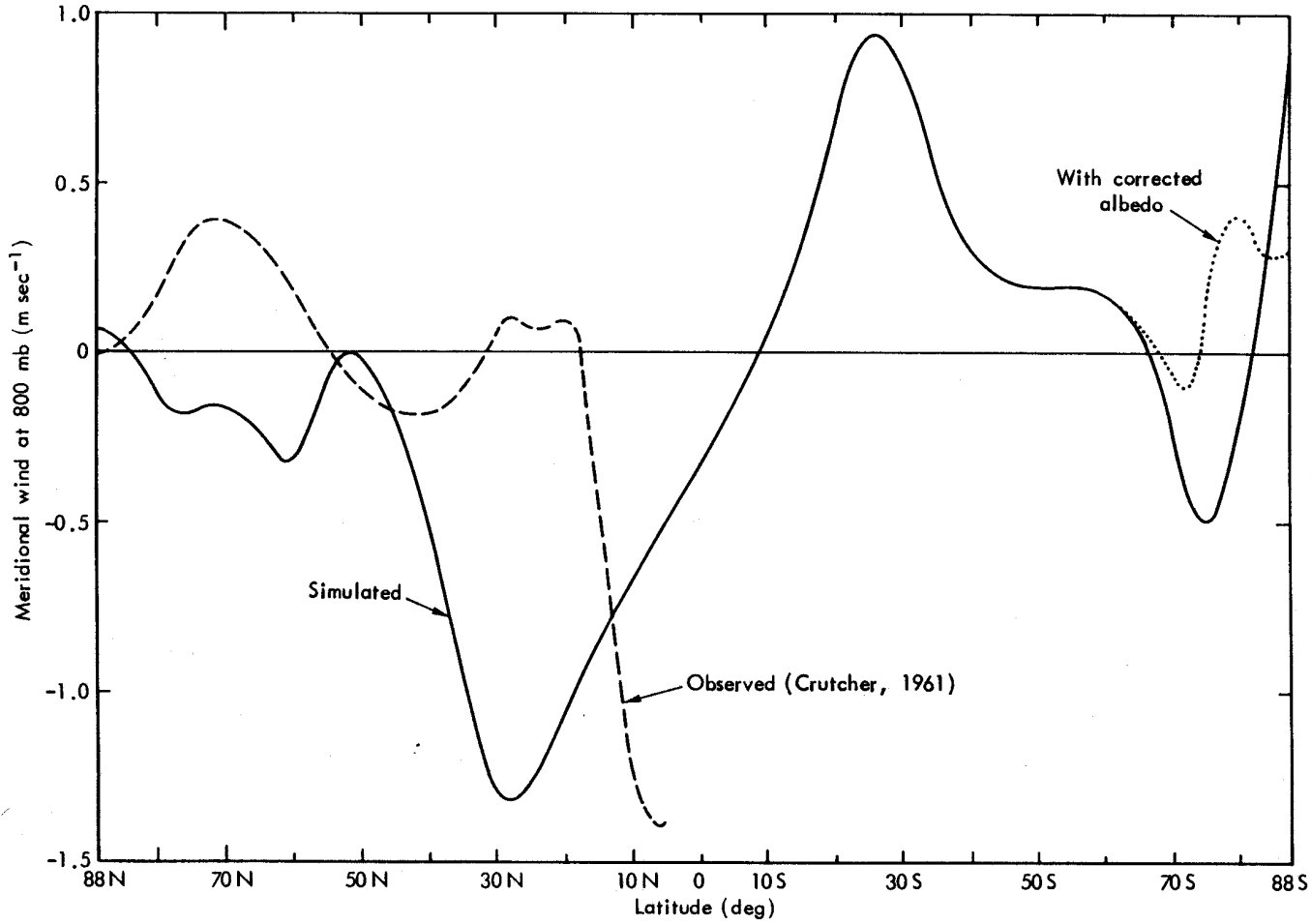

Fig. 28 -- The zonal average of the mean meridional winds at 800 mb simulated for January (full line), with the corresponding observed winds (dashed line) in the northern hemisphere. From Schutz and Gates (1971), based on data of Crutcher (1961).

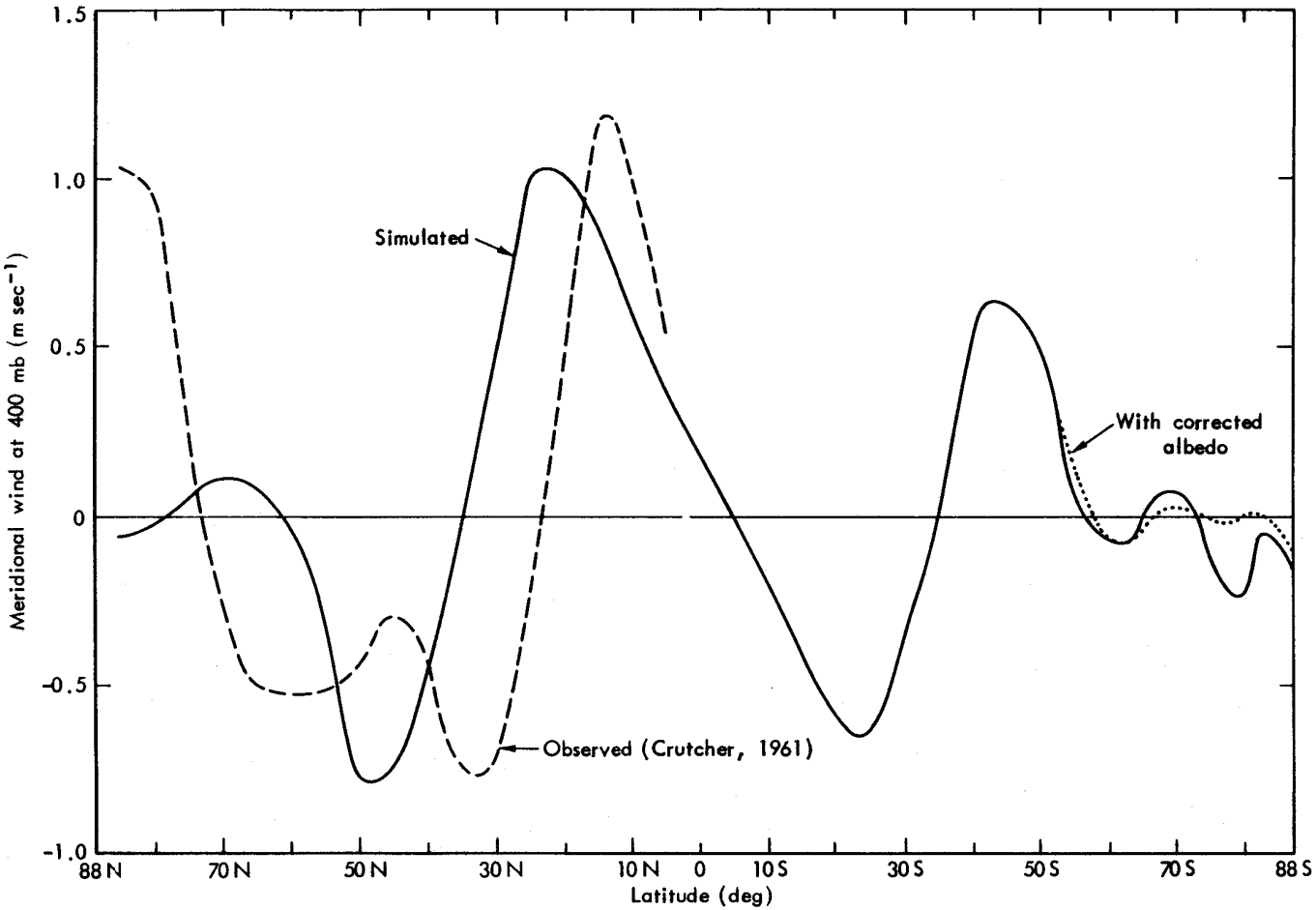

Fig. 29 -- The zonal average of the mean meridional winds at 400 mb simulated for January (full line), with the corresponding observed winds (dashed line) in the northern hemisphere. From Schutz and Gates (1971), based on data of Crutcher (1961).

flow is dominated by the components of the Hadley circulation in the tropics, where the zonally averaged meridional wind exceeds 1 m sec^{-1}. A maximum southward motion is simulated between 20°N and 30°N at 800 mb (Fig. 28), and a nearly equal maximum northward flow at 400 mb (Fig. 29) at the same latitudes. A reversed and slightly weaker circulation is simulated in the southern hemisphere between 20°S and 30°S at both levels. These motions are essentially nongeostrophic, since the zonally averaged meridional geostrophic wind vanishes identically. In comparison with the zonal mean of the available observed meridional winds for the northern hemisphere [as given by Schutz and Gates (1971), based on data of Crutcher (1961)], the simulated circulation is systematically displaced toward the north. At 800 mb (Fig. 28) the maximum equatorward flow is simulated some 20 deg north of the observed maximum at 5°N, while at 400 mb the maximum poleward flow is simulated about 10 deg too far north. A northward displacement is also evident in other features of the mean meridional winds, although the simulated speeds are in reasonably good agreement with those observed (in the northern hemisphere).

VERTICAL MOTION AND MASS FLUX

The mean meridional velocities at 400 mb and 800 mb, however, do not portray the mass flux associated with the mean meridional circulation in the model, because of the varying pressure at the earth's surface. To examine this flux, we may write the continuity equation in the form

$$\frac{\partial \pi}{\partial t} + \nabla \cdot \pi \vec{V} + \frac{\partial}{\partial \sigma}(\pi \dot{\sigma}) = 0 \tag{7}$$

where the symbols are as previously defined. Denoting a time average by $\overline{(\ )}$ and a zonal average by [ ], this becomes

$$\frac{\partial}{\partial \varphi}[a \cos \varphi \, \overline{\pi v}] + \frac{\partial}{\partial \sigma}[a^2 \cos \varphi \, \overline{\pi \dot{\sigma}}] = 0 \tag{8}$$

assuming $\overline{(\partial[\pi]/\partial t)} = 0$ over the (30-day) time period. A streamfunction ψ for the total mass flux may then be defined for which

$$2\pi' a^2 \cos\varphi\, [\overline{\pi\dot{\sigma}}]/g = -\partial\psi/\partial\varphi \tag{9a}$$

$$2\pi' a \cos\varphi\, [\overline{\pi v}]/g = \partial\psi/\partial\sigma \tag{9b}$$

where a is the earth's radius, φ is latitude, g is gravity, and $\pi' \equiv 3.14...$ (to avoid confusion with $\pi \equiv p_s - p_T$ previously defined).

We may use either of these expressions to find ψ, depending upon the data available. As suggested by Mintz, I have used (9a) and found ψ by an integration with respect to latitude. Between two latitudes φ_1 and φ_2, we thus have

$$\psi_2 - \psi_1 = -\frac{2\pi' a^2}{g} \int_{\varphi_1}^{\varphi_2} \cos\varphi\, [\overline{\pi\dot{\sigma}}_2]\, d\varphi \tag{10}$$

With the condition $\psi = 0$ at the poles and at both $\sigma = 0$ and $\sigma = 1$, this expression was used to calculate the streamfunction distribution shown in Fig. 30b. The values of $[\overline{\pi\dot{\sigma}}_2]$ used for this purpose are shown in Fig. 30a, as given by the model's mean January simulation. Since ψ is found only at the model's midlevel, the simulated streamfunction is symmetric about $\sigma = 1/2$. A comparison with the observed mass flux streamfunction given by Newell et al. (1970), also shown in Fig. 30b, reveals that the simulated mean meridional circulation has a number of realistic features.

We note in particular that the strength of the simulated northern-hemisphere Hadley circulation (152×10^{12} g sec^{-1}) is close to that given by Newell et al. (1970) for December, January, and February, although it is somewhat below the values 180×10^{12} g sec^{-1} and 230×10^{12} g sec^{-1} given by Oort and Rasmusson (1970) for January and by Palmén and Newton (1969) for the northern winter. The position of the simulated northern Hadley cell, however, is approximately 15 deg too far north. The model's northern Ferrel cell is too weak and is much narrower than that observed, although it is simulated at approximately the correct mean latitude. This may be due to the model's tendency to underestimate the strength

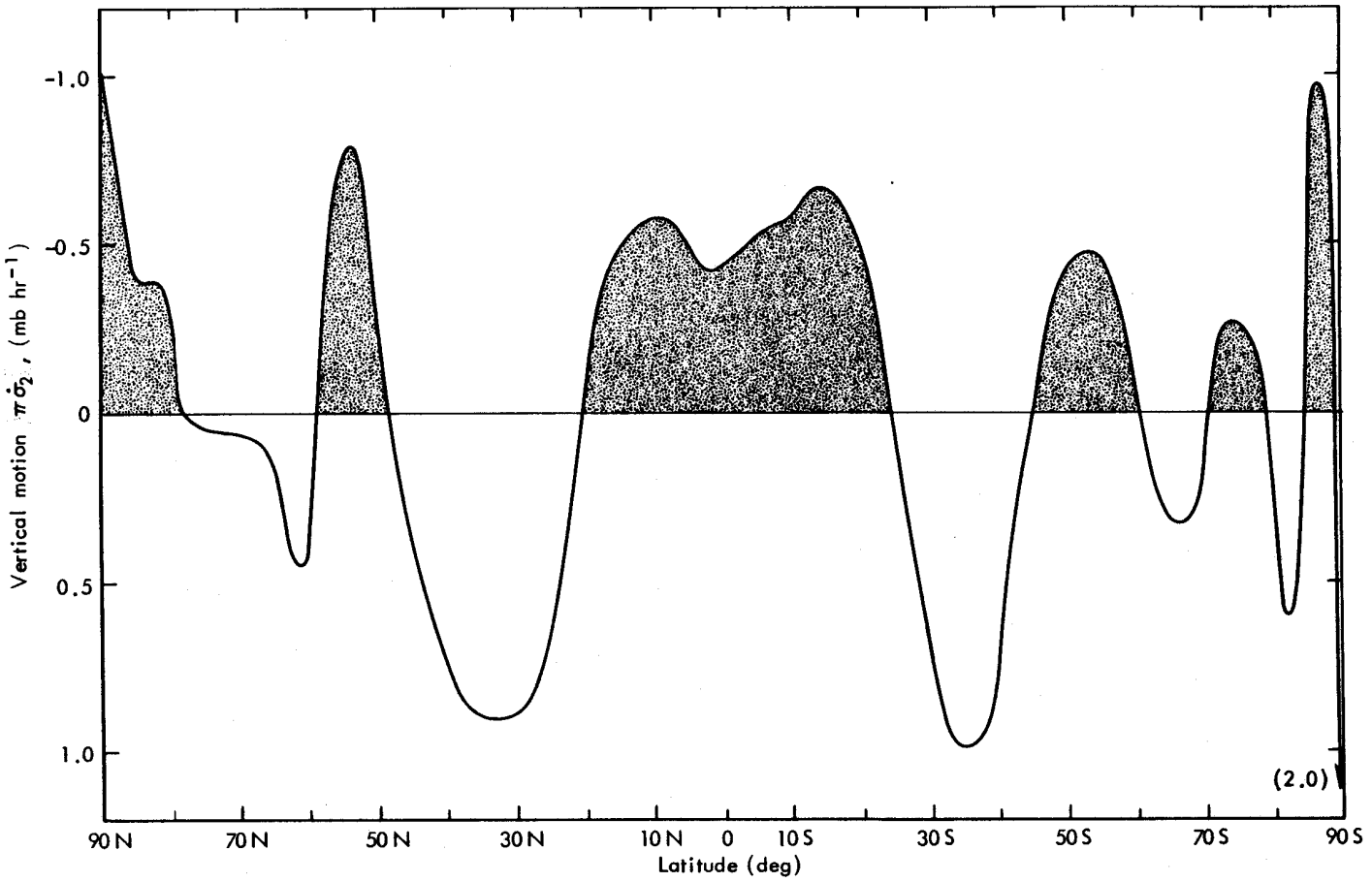

Fig. 30a -- The zonal average of the mean vertical motion simulated for January, as given by the measure $\pi\dot{\sigma}_2$. Neglecting surface pressure variations, 1 mb hr^{-1} here corresponds to a vertical velocity of about 0.4 cm sec^{-1} at 600 mb. The shading denotes regions of upward vertical motion (see also Fig. 30b).

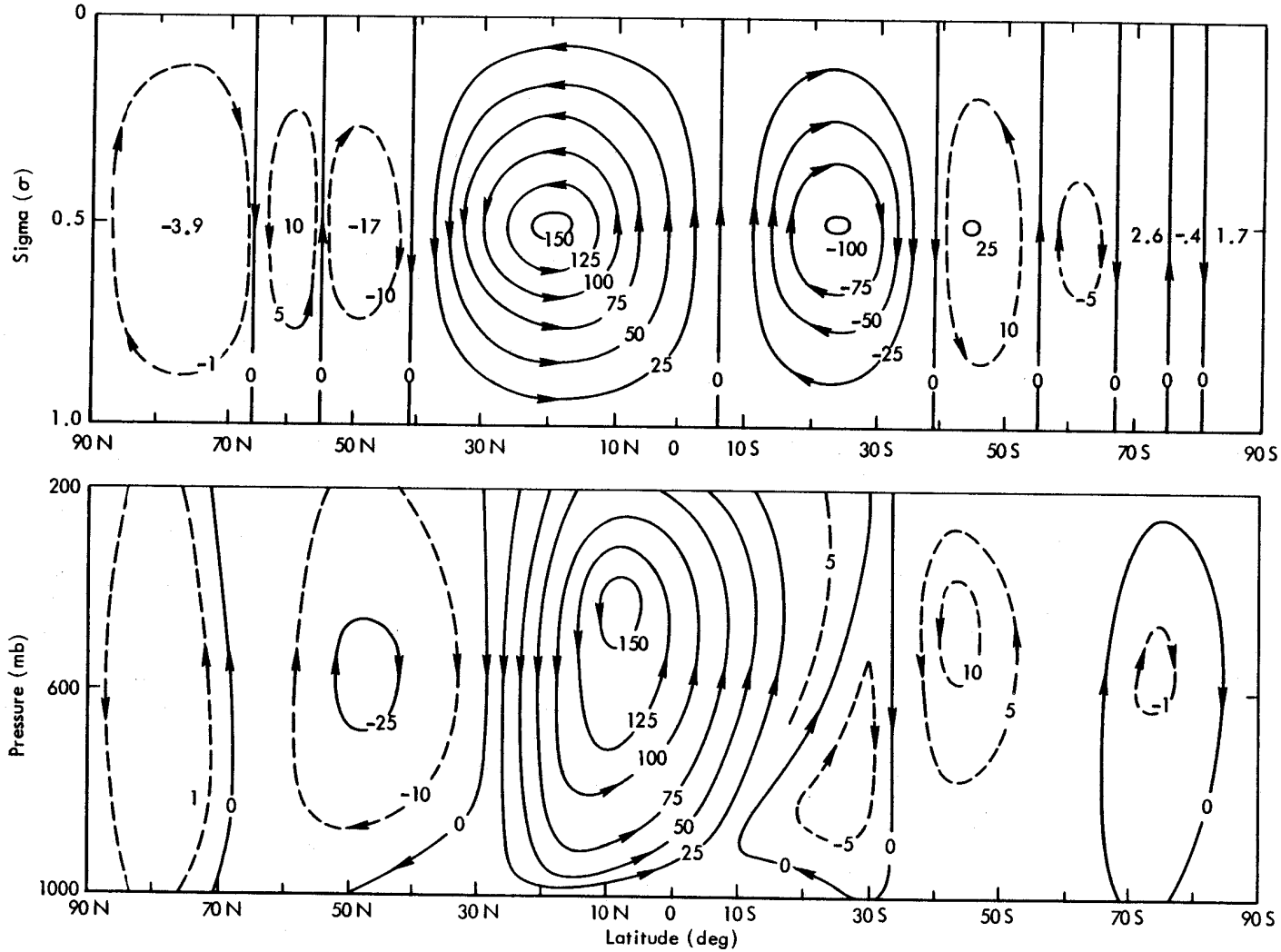

Fig. 30b -- The streamfunction for the time-mean, zonally averaged mass flux in 10^{12} g sec^{-1}. That simulated for January is shown above (symmetric about $\sigma = 1/2$), and that observed (for December, January, February) is shown below as given by Newell et al. (1970). The direction of flow is given by the arrows.

of the transient midlatitude cyclones noted earlier, with which the bulk of the nongeostrophic transport in the Ferrel cell may be associated.

In the southern hemisphere, the simulated strength (and width) of the Hadley circulation is much greater than that observed, at least according to Newell et al. (1970). The cause of this discrepancy is not clear, although it is interesting to note that the southern Ferrel cell (as well as the weaker cells south of it) is also simulated with too great a strength. It may be that the model systematically overestimates the strength of the southern hemisphere circulation for some reason (such as the use of too low a sea-surface temperature), or that the available observations in the southern hemisphere are insufficient to determine the mean meridional mass flux adequately.

After the mass flux has been determined, the mean mass-weighted meridional velocity between $\sigma = 1$ and $\sigma = 1/2$ may be found from (9b) as

$$[\bar{v}_3] \simeq \frac{[\overline{\pi v_3}]}{[\bar{\pi}]} = -2\psi g(2\pi' a \cos\varphi\,[\bar{\pi}])^{-1} \tag{11}$$

with $[\bar{v}_1]$ between the levels $\sigma = 1/2$ and $\sigma = 0$ (or 200 mb) given by a change of sign. In the northern Hadley cell, for example, we thus find a maximum $[\bar{v}_3] \simeq -1.0$ m sec^{-1} at about 20°N in contrast to the maximum value of about -1.3 m sec^{-1} found at 30°N at 800 mb (Fig. 28). The correlation between π and v thus not only insures $[\overline{\pi v_1}] + [\overline{\pi v_3}] = 0$, but also permits an effective mass-flux velocity different from the mean meridional velocities themselves.

V. THE SIMULATED AVERAGE MOISTURE AND PRECIPITATION

In addition to the fields of the primary variables of pressure, temperature, and wind, the distribution of the atmospheric water vapor and of its sources and sinks (evaporation and precipitation) is an important measure of the model's ability to simulate climate. In this section the global distributions of these variables as simulated for January in the control integration will be considered and compared with the available observations.

RELATIVE HUMIDITY AT 800 MB

The simulated January relative humidity at 800 mb is given in Fig. 31, along with the corresponding observed pattern. Here the simulated relative humidity was determined from the computed mixing ratio q_3 and the temperature T_3 at the level 3 as described in Gates et al. (1971), whereas the observed data are those given by Schutz and Gates (1971) based on the dew-point data of Crutcher and Meserve (1970) and Taljaard et al. (1969).

Only in a gross sense can the simulated field (Fig. 31a) be considered a satisfactory approximation to the observed humidity field (Fig. 31b). The prominent observed features are the dry regions over Africa, India, and Australia, and in the southwestern portions of North America, South America, and South Africa. The model has reproduced the low relative humidity over these areas with reasonable accuracy. The regions of higher humidity, however, are not well depicted in general, and there are many dissimilar features in the simulated and observed patterns. Particularly noticeable is the model's failure to simulate the regions of high humidity over South America, Africa, and Indonesia.

The errors of the simulated 800-mb relative humidity shown in Fig. 32 are generally largest in the tropics, where local errors of 40 percent are not uncommon. We note, moreover, that here the predominant error is negative; i.e., the simulation is drier than observation. Part of this error may be due to the model's use of a fictitious wind at $\sigma = 7/8$ to accomplish the horizontal moisture advection in (4), and part

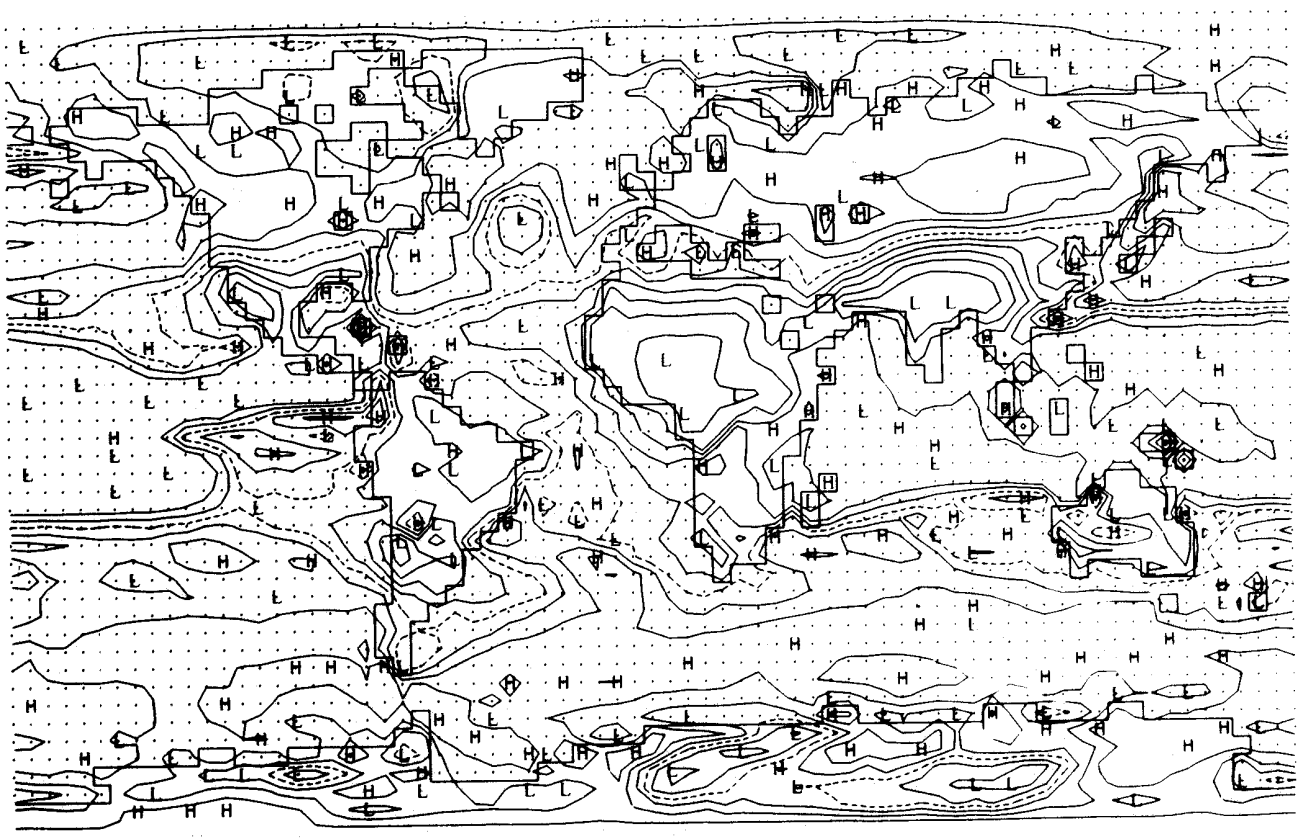

Fig. 31a -- The simulated relative humidity for January at 800 mb, with isolines at 10-percent intervals and the 60-percent isoline dashed.

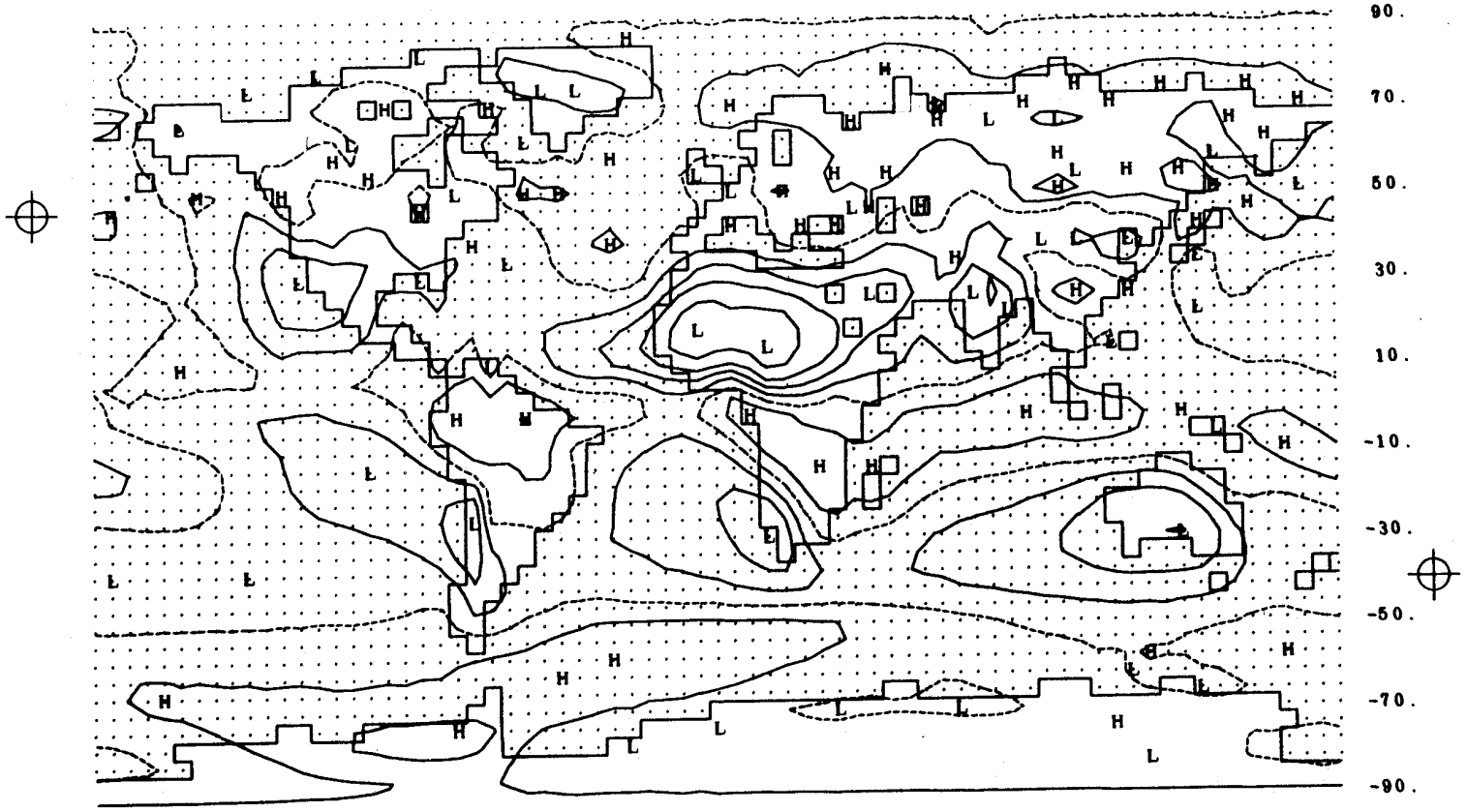

Fig. 31b -- The observed relative humidity for January at 800 mb, with isolines at 10-percent intervals and the 60-percent isoline dashed. From Schutz and Gates (1971), based on data of Crutcher and Meserve (1970) and Taljaard et al. (1969).

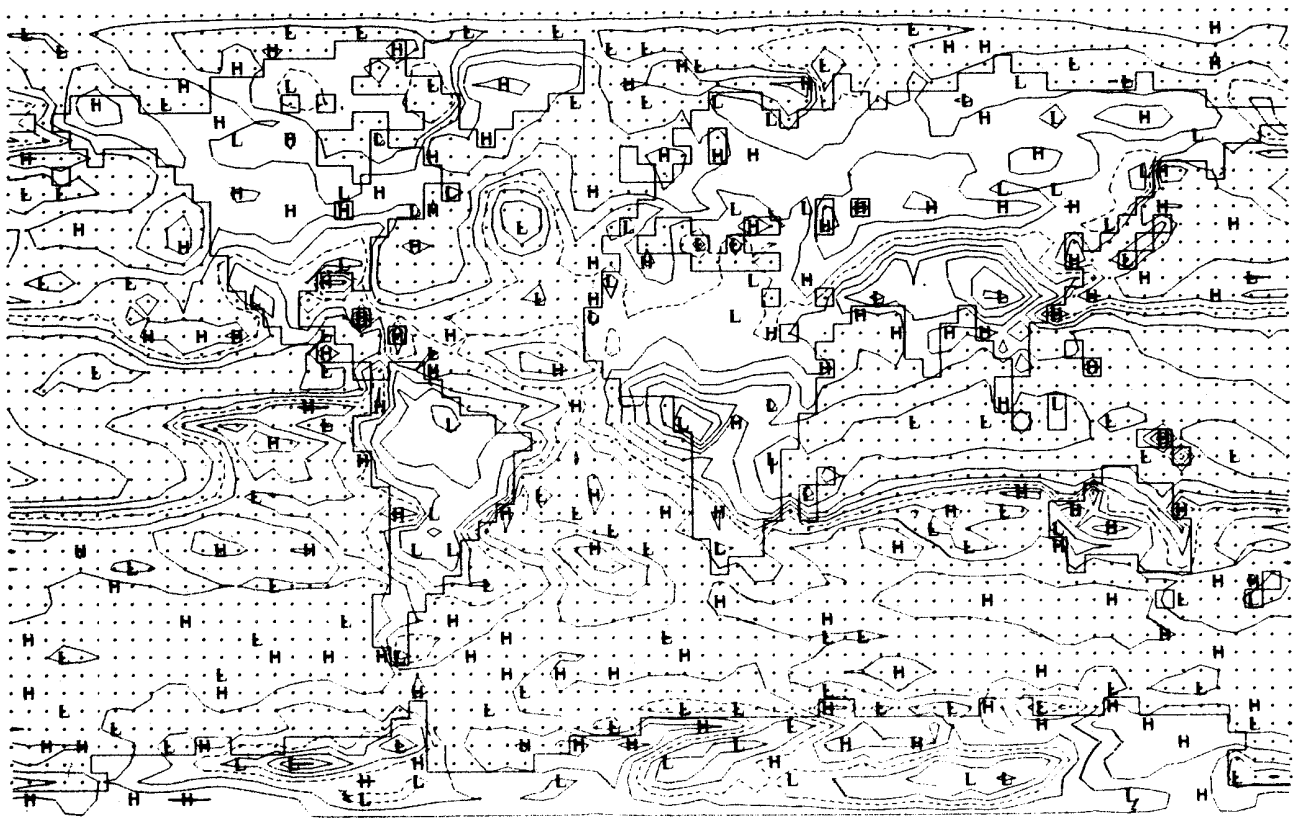

Fig. 32 -- The difference between the simulated and observed 800-mb relative humidity (Fig. 31a minus Fig. 31b). The isoline interval is 10 percent with the zero line dashed.

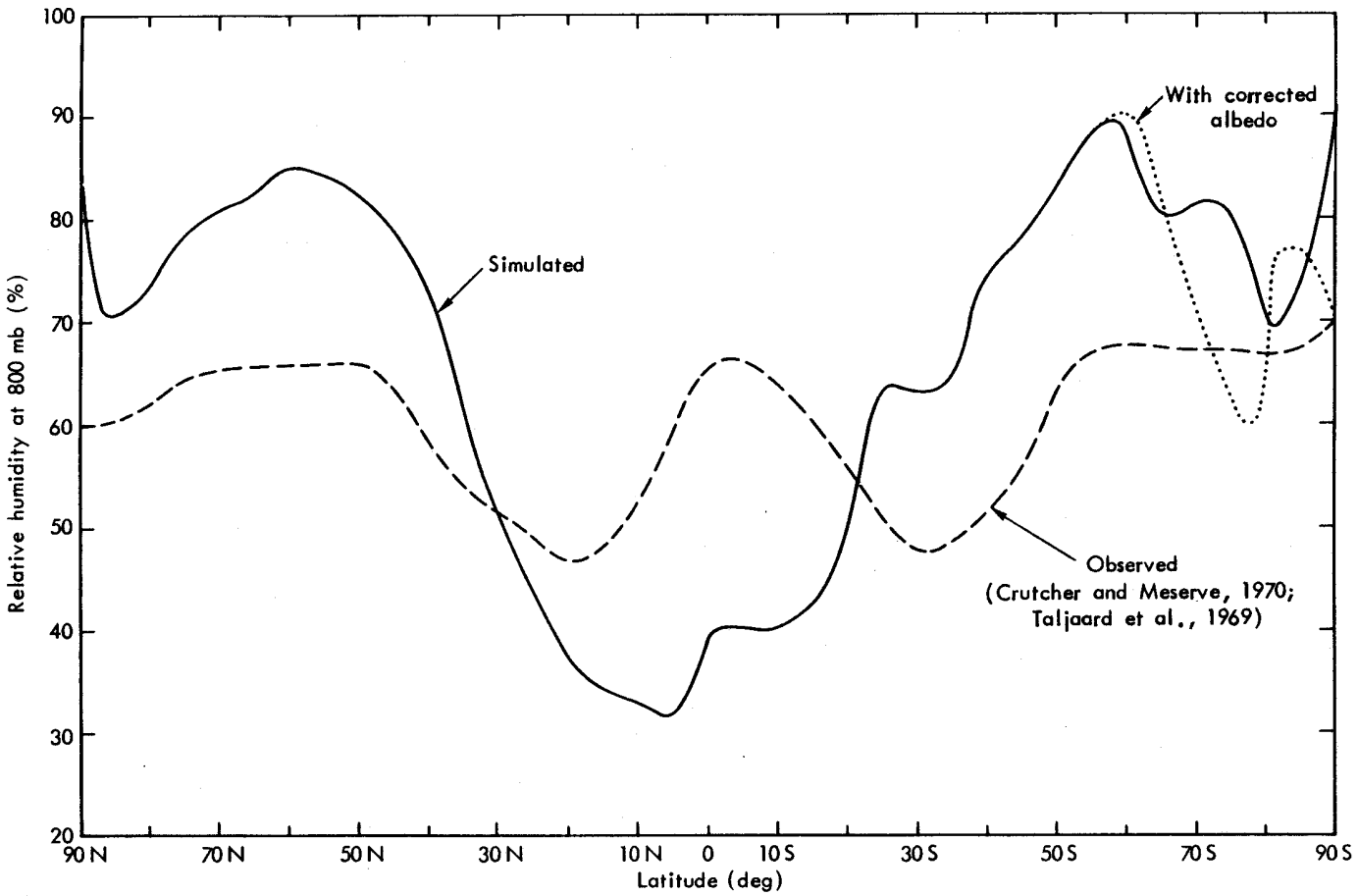

Fig. 33 -- The zonal average of the mean 800 mb relative humidity simulated for January (full line), with the corresponding observed distribution (dashed line), based on the data of Fig. 31.

may be due to the assumption of a completely dry atmosphere above the midlevel (approximately 600 mb), and the consequent absence of vertical moisture advection. Systematic errors in the simulated moisture-addition rate (E - C) may also contribute, as will be discussed below.

This low-latitude dryness is clearly seen in terms of the zonal averages given in Fig. 33. Poleward of about 30°N and 30°S, however, the simulation has substantially *over*estimated the relative humidity, resulting in the model's global average relative humidity of 59 percent approaching the observed value of 58 percent. This suggests that the model may be so efficient in the poleward advection of moisture that the higher latitudes are oversupplied while the tropics are depleted. As is discussed below, it is also possible that the model gives too little large-scale precipitation in the middle latitudes (and thereby does not deplete the midlatitude atmospheric moisture supply sufficiently), whereas it gives too much convective precipitation in the lower latitudes (and thereby overdepletes the tropical atmospheric moisture).

CLOUDINESS

Clouds in the Mintz-Arakawa two-level model are classified into three types, depending upon the particular condensation processes involved. Cloud type 1 (CL1 in the model) represents deep convective cloudiness at level 1 and is assumed to accompany either midlevel or penetrating convection (which, in turn, depends upon the vertical stability). A second form of convective cloud simulated is type 3 (CL3 in the model), which represents shallow convective cloudiness or cumulus at level 3. Both types of cloudiness are determined from the empirical formula

$$CL1,\ CL3 = -1.3 + 2.6\ RH_3 \tag{12}$$

where RH_3 is the relative humidity at level 3 (as in Fig. 31a), with the additional stipulation that $0 \leq (CL1,\ CL3) \leq 1$. These convective cloud forms occur only when the model's criteria for convective instability are met, after which there is an adjustment of both temperature and humidity to restore stability.

The third cloud form simulated is the large-scale cloudiness associated with nonconvective large-scale condensation. In the model this cloudiness (CL2) is set equal to 1 if large-scale precipitation is occurring, which itself depends on the apparent supersaturation at level 3 as a result of vertical motion. If large-scale precipitation (or condensation) is not occurring, then CL2 = 0. Thus, middle cloudiness is here simulated as either overcast or clear sky.

Each of the above cloud types affects the simulated absorption of both short- and long-wave radiation in the model atmosphere as described elsewhere (Gates et al., 1971). The fraction of the sky assumed to be cloud-covered is given by the expression CL = max (CL1, CL2, CL3), and it is this total cloudiness measure whose simulated global distribution is shown in Fig. 34. The observed January cloudiness shown in Fig. 35a is that given by Schutz and Gates (1971) for the northern hemisphere, as prepared from data furnished by the Environmental Technical Applications Center of the U.S. Air Force (1971).

In general, the January simulation has specified the maximum cloudiess over the North Pacific and North Atlantic oceans with reasonable accuracy. The model's possible ability to depict the relatively clear skies over the southwestern United States, over North Africa, and over eastern Asia is obscured by its apparent tendency to specify a low amount of cloudiness over nearly all continental areas. This same tendency is responsible for the simulation of relatively low cloudiness amounts over Europe, where there is substantial cloudiness observed (Fig. 35a).

These errors have resulted in differences between the simulated and observed cloudiness of as much as 4/10 over widespread areas, as shown in Fig. 35b. In terms of zonal averages, shown in Fig. 36, the model's mean cloudiness is systematically lower than the northern-hemisphere observations by approximately 2/10, although the cloudiness maximum is reproduced in about the correct midlatitude position. Also shown in Fig. 36 are the zonal averages of the TIROS satellite cloudiness observations of Miller (1970), here taken from the compilation of Schutz and Gates (1971). Even though the satellite data contain systematic errors due to the lack of discrimination between clouds and highly-reflective ground surfaces such as snow, ice, and desert, the model's

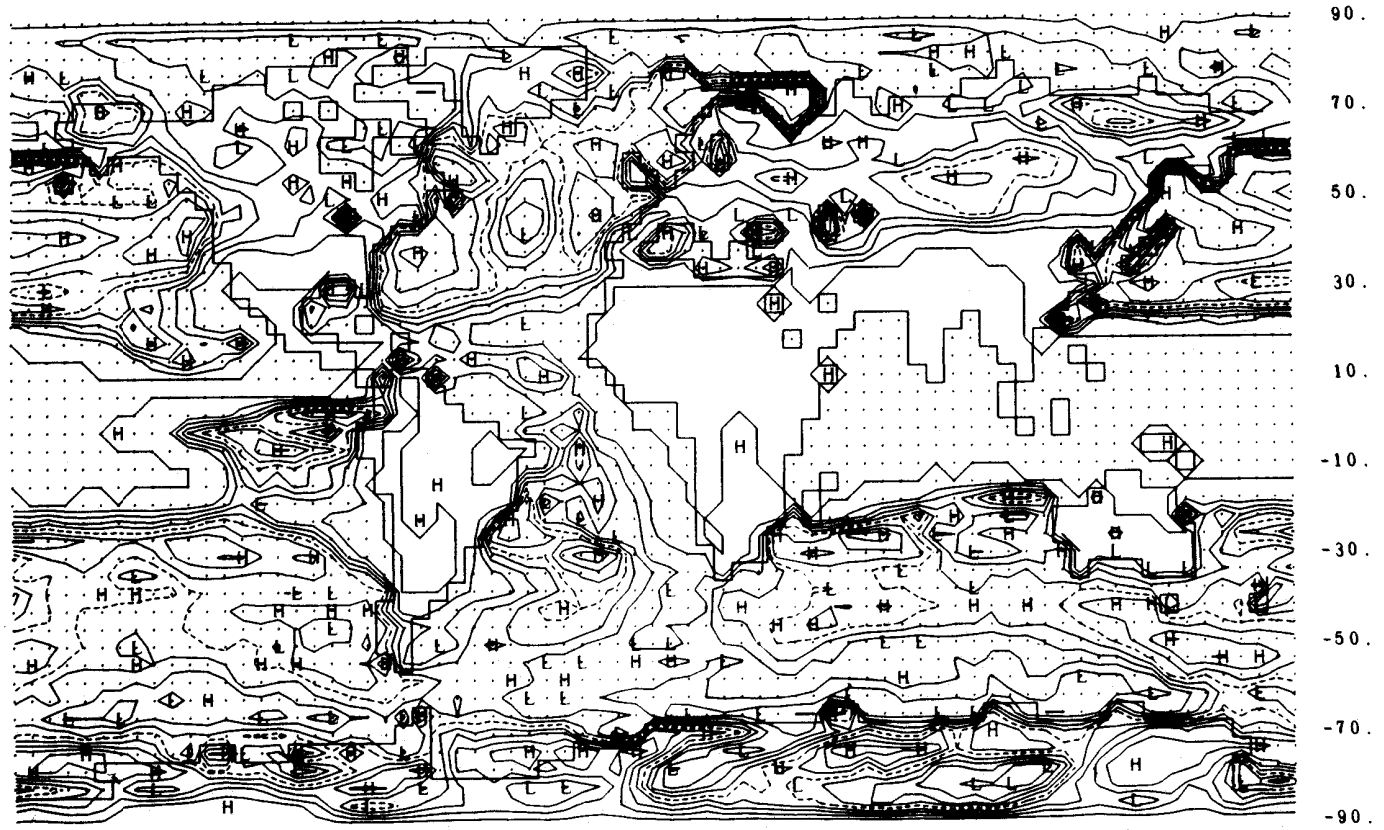

Fig. 34 -- The simulated total cloudiness for January, with isolines at 0.1-cloudiness intervals and the 0.5 isoline dashed.

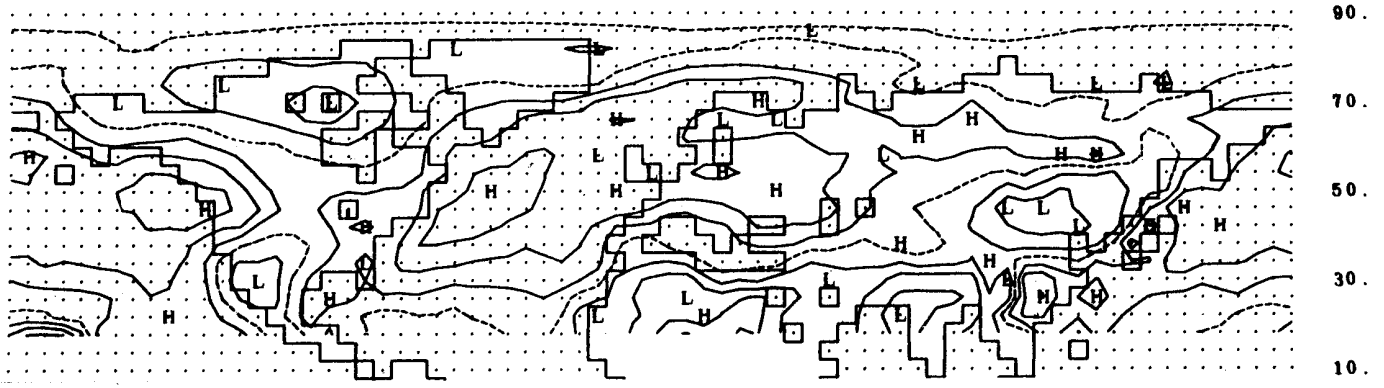

Fig. 35a -- The observed January cloudiness in the northern hemisphere, with isolines at 0.1-cloudiness intervals and the 0.5 isoline dashed. From Schutz and Gates (1971), as prepared from data supplied by the Environmental Technical Applications Center of the U.S. Air Force (1971).

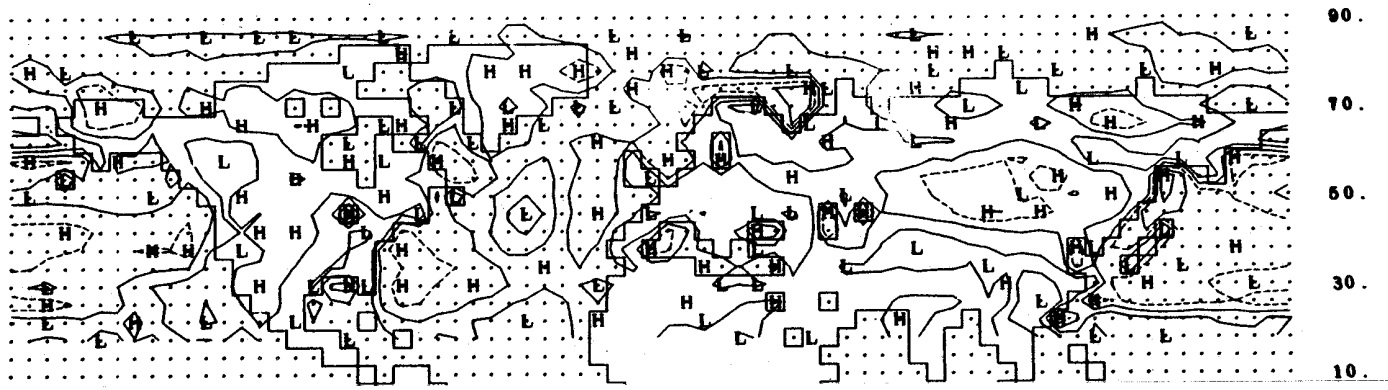

Fig. 35b -- The difference between the simulated and observed cloudiness (Fig. 34 minus Fig. 35a) in the northern hemisphere, with the isolines at 0.2-cloudiness intervals and the zero isoline dashed.

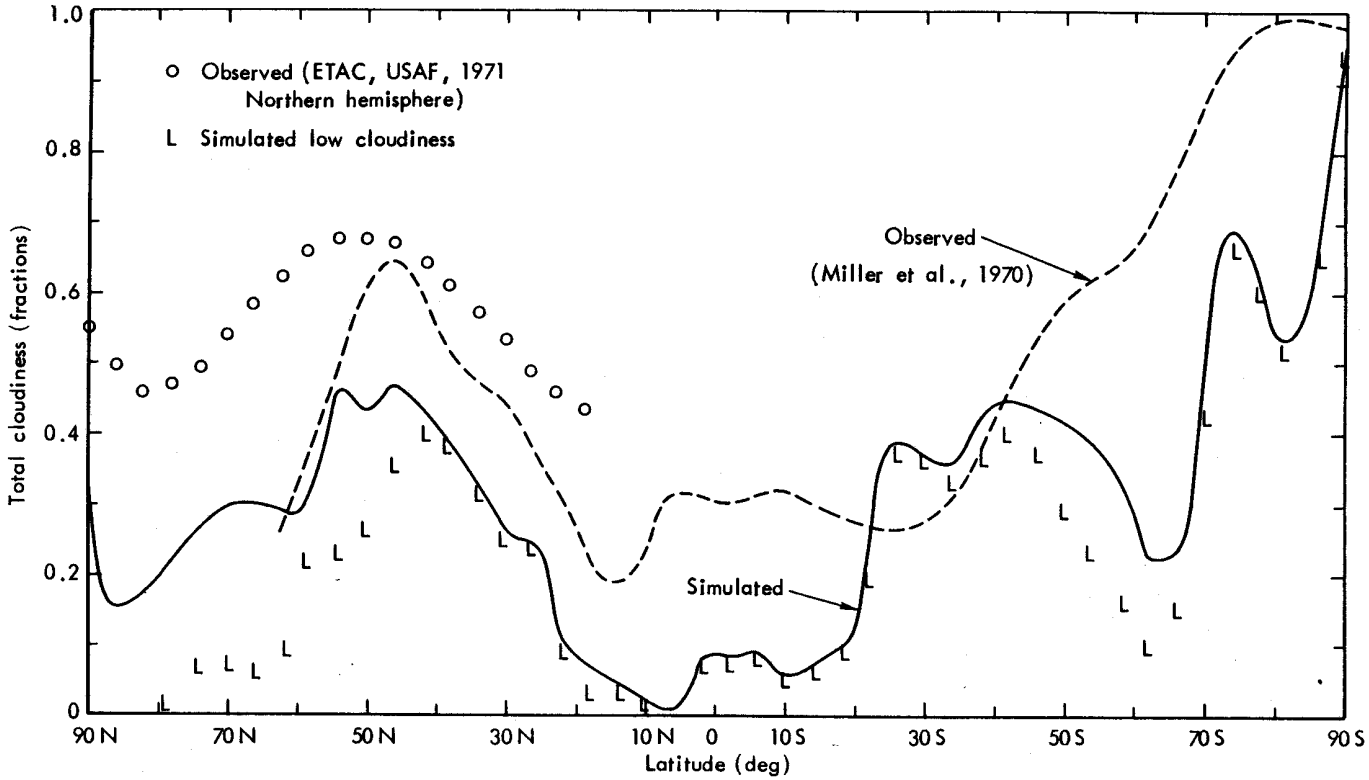

Fig. 36 -- The zonal average of the mean cloudiness as simulated for January (full line), together with the observed distribution (dashed line). From Schutz and Gates (1971), based on satellite data of Miller (1970). Also shown in the northern hemisphere (open circles) are the observed values (from both satellite and conventional observations) based on the data of Fig. 35. The symbol L denotes the simulated low cloudiness only.

January cloudiness is clearly too low, with a simulated global average of 0.26 compared to an observed value of 0.41 from Miller's data.

Most of the model's cloudiness is here due to the simulation of low clouds (type 3 or CL3 described above), which are associated primarily with convective heating over the oceans; the zonal average cloudiness due to this cloud type alone is also shown in Fig. 36. Only north of about 50°N does the cloudiness associated with large-scale precipitation contribute as much as 2/10 cloudiness to the zonal means. At no latitude does the simulated high cloudiness (CL1) give a zonal average greater than 5/10. This suggests that it may be desirable to increase systematically the total cloudiness simulated by the model at all latitudes, and in particular to increase the middle-level cloudiness whether or not it is associated with precipitation.

PRECIPITATION

The precipitation rate in the moisture-balance equation (4) is taken equal to the total rate of condensation due to both large-scale and convective processes. The precipitation associated with large-scale motions is given by the apparent supersaturation (due primarily to large-scale vertical motion), while the convective precipitation is equal to the condensation resulting from the parameterized midlevel and penetrating convection (due to vertical instability). The total precipitation rate simulated for January is shown in Fig. 37, together with the observed distribution for December, January, and February as given by Schutz and Gates (1972) from data of Möller (1951). Here the average simulated precipitation rate (Fig. 37a) was determined from the solutions every 1/2 hour (the minimum sampling interval possible),* rather than from the solutions every 6 hours. Sampling less frequently produces a distorted rainfall distribution in the tropics where convective precipitation is predominant (Gates, 1972).

A comparison of Figs. 37a and 37b shows that the model has simulated the arid regions southwest of the North American, South American,

*The simulated precipitation distribution (Fig. 37a) is from a separate integration (see Gates, 1972), rather than from the control integration used elsewhere in this report.

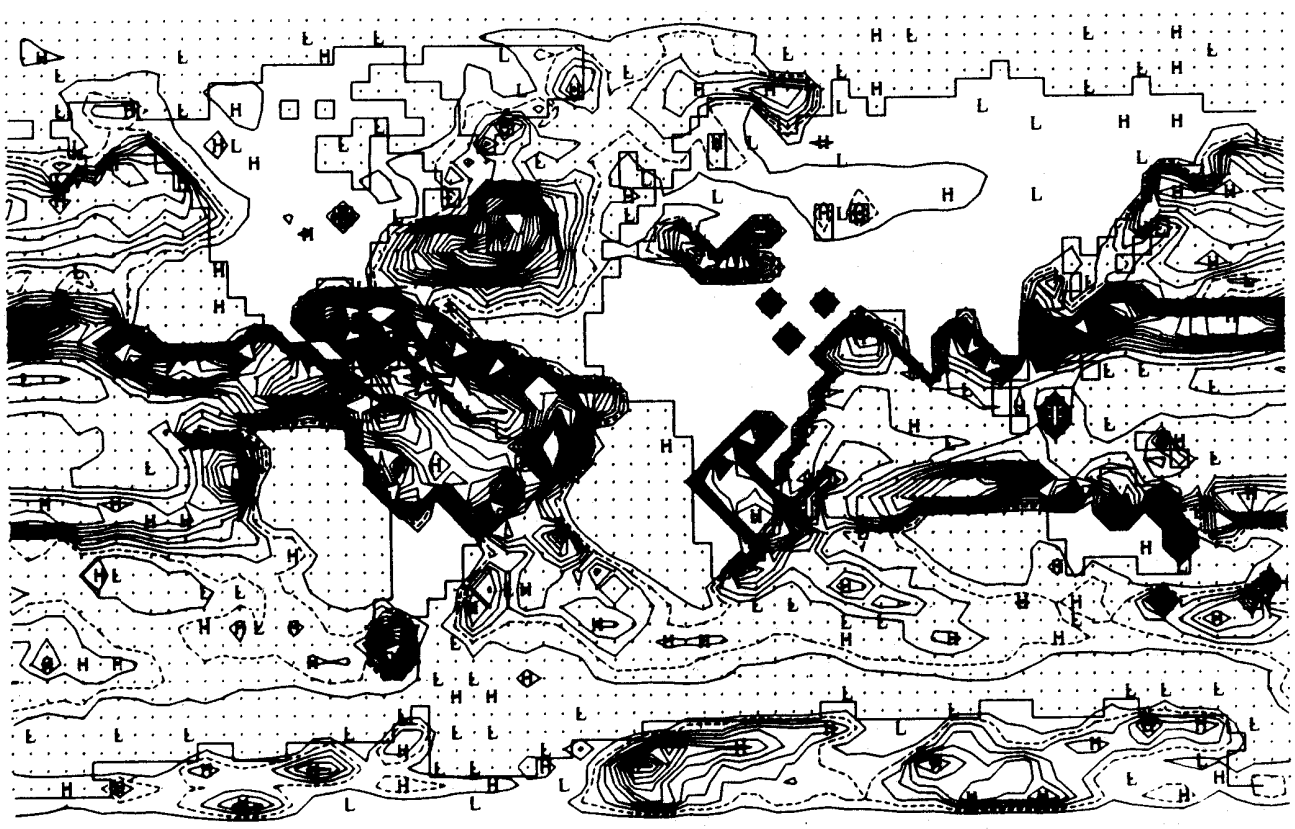

Fig. 37a -- The simulated precipitation rate for January (in a modified version of the control integration), with isolines at intervals of 1 mm day^{-1} and the 2 mm day^{-1} isoline dashed.

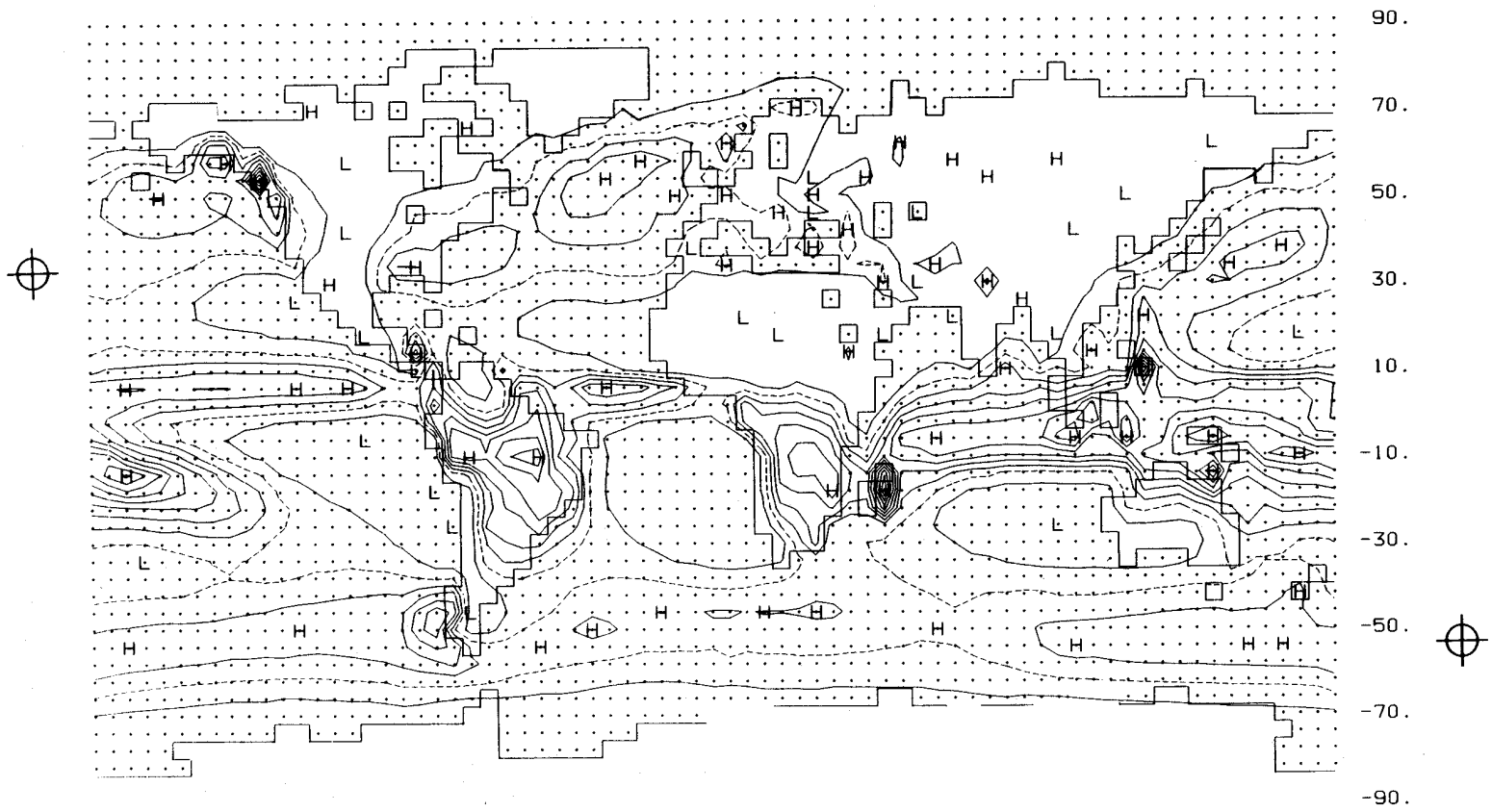

Fig. 37b -- The observed precipitation for December, January, and February, with isolines at intervals of 1 mm day^{-1} and the 2 mm day^{-1} isoline dashed. Based on data of Möller (1951) as summarized by Schutz and Gates (1972).

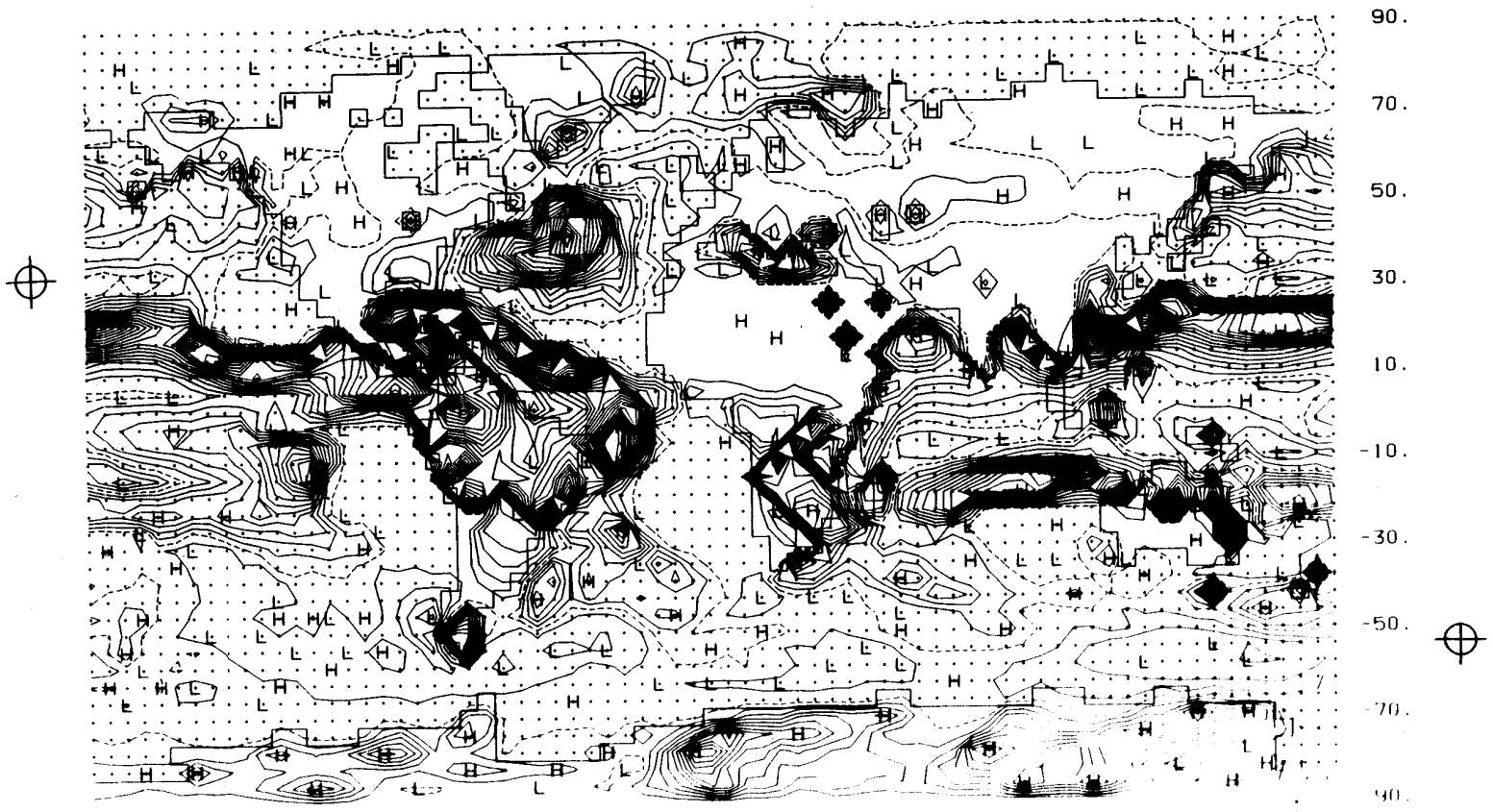

Fig. 38 -- The difference between the simulated and observed precipitation rate (Fig. 37a minus Fig. 37b). The isoline interval is 1 mm day^{-1} with the zero isoline dashed.

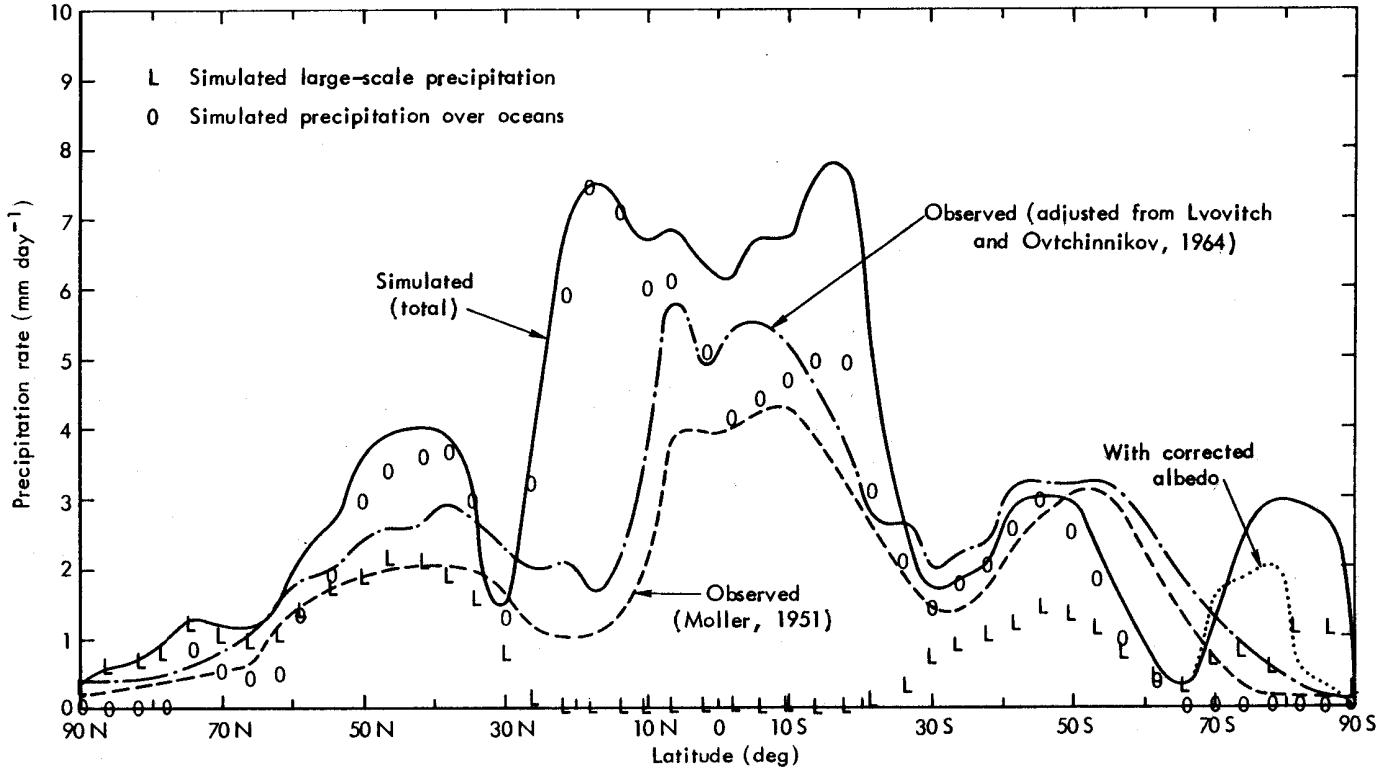

Fig. 39 -- The zonal average of the precipitation rate as simulated for January (full line) and as observed (dashed line), based on the data of Fig. 37. The dash-dotted line gives the observed precipitation from the data of Lvovitch and Ovtchinnikov (1964) as modified by Schutz and Gates (1971) for December, January, and February. The symbol L denotes the zonal averages of the simulated large-scale precipitation rate only, and the open circles denote that portion of the total simulated precipitation that falls over the oceans.

African, and Australian continents with reasonable fidelity. The most serious errors occur in the specification of the areas of maximum precipitation over the North Atlantic (where the simulated average precipitation rate of 15 mm day^{-1} is several times that observed), and in the tropics (where the simulated rainfall rate is generally about twice that observed and displaced poleward). We may also note the near absence of simulated precipitation over the bare land areas (with the notable exceptions of South America and Africa). This feature results in a poor representation of the observed precipitation over eastern North America, Europe, and (especially) over Southeast Asia. Although there is some uncertainty in Möller's (1951) observed precipitation distribution, the global rainfall given by Lvovitch and Ovtchinnikov (1964) (see Schutz and Gates, 1971) shows a similar general distribution. The precipitation simulation errors shown in Fig. 38 may, therefore, be considered representative of the model.

In the zonal averages shown in Fig. 39, the prominent error is again the model's excessive precipitation between approximately 25°N and 25°S. The bulk of this precipitation falls on the oceans, with a maximum at 18°N and the subtropical dry zone in the northern (winter) hemisphere displaced some 15 deg northward of its observed position. The simulated higher-latitude precipitation is also too great (in the northern hemisphere), although the maximum is correctly positioned at about 40°N. This error is also partly due to the simulation of excessive convection, as large-scale and convective condensation contribute approximately equally to the total precipitation poleward of 30°N (see Fig. 39). [The separate global patterns of the convective and large-scale precipitation simulated in this experiment have been given by Gates (1972).] Only in the southern hemisphere between 50°S and 65°S is the precipitation significantly underestimated by the model, although here the observations themselves may be less reliable.

Another interesting feature of Figs. 37 and 39 is the relatively heavy precipitation simulated over Antarctica. In contrast to the generally stable and dry atmosphere observed between 70°S and 90°S, the model produced appreciable deep convection in this region. This is another result of the inadvertent surface-albedo error previously noted.

On a global average, the simulated total precipitation rate of 4.1 mm day^{-1} (of which 3.5 mm day^{-1} is convective) is some 86 percent higher than the observed rate of 2.2 mm day^{-1} from Möller's data in Fig. 39. As is noted earlier, nearly all of this error is due to the excessive convective precipitation simulated in the tropics. The excessive latent heat released by this parameterized convection may also contribute to the model's specification of too high a temperature at 400 mb previously cited (see Fig. 21), as well as to the low tropical relative humidity and cloudiness (see Figs. 33 and 36).

EVAPORATION

The evaporation rate, E, in the moisture-continuity equation (4) is determined from the expression

$$E = \rho_4 C_D W(q_g - q_4)\rho_w^{-1} \tag{13}$$

where ρ_4 is the surface (level 4) air density, W is a measure of the surface wind speed, ρ_w is the density of water, C_D is the surface drag coefficient (itself dependent upon the surface wind speed), and q_g and q_4 are the mixing ratios at the ground and in the surface air (just above the ground). Over the oceans q_g is taken as the saturation value appropriate to the assigned sea-surface temperature (see Fig. 3), while over land (and ice) surfaces q_g is determined from the local moisture and heat balance. Over all surfaces, q_4 is principally determined by the moisture at level 3 (q_3), although it too is affected by the surface heat and moisture balances. For details of these processes, the reader is referred to Gates et al. (1971).

The average evaporation rate simulated for January is shown in Fig. 40, together with the observed distribution from Schutz and Gates (1971) based on data of Budyko (1963). We see at once that the overall pattern of the observed evaporation rate is simulated reasonably well by the model, although the rate is overestimated by as much as 100 percent in the tropical latitudes. Largely through the controlling influence of the sea-surface temperature, the model has simulated the zone of lower evaporation near the equator in the Indian and Pacific

oceans, but has even here overestimated the rate in absolute terms. Over land, relatively little evaporation is simulated except where the groundwater level is kept high by heavy rainfall. In the model this occurs in January only over the southern Amazon Basin, over south-central Africa, and in some coastal regions. In the difference map shown as Fig. 41, the largest simulation errors are found off the east coast of the United States and off the west coast of Central America. Here the computed average evaporation rates are several times those observed, with the error occasionally exceeding 10 mm day^{-1}.

This apparent tendency of the model to overpredict the evaporation is perhaps more clearly seen in the zonal averages shown in Fig. 42. Between about 30°N and 30°S the general pattern of the simulated evaporation is similar to that observed, but the computed rates are approximately 50 percent greater than the observed ones. Although no observations are available south of 60°S, the high rate of evaporation simulated over Antarctica may be attributed to the surface albedo error discussed earlier.

Averaged globally, the simulated January evaporation rate of 4.0 mm day^{-1} is consistent with the simulated global average precipitation rate of 4.1 mm day^{-1} (Figs. 37 and 39). Both rates, however, substantially exceed the observed global average rates of evaporation and precipitation (3.1 mm day^{-1} and 2.2 mm day^{-1}). The model's overprediction of the precipitation is therefore passed on in the form of excessive (and approximately equal) evaporation. It is apparent, however, that the "observed" long-term average global rates of evaporation and precipitation do not balance as well as do the simulated ones. It would appear that the mean December, January, February global precipitation is seriously underestimated by Möller (1951), or that the evaporation is systematically overestimated in the data of Budyko (1963), or both. Since the data of Lvovitch and Ovtchinnikov (1964), as summarized by Schutz and Gates (1971), give a global mean precipitation rate of 2.9 mm day^{-1}, the greater observational error would seem to lie in Möller's data.

The details of the model's simulation of the net rate of moisture addition, E - C, are given elsewhere (Gates, 1972). Here we note,

however, that this simulated difference is positive only between 20° and 40° latitude in each hemisphere, which agrees reasonably well with the observed average moisture source for January from Figs. 39 and 42.

GROUND WETNESS

To complete this presentation of the model's hydrologic cycle, the mean simulated January ground wetness is shown in Fig. 43. As described in detail elsewhere (Gates et al., 1971), the ground wetness is a dimensionless measure of the surface wetness, scaled from 0 to 1. Over water, snow, and ice, it is taken as unity, whereas over land it is calculated from the surface water balance. When the (local) precipitation exceeds evaporation, the ground wetness is increased toward unity, with a portion of the excess water assumed lost in surface runoff. When evaporation exceeds precipitation, the local ground wetness is decreased (without runoff).

Although there are no observations of average ground wetness readily available, the areas of dry land surface in the simulated January ground wetness shown in Fig. 43 correspond roughly with the locations of the world's deserts. The most notable exceptions are central Africa, India, and Indochina, over which there is little simulated rainfall (Fig. 37a). The ground wetness itself is used in the calculation of the ground temperature and the evaporation, and the dry areas in Fig. 43 are all regions of low simulated evaporation (Fig. 40a). The only areas of extensive wet ground and appreciable runoff are in the Amazon Basin, in southeast Africa, and in Indonesia, which correspond well with the regions of high precipitation observed in January as shown in Fig. 37b.

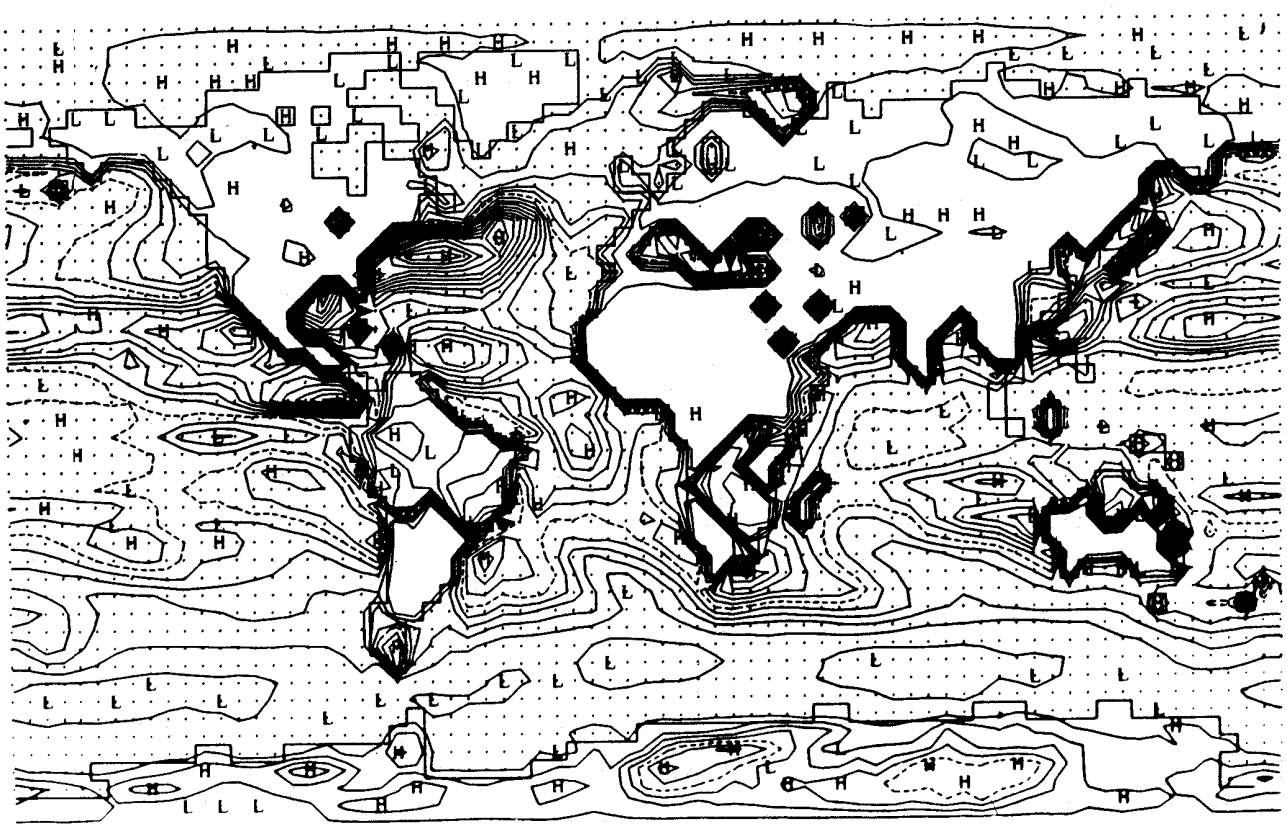

Fig. 40a -- The simulated evaporation rate for January, with isolines at intervals of 1 mm day^{-1} and the 5 mm day^{-1} isoline dashed.

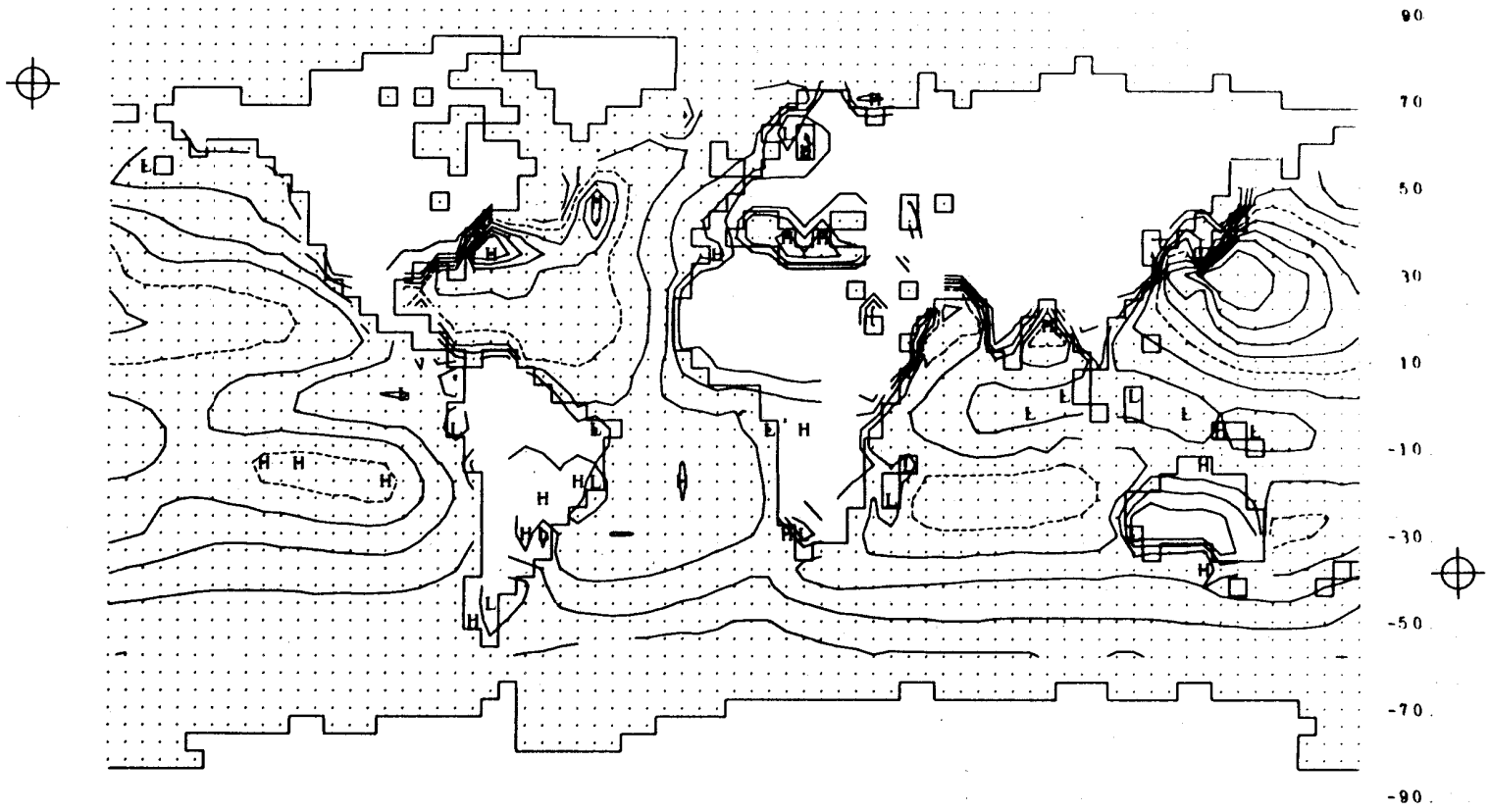

Fig. 40b -- The observed evaporation rate for January, with isolines at intervals of 1 mm day^{-1} and the 5 mm day^{-1} isoline dashed. The blank regions are areas for which observational data are missing. Based on data of Budyko (1963) as given by Schutz and Gates (1971).

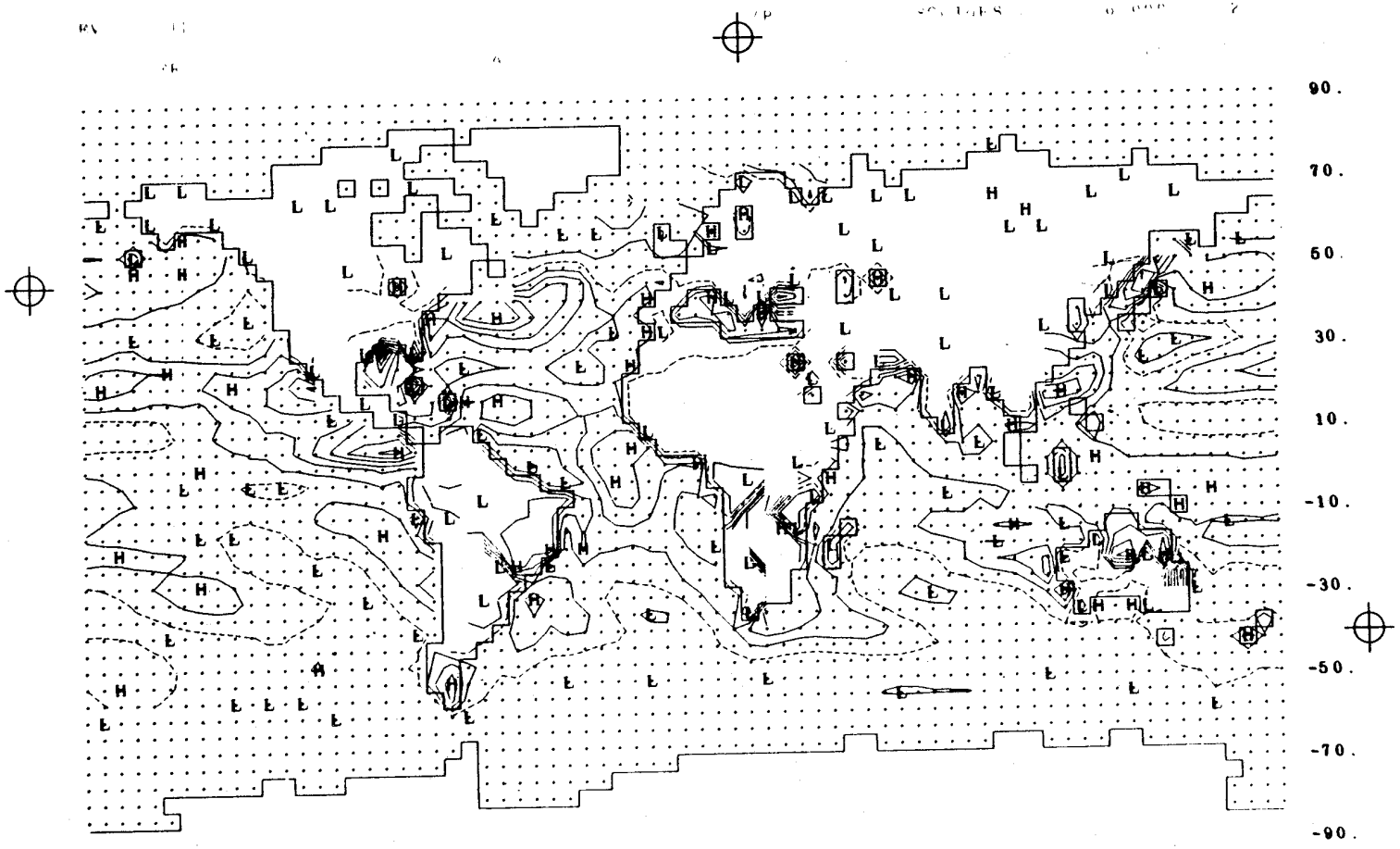

Fig. 41 -- The difference between the simulated and observed evaporation rate (Fig. 40a minus Fig. 40b). The isoline interval is 1 mm day^{-1} with the zero isoline dashed.

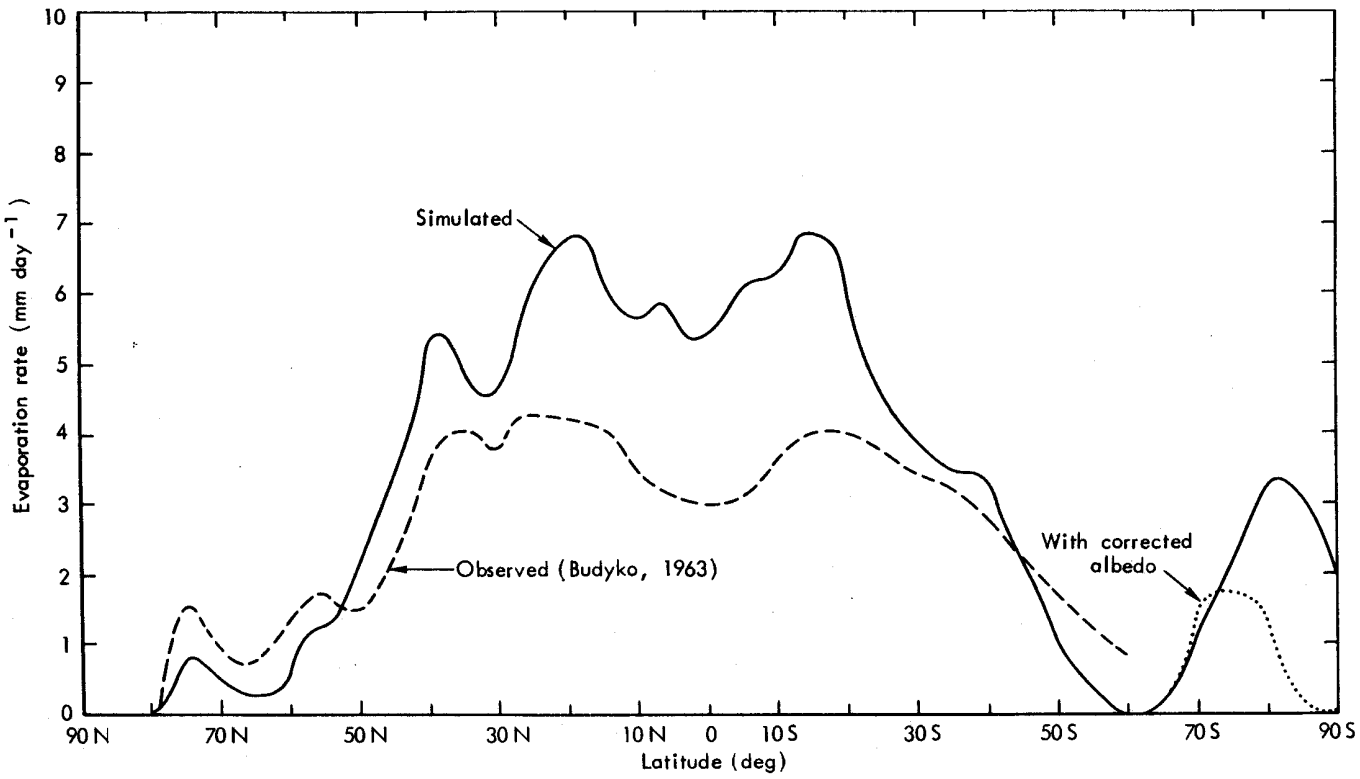

Fig. 42 -- The zonal average of the evaporation rate as simulated for January (full line) and as observed (dashed line), based on the data of Fig. 40.

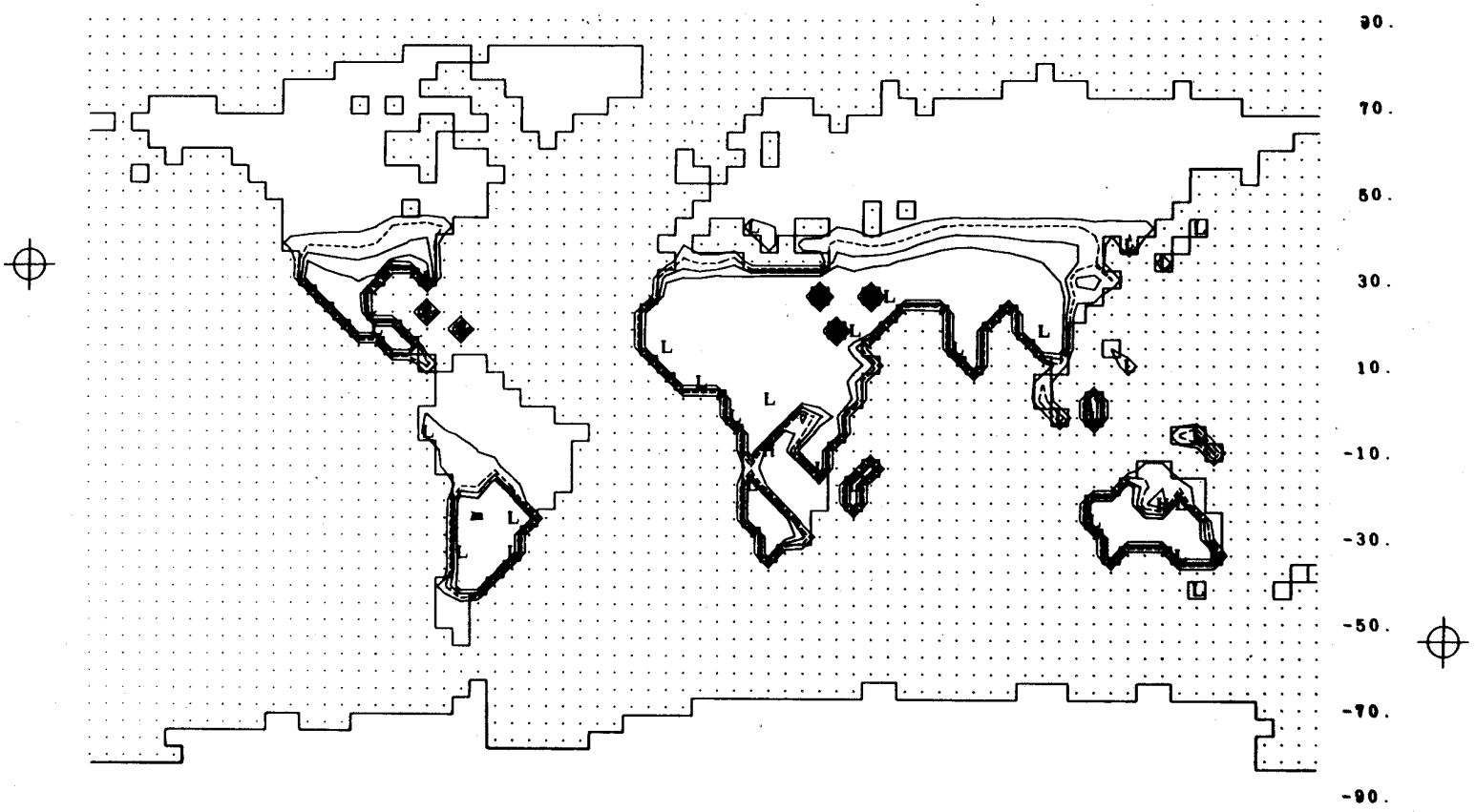

Fig. 43 -- The simulated ground wetness in January, with isolines every 0.2 and the 0.6 isoline dashed. The oceans and all ice-covered surfaces are considered completely wet (ground wetness ≡ 1).

VI. THE SIMULATED AVERAGE SURFACE HEATING

Of the many processes which contribute to the net heating rate, $\dot{H}$, in the model, only a few can be readily compared at present with corresponding observed global distributions. Here we shall consider only the flux of sensible heat and the net surface absorption of shortwave radiation, both of which are components of the surface heat balance. The heating at tropospheric levels 1 and 3 in the model, however, is dominated by the latent heat released during the simulated condensation (or precipitation). This process accounts for some 70 percent of the heating (as opposed to cooling in the model), and its global distribution may be obtained from the precipitation rates of Fig. 37 by conversion to the equivalent latent heating rate. The other heating processes important in the model's tropospheric heat budget are the net absorption of solar insolation and the net flux of longwave radiation. Lacking appropriate global observations of these processes, a comparison of the simulated zonal averages with the available observed zonal averages has been given elsewhere (Gates, 1972). A more comprehensive analysis of the model's simulated radiation budget is in preparation (Kahle, 1972).

SURFACE SENSIBLE-HEAT FLUX

The upward (turbulent) flux of sensible heat at the surface is given by the expression

$$\Gamma = \rho_4 C_D c_p W(T_g - T_4) \tag{14}$$

where T_g is the ground surface temperature, T_4 is the air temperature just above the ground, and ρ_4, C_D, and W are as in (13). Over the oceans T_g is the assigned sea-surface temperature (see Fig. 2), whereas over land it is computed from an assumed condition of zero net heat flux. The surface air temperature T_4 resembles the model's free air temperature extrapolated to the surface but is also affected by the simulated low-level convective heat transport. The sensible heating

given by (14) is assumed to represent a flux from the surface to the model's lower level (level 3), where it serves to change the free-air temperature, T_3, as a part of the diabatic heating, H_3, in (3).

The simulated surface sensible-heat flux for January is shown in Fig. 44, along with the observed pattern as given by Schutz and Gates (1971) based on data of Budyko (1963). The prominent features of the simulation (Fig. 44a) are the maxima of upward heat flux off the east coasts of North America and Asia, where there is a characteristic flow of relatively cold air from the continents over the warmer oceans. While these features are realistic in both pattern and position, they are approximately twice as intense as the fluxes derived from the observed data (Fig. 44b).

A second noteworthy feature of the simulated sensible surface heating is the calculation of a *negative* flux over much of the tropical oceans, with values as large as 200 ly day^{-1} off the central west coasts of Africa and South America. According to Budyko's (1963) data as shown in Fig. 44b, the observed heat flux is here small but positive. The overall pattern of the simulated sensible-heat flux over the oceans (Fig. 44a) bears a marked resemblance to the simulated cloudiness (Fig. 34); both fields are dominated by low-level convection over the sea. Over the central and southern parts of South America and Africa, as well as over Australia, the model has successfully simulated upward heat fluxes, but here again the maxima are approximately twice those observed over these continents in the southern summer.

The errors of the simulation of sensible-heat flux are shown more clearly in Fig. 45, where local differences of more than 100 ly day^{-1} are not uncommon. In Fig. 46, the simulated flux is seen to average about 50 ly day^{-1} too low between about 20°N and 20°S, and is more than 100 ly day^{-1} below that observed in high northern latitudes. In contrast to the observed zonal average heat flux which is everywhere positive, the model yields a downward heat flux (from the air to the ground) in both low and high latitudes. The average downward (negative) fluxes simulated at latitudes north of about 50°N are probably due to the model's calculation of low surface temperatures over the continents, whereas Budyko's data in this region are almost entirely over the

oceans (see Fig. 44b). If we compare the simulated surface heat flux as zonally averaged only over the oceans (shown by the open circles in Fig. 46), we find at least agreement in sign with Budyko's data at latitudes north of 50°N.

It appears that the low (and even negative) zonally averaged sensible-heat flux simulated between about 20°N and 20°S (Fig. 46) is due to the model's systematic overprediction of the surface air temperature over the tropical oceans. A comparison of Figs. 3 and 13 shows that the simulated surface air temperature not only is generally higher than that observed but is several degrees higher than the prescribed sea-surface temperature itself over all tropical oceans between about 20°N and 20°S. This has resulted through (14) in the reversal of the normal (observed) upward sensible-heat flux in this region, as shown by the oceanic zonal averages (open circles) in Fig. 46. The use of more realistic sea-surface temperatures and a more detailed treatment of the surface layer in the model could be expected to reduce these discrepancies.

SURFACE SHORTWAVE RADIATION

Depending on wave length, the shortwave (solar) radiation incident at the top of the model atmosphere is either subject to atmospheric absorption or subject to scattering, both by the air and by clouds. Both components of the radiation are also partially reflected at the earth's surface, depending upon the locally prescribed albedo, with the remainder being absorbed at the surface. The global distribution of the solar radiation incident at the surface, as simulated in the model for January, is shown in Fig. 47a. The observed distribution of the solar radiation received at the surface in January is shown in Fig. 47b, based on the data of Budyko (1963) as summarized by Schutz and Gates (1971).

Both the observed and simulated surface solar radiation show maxima over the southern hemisphere oceans, as expected for January, with a more-or-less uniform northward decrease. In general, however, the simulated surface solar radiation (Fig. 47a) is somewhat greater than the observed incident radiation (Fig. 47b), as may be more clearly seen

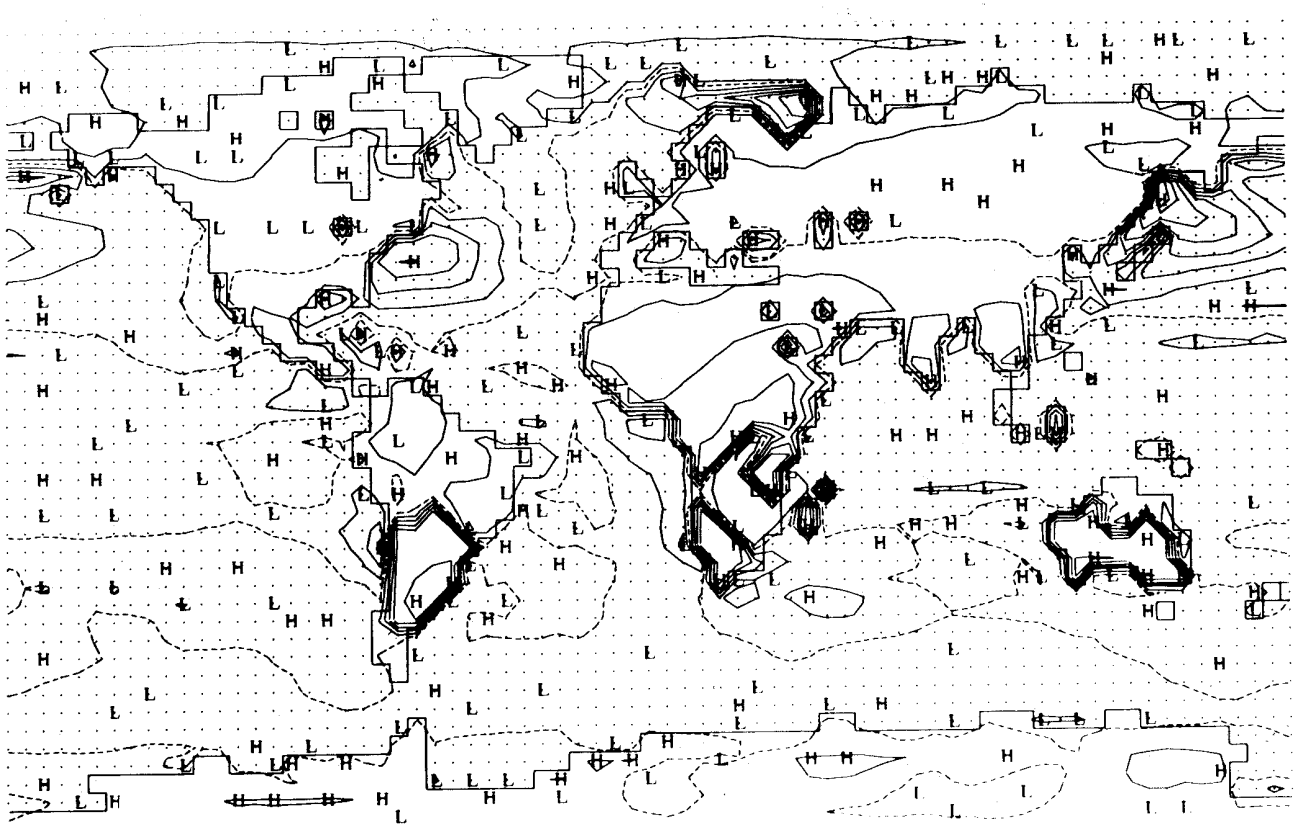

Fig. 44a -- The simulated sensible heat flux at the surface for January, with isolines at intervals of 100 ly day^{-1} and the zero isoline dashed.

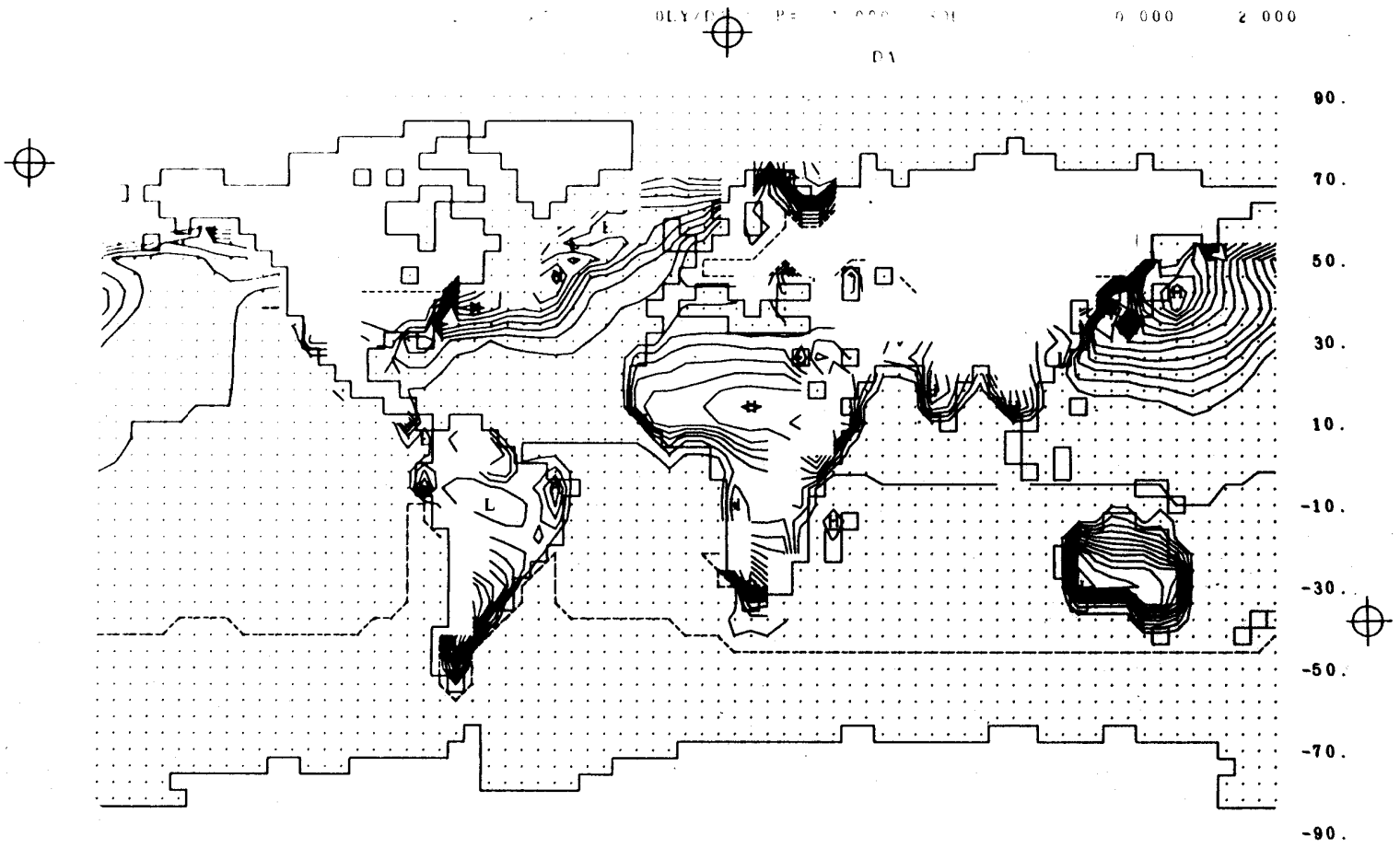

Fig. 44b -- The observed sensible heat flux at the surface for January, with isolines at 20 ly day^{-1} intervals and the zero isoline dashed. The blank regions are areas for which observational data are missing. From Schutz and Gates (1971), based on data of Budyko (1963).

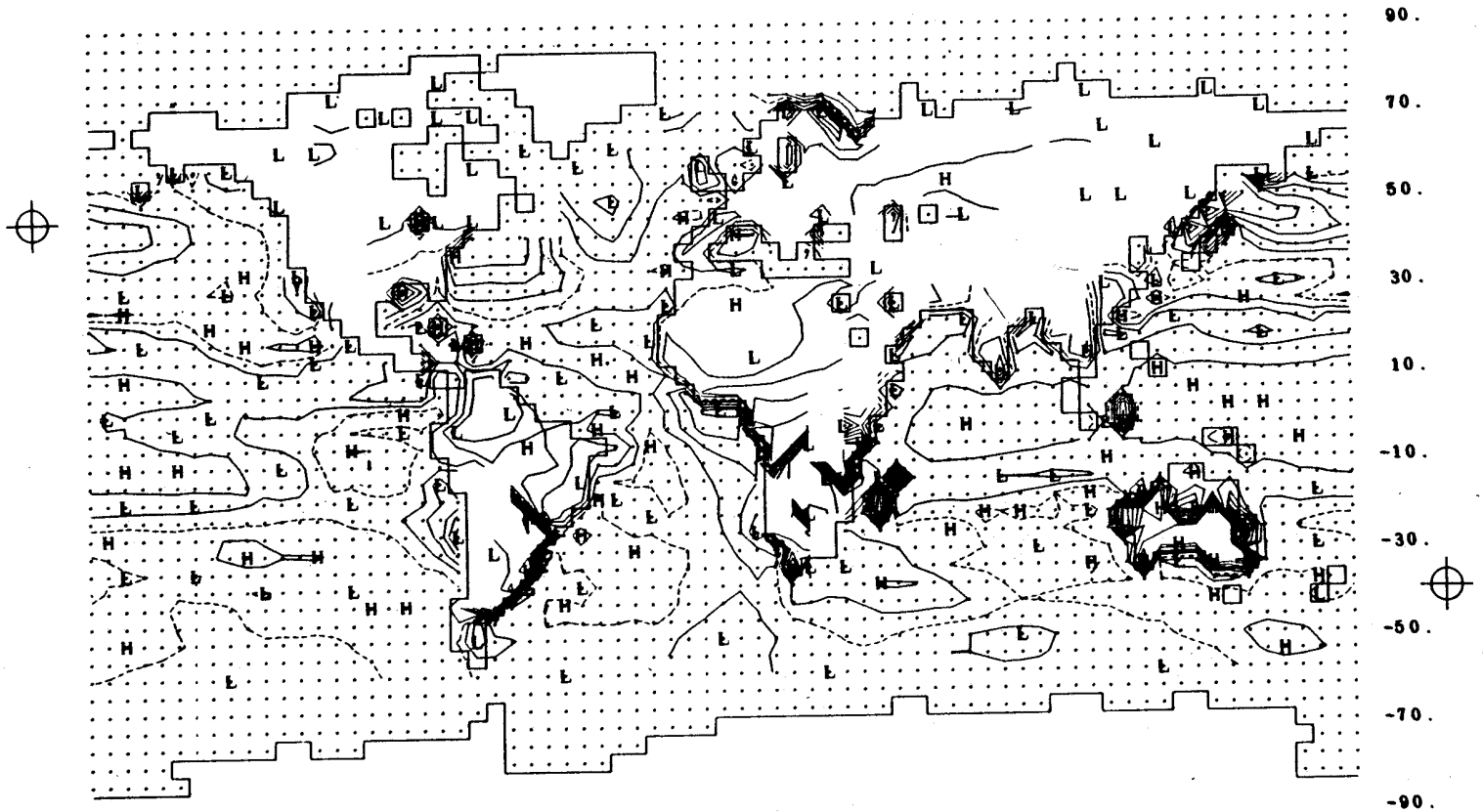

Fig. 45 -- The difference between the simulated and observed surface sensible heat flux (Fig. 44a minus Fig. 44b). The isoline interval is 60 ly day^{-1}, with the zero isoline dashed.

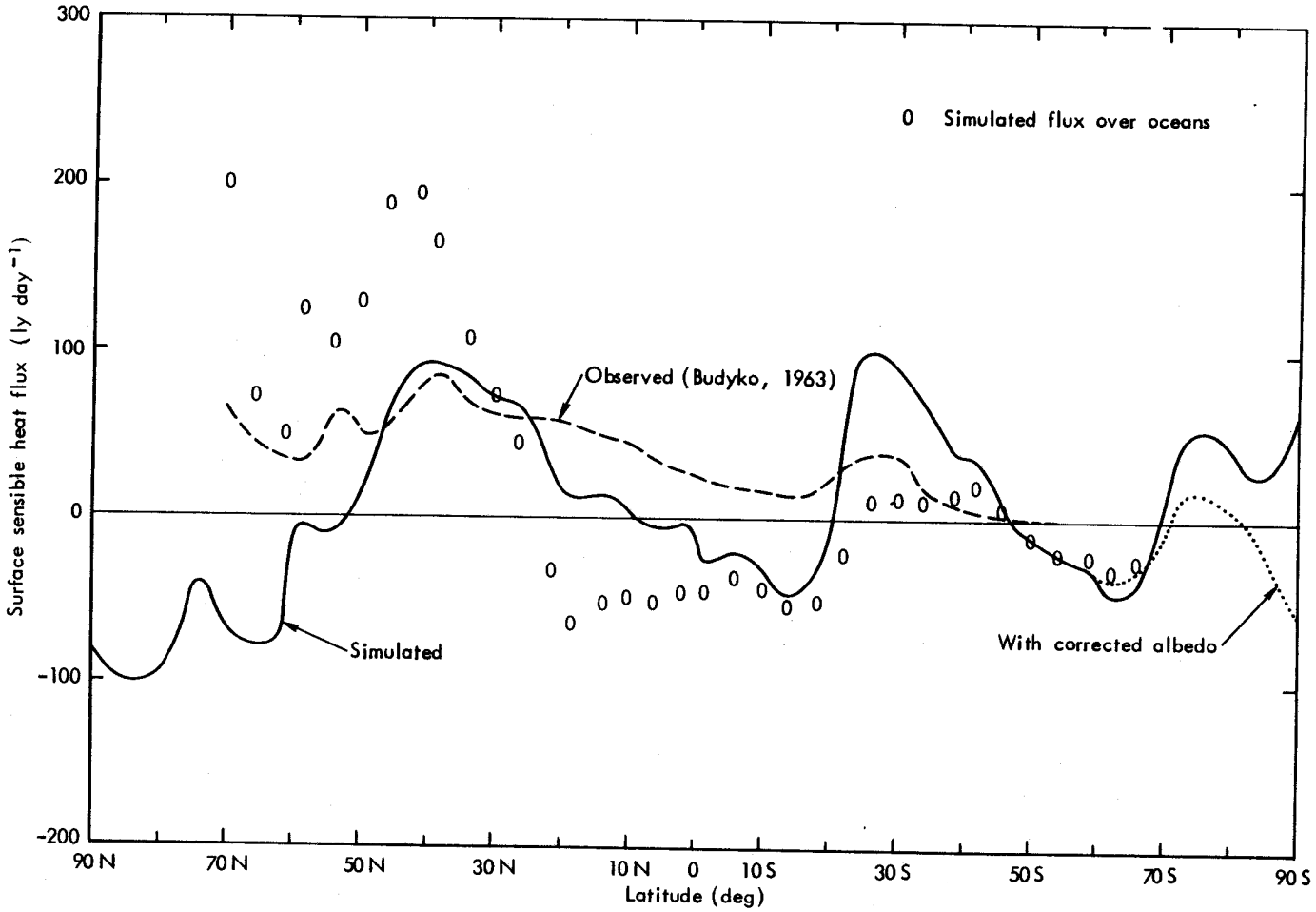

Fig. 46 -- The zonal average of the surface sensible heat flux as simulated for January (full line) and as observed (dashed line) according to the data of Fig. 44. The open circles denote the zonal average over the oceans only.

in the difference, or simulation error, in Fig. 48. On the basis of the zonal averages shown in Fig. 49, this oversimulation of the shortwave, or solar, radiation incident at the surface amounts to some 134 ly day^{-1} in the global mean. Since the global average observed (between 70°N and 62°S) is 377 ly day^{-1}, this error is a substantial fraction of the solar radiation budget. The solar radiation absorbed at the surface may be found from the simulated incident radiation data in Figs. 47a and 48 by multiplying by $(1 - \alpha)$, where α is the surface albedo (0.07 over ocean, 0.14 over land, and varying with latitude from about 0.4 to 0.9 over ice; see, however, the footnote on p. 8).

This evidence suggests that the model permits too much shortwave radiation to penetrate to the surface by the simulation of too little absorption or reflection in the troposphere. Although the model's simulated radiation budget is not analyzed in detail here, the analysis of a closely related experiment has shown that the total shortwave radiation absorbed in the atmospheric column is reasonably accurate (Gates, 1972). Since this same analysis also showed that the simulated net longwave cooling of the (tropospheric) column was reasonably close to observation, we are led to speculate that the model significantly underestimates the shortwave radiation reflected to space by *clouds*. The simulated total cloudiness was shown earlier (Figs. 34 to 36) to be systematically too low by about 0.2 coverage. Noting that this error is half the observed global average cloudiness of 0.4, the model's clouds thus reflect on the average only about half as much solar radiation to space as do the observed clouds. Since reflection by clouds is an important part of the atmosphere's shortwave radiation budget, an increase in the model's cloudiness by about a factor of two could therefore be expected to substantially reduce the surface shortwave radiation error.

SURFACE HEAT BALANCE

Letting the solar radiation absorbed at the surface be denoted by S_g, and the net longwave radiation emitted from the surface by R_4, the net surface heating or heat balance is given by the expression

$$S_g - R_4 - \Gamma - L\rho_w E \qquad (15)$$

where Γ is the surface sensible-heat flux as in (14), E is the evaporation rate as in (13), and L is the latent heat of condensation. Over land areas in the model it is assumed that (15) is equal to zero, i.e., that there is no net heating at the ground surface. The resulting equation is in fact used to determine the unknown ground temperature, T_g, upon which R_4 and Γ depend. Over the oceans, on the other hand, no such balance is assumed and the water's surface temperature is prescribed (as in Fig. 3).

The simulated surface heating (15) for January is shown in Fig. 50, along with the observed distribution given by Budyko (1963), as summarized by Schutz and Gates (1971). The principal areas of observed net surface heating in the western North Atlantic and western North Pacific oceans are reasonably well simulated by the model, as are the regions of net heat loss in the lower latitudes. Over the southern oceans (say south of 40°S) the model simulates a net heating several times greater than that given by the data of Fig. 50b, as is readily seen in the differences between the simulated and observed heat-balance distributions given in Fig. 51. A local error of 300 ly day^{-1} is here not uncommon, and is in many instances comparable to the individual terms of (15). Over the continents both the observed and simulated net surface heating are generally slight. If we recall that the model was designed with a zero surface heat balance over land, the small values (< 10 ly day^{-1}) in Fig. 50b over the continents are thus seen to be due to numerical error.

In the zonal averages shown in Fig. 52, the simulated surface heat balance can be considered a good approximation to observation everywhere north of about 45°S. In diagnosing this balance in terms of (15), the surface longwave radiation, R_4, may be considered to be modeled with good accuracy at all except polar latitudes in view of the generally successful surface temperature simulation (see Figs. 13 to 15). In the tropics the excessive solar radiation absorbed at the surface, S_g, and the positive heating error introduced by the simulated (negative) sensible-heat flux, Γ, are approximately offset by the excessive heat, $L\rho_w E$, lost through too high a simulated surface evaporation (see Fig. 42). In the middle northern latitudes an approximately correct

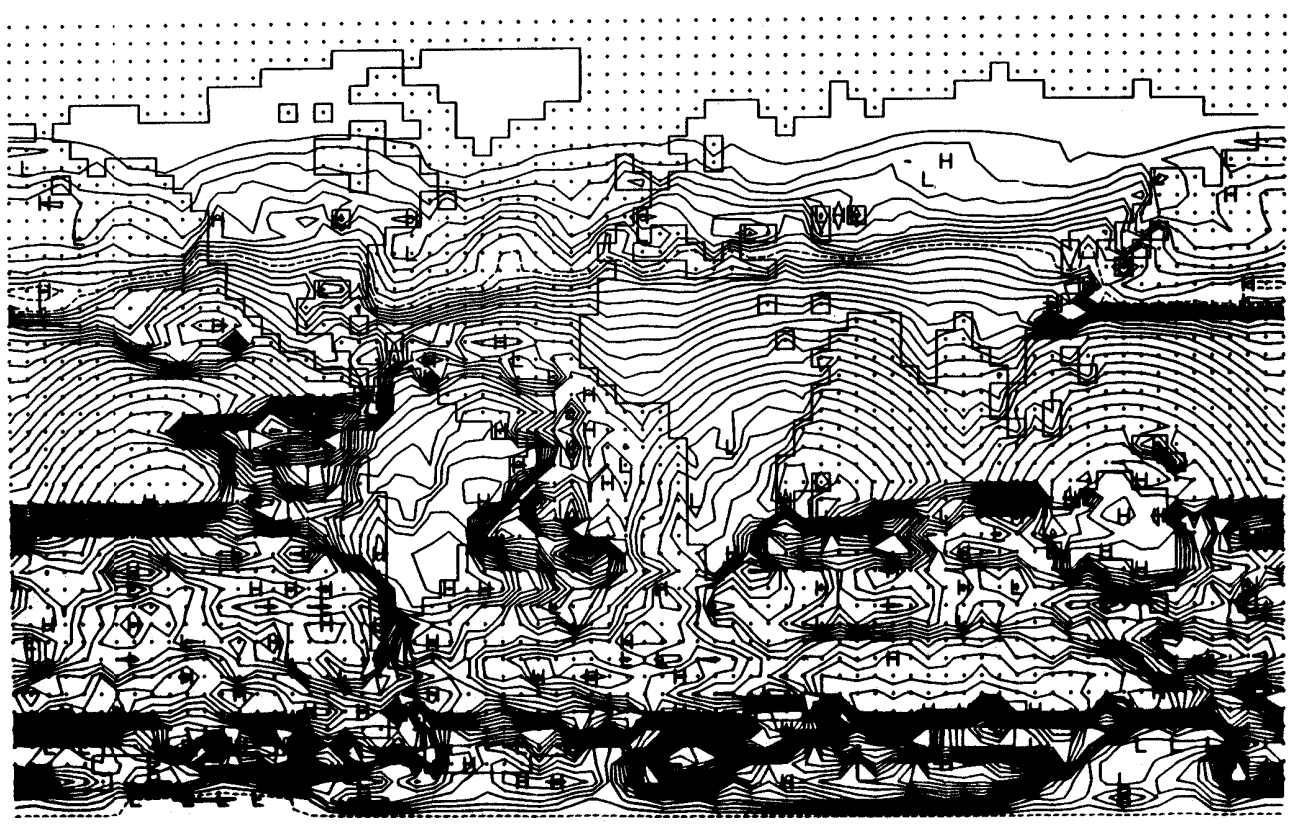

Fig. 47a -- The simulated shortwave (solar) radiation incident at the surface in January, with isolines every 25 ly day^{-1} and the 250 ly day^{-1} isoline dashed.

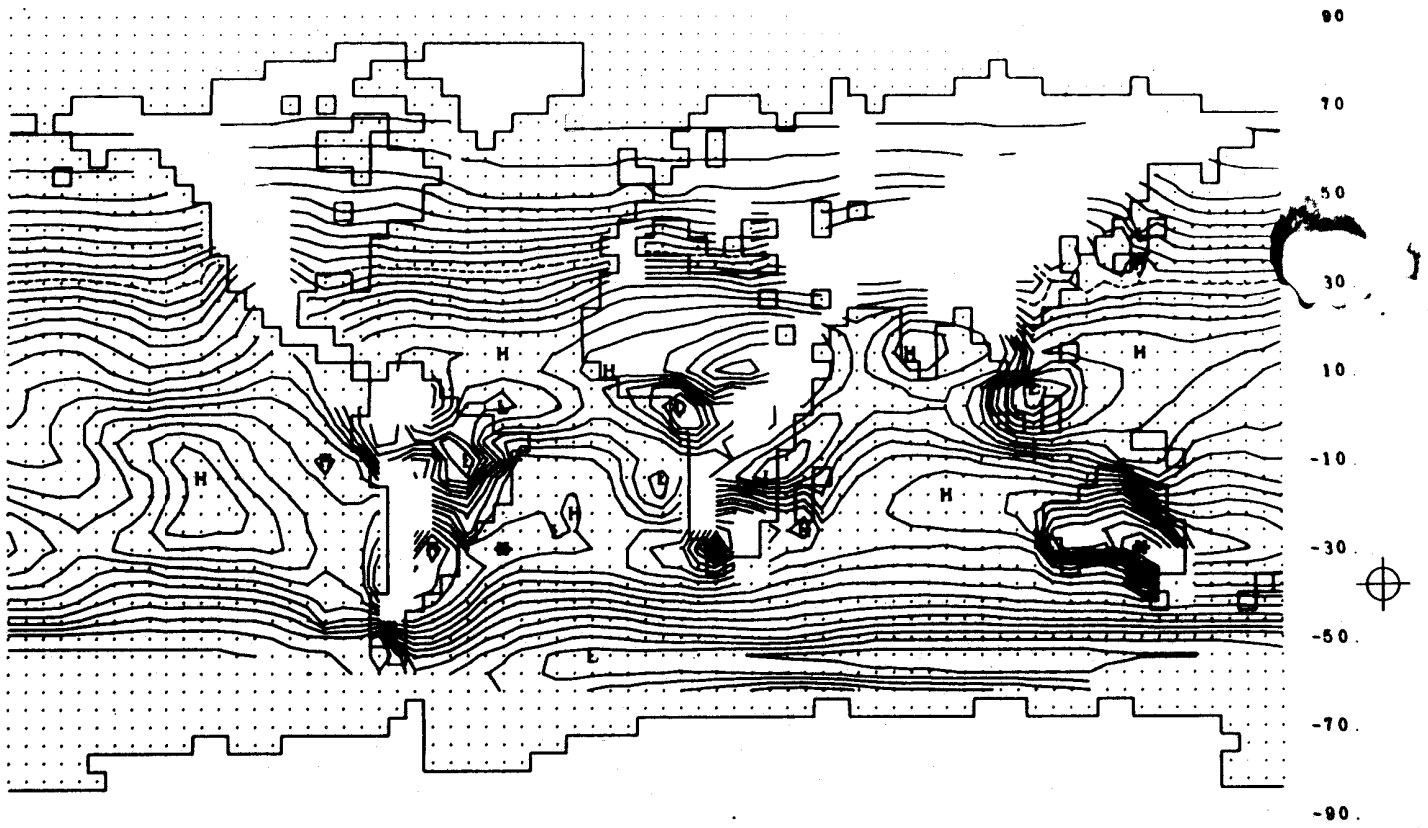

Fig. 47b -- The observed shortwave (solar) radiation incident at the surface in January, with isolines every 25 ly day^{-1} and the 250 ly day^{-1} isoline dashed. From data of Budyko (1963) as summarized by Schutz and Gates (1971).

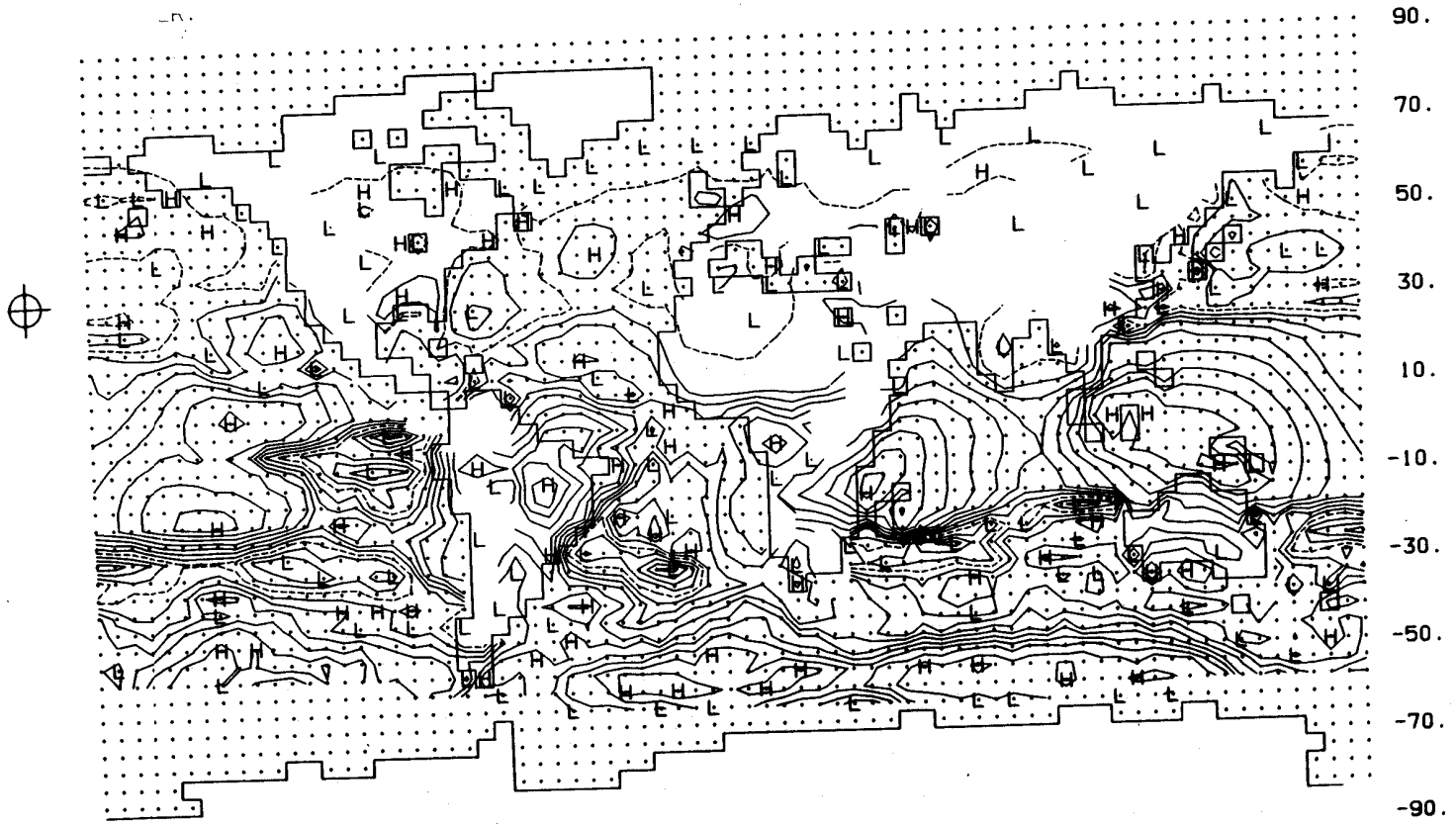

Fig. 48 -- The difference between the simulated and observed shortwave (solar) radiation incident at the surface (Fig. 47a minus Fig. 47b). The isoline interval is 50 ly day^{-1}, with the zero isoline dashed.

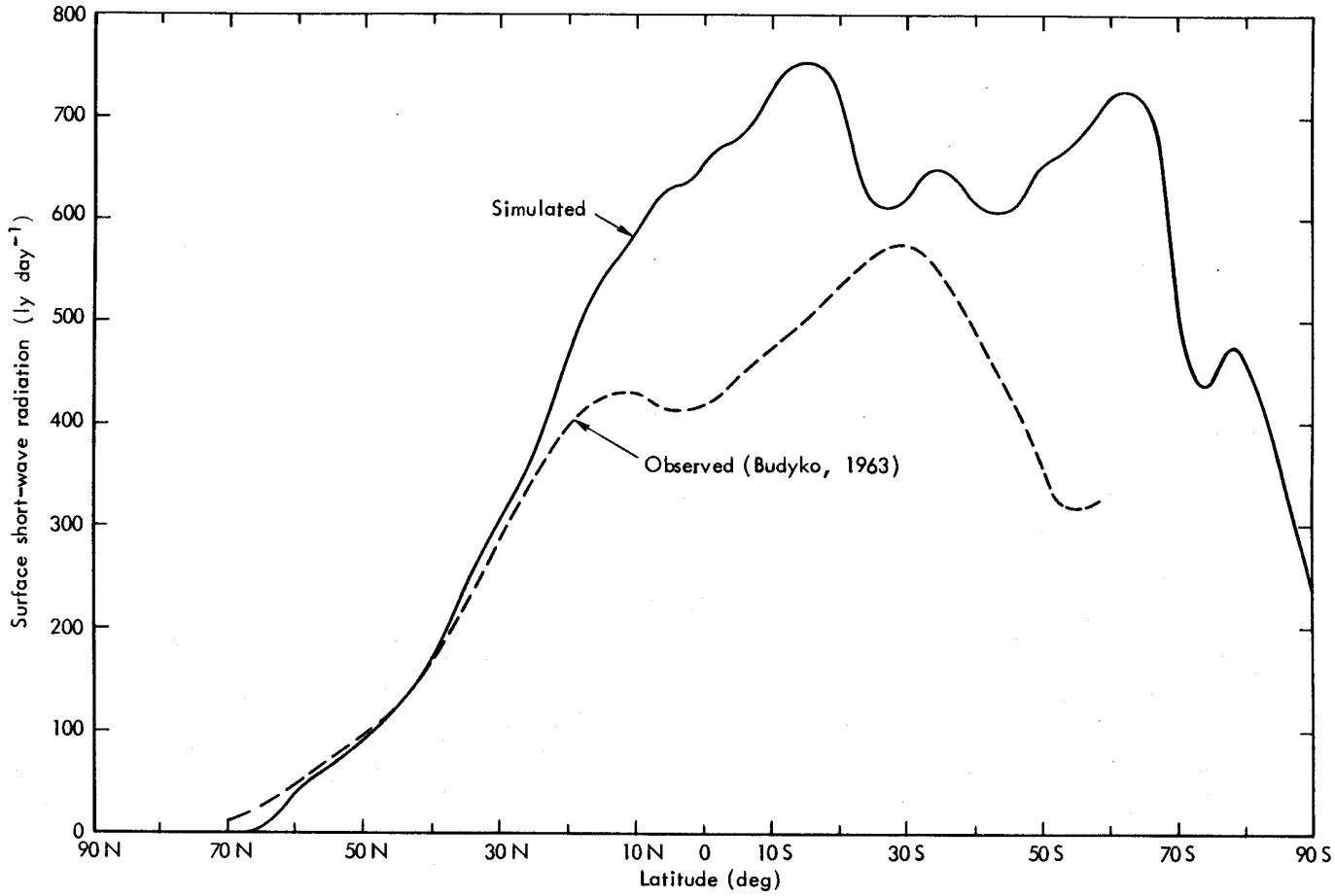

Fig. 49 -- The zonal average of the simulated shortwave radiation incident at the surface (full line) and that observed (dashed line), based on the data of Fig. 47.

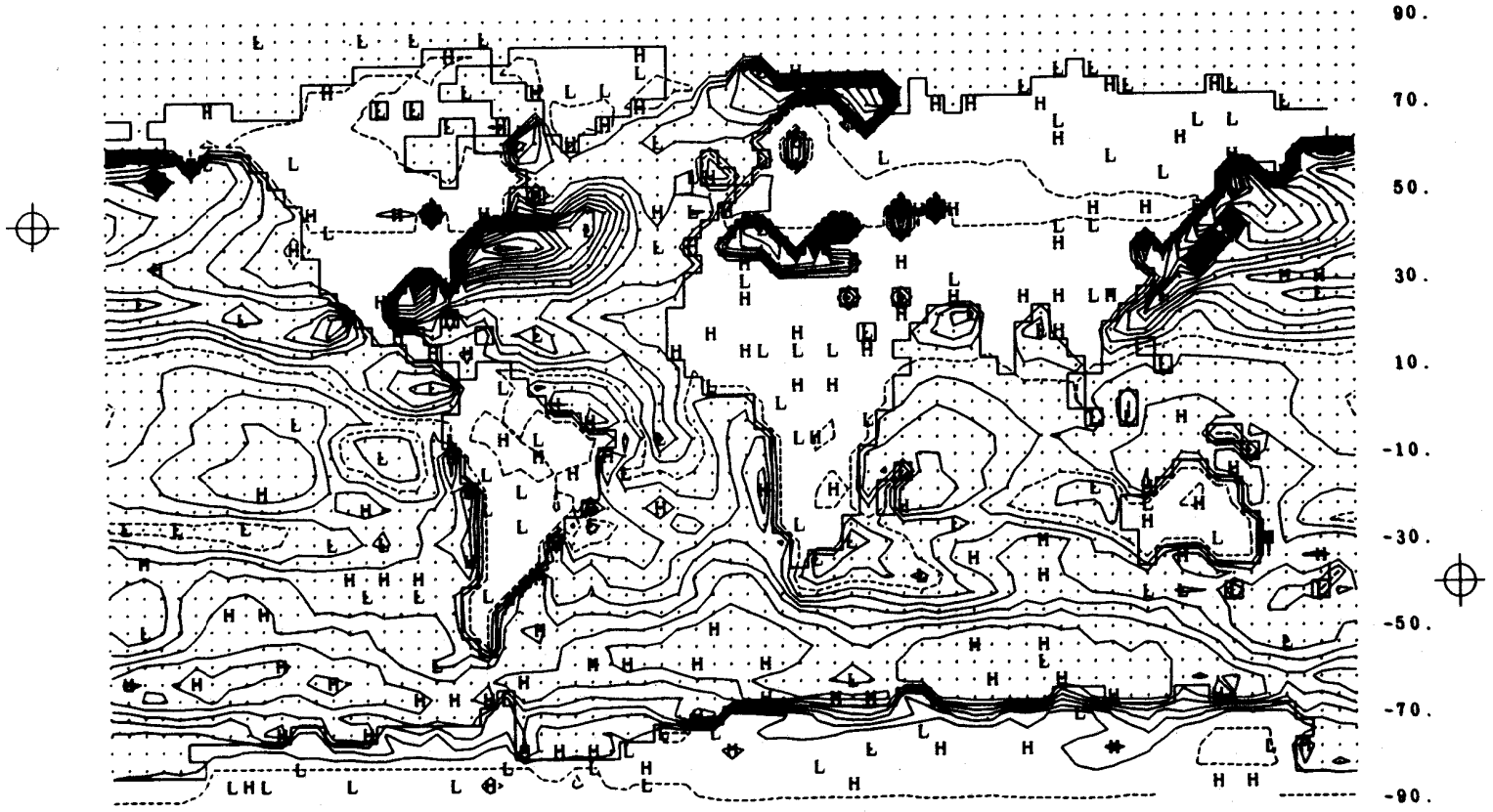

Fig. 50a -- The simulated surface heat balance in January, given by the excess of the solar radiation absorbed over the (usual) losses due to evaporative cooling, long-wave radiation, and upward sensible heat flux. The isoline interval is 100 ly day^{-1}, with the zero isoline dashed. Data from Figs. 40, 44, and 47.

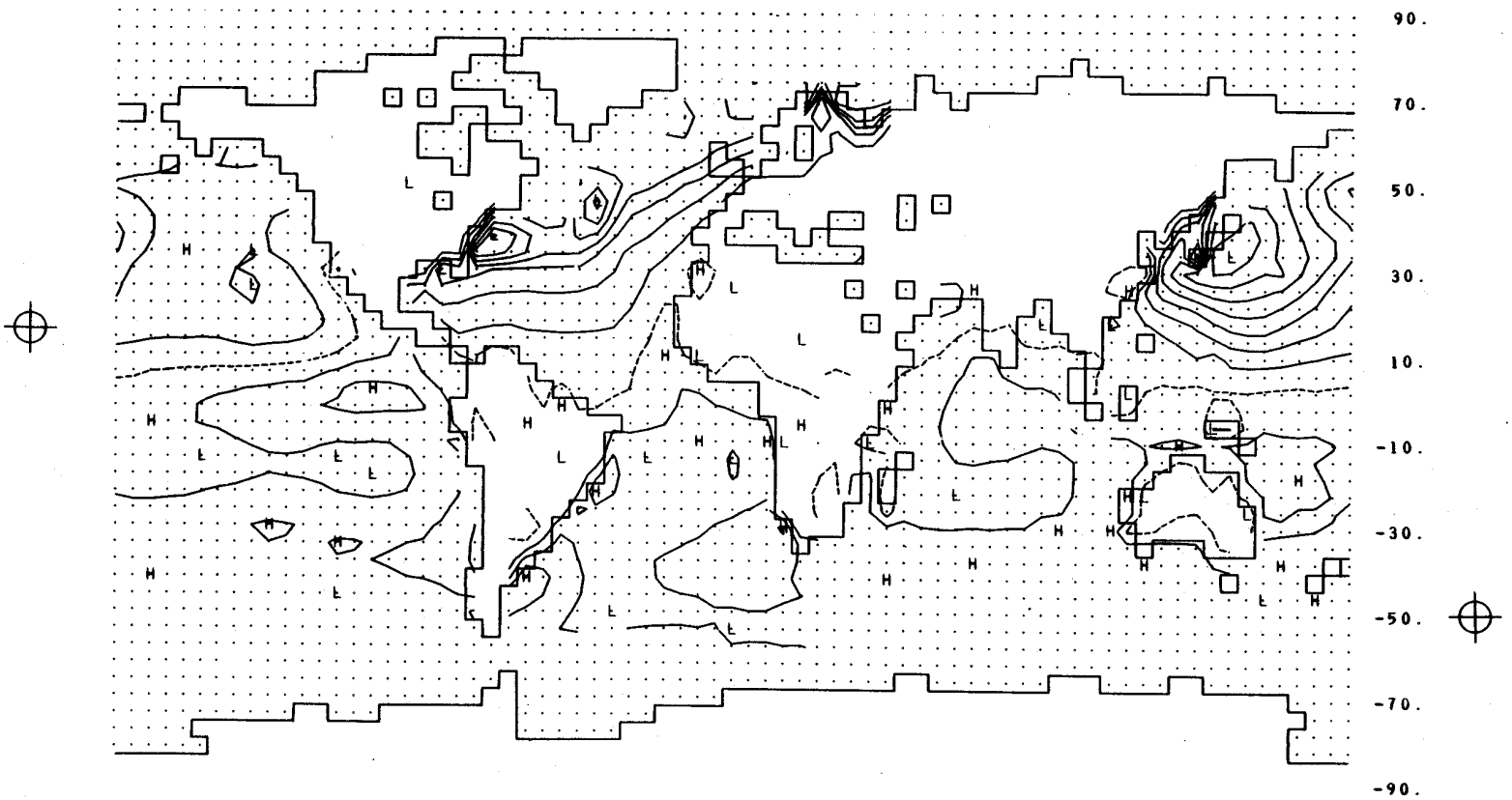

Fig. 50b -- The observed surface heat balance in January, given by the excess of the solar radiation absorbed over the (usual) losses due to evaporative cooling, long-wave radiation, and upward sensible heat flux. The isoline interval is 100 ly day^{-1}, with the zero isoline dashed. Based on data of Budyko (1963) as summarized by Schutz and Gates (1971).

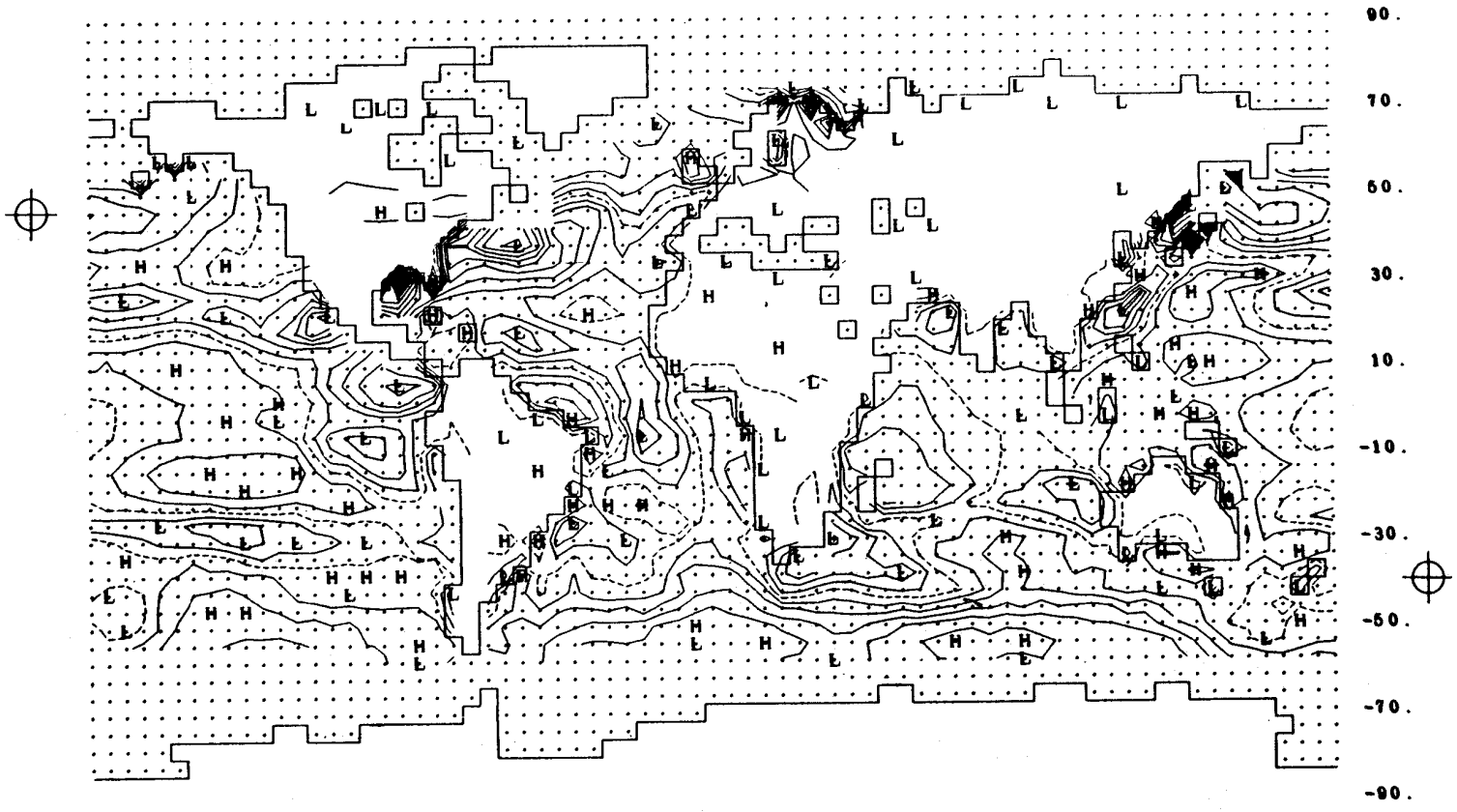

Fig. 51 -- The difference between the simulated and observed surface heat balance (Fig. 50a minus Fig. 50b). The isoline interval is 100 ly day^{-1} with the zero isoline dashed.

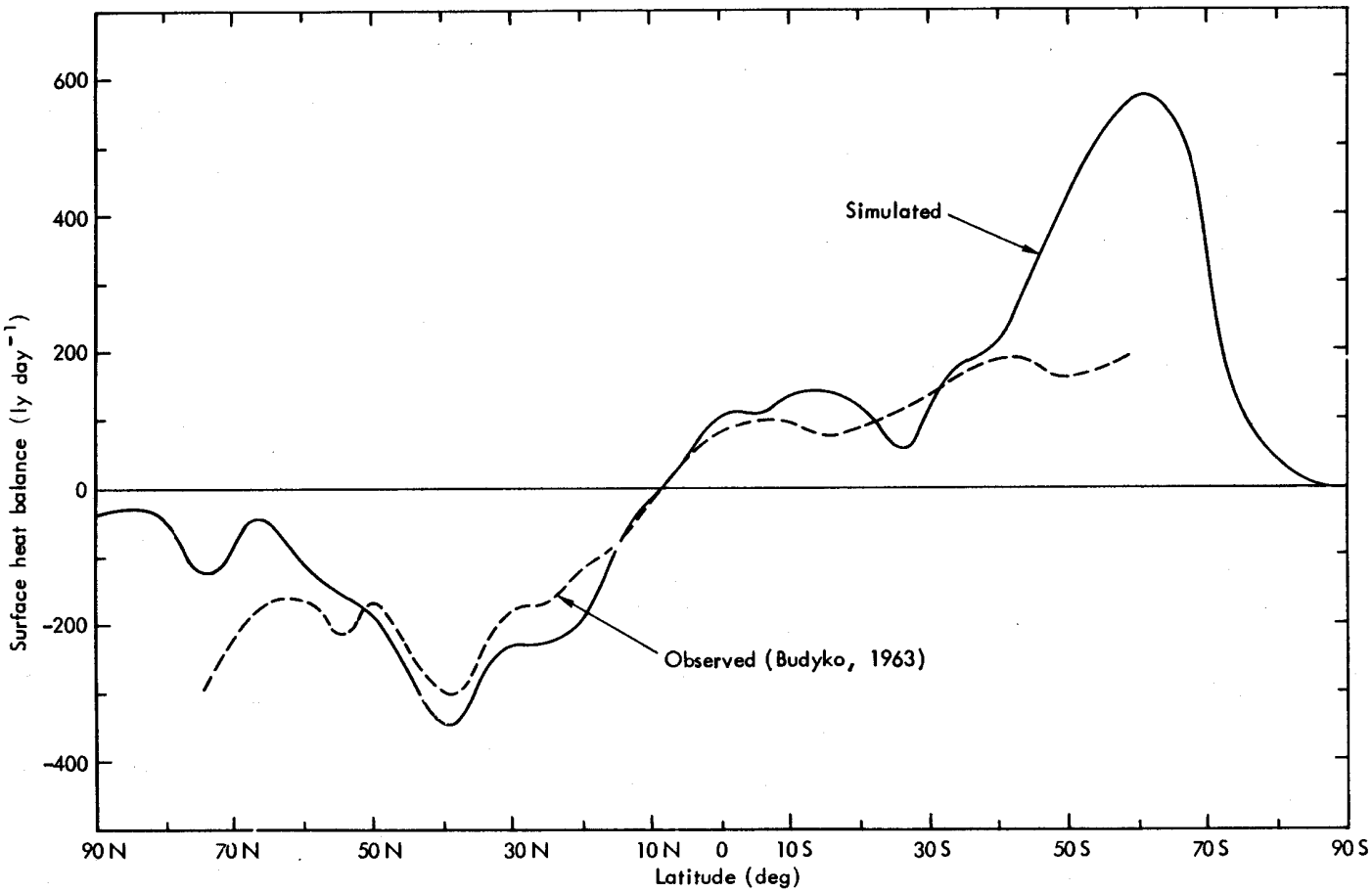

Fig. 52 -- The zonal average of the surface heat balance as simulated for January (full line) and as observed (dashed line), based on the data of Fig. 50.

surface heat balance results from compensation between a simulated Γ which is too small and a simulated evaporation which is too great.

Over the southern hemisphere oceans (say south of 45°S), such error compensation does not occur. The excessive positive net surface heating simulated between about 50°S and 70°S (see Figs. 50a and 52) is a direct result of the simulation of excessively great solar-radiation absorption at the surface, as may be seen in Fig. 49. This error is evidently due to the small amounts of simulated cloudiness, and not to the inadvertent surface-albedo error noted earlier. This excessive solar radiation incident (and absorbed) at the surface is responsible for the high simulated global average surface heating of 35 ly day^{-1}. The corresponding observed value from the (incomplete) global data of Fig. 50b is 7 ly day^{-1}.

VII. SUMMARY AND CONCLUSIONS

In this report, the January global climate simulated by the two-level Mintz-Arakawa model has been presented, both in terms of the mean global patterns and the associated zonal averages. In addition to the familiar meteorological variables of pressure, temperature, wind, humidity, and precipitation, the simulated patterns of certain elements of the moisture and energy balances are also given. In general, those fields selected were ones for which global observations were available. To facilitate comparison, both the model's simulations and the observed data have been presented in a uniform format (Schutz and Gates, 1971); the difference between the two fields (the simulation error) is also given.

Considering the relative simplicity of the model, the simulated climate may, in general, be considered reasonably accurate. A number of characteristics of the errors of the January simulation are summarized in Table 1.* A detailed discussion of each of the simulation errors is given in the text, along with the complete global and zonal average error distributions. The text should also be consulted for a discussion of the simulated mean meridional circulation and the surface absorption of solar radiation.

Each of the simulated fields shows a large-scale pattern of departure from the observed distribution, and in some variables this error represents a substantial fraction of the observed value itself. This is particularly true for zonal wind, relative humidity, precipitation, evaporation, and sensible-heat flux and heat balance at the surface. Most of these errors are systematic with respect to latitude and may be seen in the zonal averages. For example, the simulated temperature at 400 mb is about 6 deg C too high in the tropics (Fig. 21); the maximum zonal winds (jet stream) in the northern hemisphere

*Excluded from this summary are the latitudes south of 70°S, in view of the inadvertent ice-albedo error noted earlier. As is described previously, this error has introduced an anomaly of 10 to 15 deg C in the surface temperatures over Antarctica, and has resulted in the simulation of excessive evaporation and (convective) precipitation between about 70°S and 90°S.

Table 1

SUMMARY OF ERRORS OF JANUARY CLIMATE SIMULATED BY THE TWO-LEVEL MINTZ-ARAKAWA MODEL

Variable	Error Characteristics (Simulation Minus Observation)			Remarks on Simulation
	Typical Local Error Magnitude	Maximum Zonal Average Error[a] (and Simulated Value)	Global Average Error (and Simulated Value)	
Sea-level pressure (mb)	±10	-10.3 (1003.5)	-0.8[b] (1010.3)	midlatitude quasi-stationary systems too intense; transient cyclones too weak.
Geopotential height (m)				
800 mb	+300	+382 (2042)	+300 (2268)	absolute heights everywhere too high[c]; midlatitude gradient too steep.
400 mb	+300	+441 (7795)	+323 (7600)	
Temperature: (deg C)				
surface	±6	+4.0 (-9.5)	+1.2 (13.4)	tropical oceans and continental interiors too warm.
800 mb	±6	-5.3 (2.3)	-0.9 (3.2)	oceanic regions too cold; midlatitude gradient too great.
400 mb	±10	+9.4 (-18.5)	+3.7 (-24.2)	tropics too warm; midlatitude gradient too great.
Zonal wind ($m\ sec^{-1}$)				
800 mb	±10	+6.5 (13.7)	+1.0[d] (3.1)	midlatitude westerlies too strong.
400 mb	±20	+14.9 (35.1)	+3.1[d] (11.8)	
Meridional circulation (10^{12} g sec^{-1})	±40[e]	-99 (-101)	...	southern hemisphere Hadley and Ferrel cells too strong; northern Ferrel cell too weak.
Relative humidity (%)				
800 mb	±30	-27.0 (31.6)	+1.4 (59.2)	tropics too dry, midlatitudes too moist.
Cloudiness	-0.3	-0.37 (0.06)	-0.26[f] (0.26)	total cloudiness everywhere too little.
Precipitation ($mm\ day^{-1}$)	±5	+6.3[g] (7.4)	+1.9[g] (4.1)	tropical rainfall maxima too high and too far poleward.
Evaporation ($mm\ day^{-1}$)	±5	+3.0 (6.8)	+1.6[h] (4.0)	excessive evaporation over tropical oceans.
Surface sensible-heat flux ($ly\ day^{-1}$)	±100	-124 (-89)	-17[h] (15)	negative flux over tropical oceans; upward flux over continents and higher-latitude oceans too great.
Surface shortwave radiation (ly/day^{-1})	±200	+386 (704)	+134[i] (487)	excessive insolation in tropics and over southern oceans.
Surface heat balance ($ly\ day^{-1}$)	±300	+355 (548)	+17[h] (35)	excessive net heating over southern oceans.

[a] Excluding Antarctica.

[b] Due to arbitrary reduction to sea level.

[c] See pp. 18 and 19.

[d] Average between 4°N and 88°N.

[e] Average between 60°S and 60°N.

[f] Average between 18°N and 90°N.

[g] See footnote, p. 67.

[h] Average between 58°S and 78°N.

[i] Average between 62°S and 70°N.

are about 60 percent stronger than the observed winds (with a smaller error in the southern (summer) hemisphere, Figs. 24 and 25); the relative humidity is about half that observed in the tropics and about 50 percent greater than the observed values in middle and high latitudes (Fig. 33); both the precipitation and the evaporation are about twice those observed in the tropics (Figs. 39 and 42); and the simulated surface sensible-heat flux is negative at low and high latitudes, whereas the observed flux is everywhere positive (Fig. 46).

Aside from the systematic bias in the geopotential noted earlier, only the simulated cloudiness shows an error of uniform sign; judged from the best available observations (U.S. Air Force; see Fig. 36), the total cloud cover simulated by the model is only about half that observed, with zonal averages below the observed values everywhere in the northern hemisphere.

From such an overview of the simulation errors, it is tempting to speculate on their causes and possible interrelations. On the basis of the present evidence, there appear to be two major sources of significant error in the model. First are the low values of simulated cloudiness just mentioned. The model's cloudiness is primarily determined by the simulated occurrence of low-level convection, which occurs almost exclusively over the oceans (see Fig. 36). Although no separate low cloudiness observations are available, it is possible that this cloud type is reasonably well accounted for in the model. The substantial amounts of middle- and high-level clouds observed in the atmosphere, however, are represented in the model by relatively small cloud amounts, which, moreover, are simulated only during condensation. The present model makes no attempt to simulate nonprecipitating clouds, and it is the neglect of this cloudiness which is likely responsible for the low total cloud cover simulated. According to London (1957) the energy reflected from clouds is approximately half the shortwave radiation absorbed at the surface. The model's low simulated cloudiness thus reflects too little of the incoming solar radiation and, thereby, permits too much radiation to be absorbed at the surface (Fig. 49). In January this excessive solar radiation absorption is a maximum in the southern hemisphere and is responsibe for the most prominent error of

the simulated surface heat budget (Fig. 52). Most of this energy, however, disappears into the ocean, which is an infinite heat reservoir in the model.

A second significant error in the model is the high values of precipitation simulated in the tropical region between about 25°N and 25°S. As was previously noted, almost all of this precipitation is determined by the simulated occurrence of penetrating convection. This excessive rainfall is accompanied by the release of too much latent heat of condensation, and may therefore be responsible for the excessively warm air simulated at 400 mb (Fig. 21). The midlatitude meridional temperature gradient is thereby increased, which in turn contributes to the simulation of excessively strong westerly winds and too steep a meridional geopotential height gradient. Rather than increasing the instability of the transient baroclinic waves in middle latitudes as might be expected, these errors appear to have intensified the quasi-stationary long waves and resulted in an excessively strong mean meridional circulation (Fig. 30b). Although it is dangerous to speculate in a qualitative manner, it may be that the excessive tropical precipitation removes too much moisture from the atmosphere (modeled only at the lower level) and is thus a cause of the low simulated relative humidity at 800 mb between about 25°N and 25°S (Fig. 33). This in turn would promote the excessive evaporation in the same region (Fig. 42), since the surface moisture is fixed over the oceans where nearly all of the evaporation occurs.

If the major errors of the present control integration are indeed associated with the model's underprediction of the cloudiness and its overprediction of the convection as hypothesized above, then the appropriate revision of these parameterizations could be expected to markedly improve the accuracy of the climatic simulation. Accordingly, research is now under way to increase the amount of cloudiness simulated in the model by suitable revision of the relation (12) and by the introduction of a provision to allow midlevel nonconvective cloudiness even in the absence of precipitation. Other research is in progress whose aim is to reduce the amount of convective precipitation by suitable revision of the convective parameterization. (This parameterization has also

been revised in the design of a new three-level version of this model [Arakawa, 1972].) With these modifications, a new January integration is envisaged, which will also include the appropriate monthly distribution of sea-surface temperature (replacing the annual averages used here), and a more realistic distribution of the seasonal surface albedo (replacing the values 0.14 and 0.07 now assigned to all land and ocean, respectively, and the (erroneous) values used for snow and ice).

In interpreting the results of this or any other general circulation model, it is important to recognize that there may be significant variations in the simulated seasonal averages from one year to the next; most analyses, including the present one, have considered only a single month's simulation. Some information on annual variability of the present model over a three-year period is in preparation by Mintz et al. (1972), and longer runs are envisaged with improved versions of the model as discussed above. Further work of this sort is needed in order to determine more accurately the model's true ability to simulate climate and, thereby, to assess its usefulness as a tool in the study of climatic change.

REFERENCES

Arakawa, A., "Design of the UCLA General Circulation Model," *Numerical Simulation of Weather and Climate*, Tech. Report No. 7, Department of Meteorology, University of California, Los Angeles, 1972.

Arakawa, A., A. Katayama, and Y. Mintz, "Numerical Simulation of the General Circulation of the Atmosphere," *Proc. of the WMO/IUGG Symposium on Numerical Weather Prediction in Tokyo*, Meteorological Society of Japan, Tokyo, 1969, pp. IV.7-IV.8.12.

Berkofsky, L., and E. A. Bertoni, "Mean Topographic Charts for the Entire Earth," *Bulletin of the American Meteorological Society*, Vol. 36, No. 7, September 1955, pp. 350-354.

Budyko, M. I., *Atlas of the Heat Balance of the Earth*, Gidrometeorizdat, Moscow, 1963, 69 pp.

Crutcher, H. L., *Meridional Cross-Sections, Upper Winds over the Northern Hemisphere*, Technical Paper No. 41, National Weather Records Center, U.S. Weather Bureau, Asheville, N.C., 1961.

Crutcher, H. L., and J. M. Meserve, *Selected Level Heights, Temperatures and Dew Points for the Northern Hemisphere*, NAVAIR Publication 50-1C-52, Naval Weather Service, Washington, D.C., 1970.

Dietrich, G., *General Oceanography* (translated by F. Ostapoff), Inter-Science, New York, 1963, 588 pp.

Environmental Technical Applications Center, U.S. Air Force, *Northern Hemisphere Cloud Cover*, Project 6168, Washington, D.C., 1971.

Gates, W. L., *Analysis of the Mean Forcing Fields Simulated by the Two-Level Mintz-Arakawa Atmospheric Model*, The Rand Corporation, R-958-ARPA, May 1972, 43 pp.

Gates, W. L., E. S. Batten, A. B. Kahle, and A. B. Nelson, *A Documentation of the Mintz-Arakawa Two-Level Atmospheric General Circulation Model*, The Rand Corporation, R-877-ARPA, December 1971.

Holloway, H. L., Jr., and S. Manabe, "Simulation of Climate by a Global General Circulation Model: I. Hydrologic Cycle and Heat Balance," *Monthly Weather Review*, Vol. 99, No. 5, May 1971, pp. 335-370.

Kahle, A. B., "The Radiation Budget of the Mintz-Arakawa Model," The Rand Corporation, 1972 (in preparation).

Kasahara, A., and W. M. Washington, "General Circulation Experiments with a Six-Layer NCAR Model, Including Orography, Cloudiness and Surface Temperature Calculations," *Journal of the Atmospheric Sciences*, Vol. 28, No. 5, July 1971, pp. 657-701.

London, J., *A Study of the Atmospheric Heat Balance*, Final Report, Contract AF19(122)-165, Department of Meteorology and Oceanography, New York University, 1957, 99 pp.

Lvovitch, M. I., and S. P. Ovtchinnikov, *Physical-Geographical Atlas of the World*, Academy of Sciences, USSR, and Department of Geodesy and Cartography, State Geodetic Commission, Moscow, 1964, 298 pp.

Miller, D. B., "Automated Production of Global Cloud Climatology Based on Satellite Data," in *Proc. of 3rd Technical Exchange Conference*, Annapolis, Maryland, 1970.

Mintz, Y., "Very Long-Term Global Integration of the Primitive Equations of Atmospheric Motion: An Experiment in Climate Simulation," *W.M.O. Technical Notes*, No. 66, 1965, pp. 141-167 (see also *Meteorological Monographs*, Vol. 8, No. 30, February 1968, pp. 20-36).

Mintz, Y., A. Katayama, and A. Arakawa, *Simulation of the Seasonally and Inter-annually Varying Tropospheric Circulation*, Department of Meteorology, University of California, Los Angeles, 1972 (in press).

Möller, F., "Vierteljahrskarten des Niederschlags für die Ganze Erde," *Petermann's Geographische Mitteilungen*, Vol. 95, No. 1, 1951, pp. 1-7.

Newell, R. E., D. G. Vincent, T. G. Dopplick, D. Ferruzza, and J. W. Kidson, "The Energy Balance of the Global Atmosphere," *The Global Circulation of the Atmosphere*, Royal Meteorological Society, London, 1970, pp. 42-90.

Oort, A. H., and E. M. Rasmusson, "On the Annual Variation of the Monthly Mean Meridional Circulation," *Monthly Weather Review*, Vol. 98, No. 6, June 1970, pp. 423-442.

Palmén, E., and C. W. Newton, *Atmospheric Circulation Systems*, Academic Press, New York, 1969, 603 pp.

Phillips, N. A., "The General Circulation of the Atmosphere: A Numerical Experiment," *Quarterly Journal of the Royal Meteorological Society*, Vol. 82, No. 352, April 1956, pp. 123-164.

Schutz, C., and W. L. Gates, *Global Climatic Data for Surface, 800 mb, 400 mb: January*, The Rand Corporation, R-915-ARPA, November 1971, 173 pp.

Schutz, C., and W. L. Gates, *Supplemental Global Climatic Data: January*, The Rand Corporation, R-915/1-ARPA, May 1972, 41 pp.

Smagorinsky, J., "General Circulation Experiments with the Primitive Equations: I. The Basic Experiment," *Monthly Weather Review*, Vol. 91, No. 3, March 1963, pp. 99-164.

Taljaard, J. J., H. Van Loon, H. L. Crutcher, and R. L. Jenne, *Climate of the Upper Air: Southern Hemisphere, Vol. 1. Temperatures, Dew Points and Heights at Selected Pressure Levels*, NAVAIR Publication 50-1C-55, Naval Weather Service, Washington, D.C., 1969.

Washington, W. M., and L. G. Thiel, *Digitized Global Monthly Mean Ocean Surface Temperatures*, NCAR-TN-54, National Center for Atmospheric Research, Boulder, Colorado, 1970.

Gates

THE JANUARY GLOBAL CLIMATE SIMULATED BY THE TWO-LEVEL MINTZ-ARAKAWA MODEL: A COMPARISON WITH OBSERVATION

R-1005-ARPA